Technische Universität München
Institut für Energietechnik

Lehrstuhl für Thermodynamik

Large Eddy Simulation of Reacting Jets in Hot Crossflow under Atmospheric and Gas Turbine Conditions

Johannes Michael Quirin Weinzierl

Vollständiger Abdruck der von der Fakultät für Maschinenwesen der Technischen Universität München zur Erlangung des akademischen Grades eines

DOKTOR – INGENIEURS

genehmigten Dissertation.

Vorsitzender:
    Prof. Dr.-Ing. Georg Wachtmeister
Prüfer der Dissertation:
    Prof. Dr.-Ing. Thomas Sattelmayer
    Prof. Dr. rer. nat. Michael Pfitzner, Universität der Bundeswehr München

Die Dissertation wurde am 18.12.2015 bei der Technischen Universität München eingereicht und durch die Fakultät für Maschinenwesen am 23.05.2016 angenommen.

Abstract

A numerical tool has been designed to describe an axially staged combustion process of a heavy duty gas turbine with means of LES. Two different combustion models have been coupled with the newly developed NOx model. A validation with experimental results from an atmospheric test rig reveals an excellent performance of the tool.

A reduction of NOx due to mixing effects has been identified when simulating engine conditions of technical interest. Conducted investigations figured out that different jet geometries of the second stage and an elevation of the velocity magnitude can improve the mixing process.

Zusammenfassung

Um die Vorgänge in einer gestuften Verbrennung einer industriellen Gasturbine berechnen zu können, wurde ein neues NOx Modell entwickelt. Dieses wurde mit zwei unterschiedlichen Verbrennungsmodellen kombiniert. Ergebnisse auf dieser Basis zeigen eine sehr gute Übereinstimmung mit den Messwerten.

Die Berechnungen zeigen, dass die NOx Emissionen unter Maschinenbedingungen durch Mischungsprozesse reduziert werden können. Diese Mischungsprozesse werden dabei positiv durch die absolute Geschwindigkeit und die Jet-Geometrie beeinflusst.

Contents

List of Tables

List of Figures

Nomenclature

Latin letters

A	Proportional factor	[-]
C	Progress variable	[-]
C	Constant	
D	Jet diameter	[m]
D	Diffusion coefficient	[$\mathrm{m^2\ s^{-1}}$]
E_A	Activation energy	[$\mathrm{J\ mole^{-1}}$]
E	Efficiency factor	[-]
F	Thickening factor	[-]
G	Filter kernel	
G	Flame surface tracking variable	[-]
ΔH_R^0	Standard enthalpy of reaction	[$\mathrm{J\ kg^{-1}}$]
I	Turbulence Intensity	[-]
J	Momentum ratio	[-]
M	Molar mass	[$\mathrm{kg\ kmol^{-1}}$]
P	Probability function	[-]
$\dot{Q}$	Heat flux	[$\mathrm{J\ s^{-1}}$]
R	Specific gas constant	[$\mathrm{J\ kg^{-1}\ K^{-1}}$]
R_u	Universal gas constant	[$\mathrm{J\ mol^{-1}\ K^{-1}}$]
RR_i	Rate of formation	[$\mathrm{mol\ s^{-1}}$]
S	Species	[-]
T	Temperature	[K]
V	Diffusion velocity	[$\mathrm{m\ s^{-1}}$]
V	Volume	[$\mathrm{m^3}$]
X	Mole fraction	[-]
Y	Mass fraction	[-]

Z	Mixture fraction	[-]
a	Thermal conductivity	[J s^{-1} m^{-1} K^{-1}]
c_p	Specific heat capacity	[J kg^{-1} K^{-1}]
f	Jet mixture fraction	[-]
Δh_f^0	Specific standard enthalpy of formation	[J kg^{-1}]
h_s	Sensible enthalpy	[J kg^{-1}]
k	Turbulent kinetic energy	[m^2 s^{-2}]
k	Proportional constant	[-]
l	Characteristic length	[m]
l_t	Integral length scale	[m]
l_η	Kolmogorov length scale	[m]
l_Δ	SGS velocity fluctuation lenght scale	[-]
m	Mass	[kg]
n	Number of atoms	[-]
p	Pressure	[Pa]
s_l	Laminar flame speed	[m/s]
t	Time	[s]
t_c	Chemical time scale	[s]
t_t	Integral time scale	[s]
t_η	Kolmogorov time scale	[s]
u	Velocity	[m/s]
x	Direction vector	[-]

Greek letters

Γ	Model constant	[-]
Δ	Filter width	
Δ_e	Test filter width	
Φ	Equivalence ratio	[-]
Φ	Normalized temperature	[-]
Ξ	Wrinkling factor	[-]
Θ	Normalized temperature	[-]
Ω	Flame sensor	[-]
β	Model constant	[-]

δ_{ij}	Kronecker delta	[-]
δ_l	Laminar flame thickness	[m]
λ	Thermal conductivity	[J s^{-1} m^{-1} K^{-1}]
ϵ	Dissipation rate	[m^2 s^{-3}]
κ	Wave number	[m^{-1}]
κ	Reacting volume fraction	[-]
σ	Variance	[-]
τ	Time scale	[s]
τ	Shear stress tensor	[kg $\mathrm{m}^{-1}\mathrm{s}^{-2}$]
$\tau*$	Subgrid mixing time	[s]
ρ	Density	[kg m^{-3}]
μ	Dynamic viscosity	[Pa s]
ν	Kinematic viscosity	[m^2 s^{-1}]
ν'	Stoichiometric coefficient of reactants	[-]
ν''	Stoichiometric coefficient of products	[-]
$\dot{\omega}$	Source term	[s^{-1}]

Indices and superscripts

ad	Adiabatic
cf	Cross flow
EBU	Eddy break up
$fuel$	Fuel
i	Direction component
ign	Ignition delay
j	Direction component
k	Species placeholder
n	Temperature exponent
ox	Oxidizer
s	Sub grid model
tot	total
$Prod$	Products
$Reac$	Reactants
RMS	Root mean square

Δ_e	Test filter width

Dimensionless numbers

CFL	Courant-Friedrichs-Lewy number
Da	Damköhler number
Da_t	Ignition delay Damköhler number
Ka	Karlovitz number
Ka_τ	Karlovitz number based on ignition delay
Ka_{mix}	Karlovitz number of the mixture
Pr	Prandtl number
Re	Reynolds number
Re_t	Turbulent Reynolds number
Sc	Schmid number
Sc_t	Turbulent Schmid number

Symbols and operators

$\bar{(\ )}$	Mean value
$(\ )'$	Fluctuating value
$\tilde{(\ )}$	Favre average
$\hat{(\ )}$	Spacial filter
$\vert(\ )\vert$	Absolute value

Acronyms and abbreviations

SMD	Spacial mixing deficiency
CFD	Computer fluid dynamics
CM	Combustion model
DES	Detached eddy simulation
LDA	Laser Doppler anemometry
LES	Large eddy simulation
LO	Lift-off height

NO_x	Nitrogen oxide + nitrogen dioxide
NO	Nitrogen oxide
NO_2	Nitrogen dioxide
$PaSR$	Partially stirred reactor
PDF	Probability density function
TFM	Thickened flame model
SAS	Scale adaptive simulation
SGS	Sub grid scale
$URANS$	Unsteady Reynolds Averaged Navier Stokes

1 Introduction

The electricity generation in Germany has been changing for the last 20 years. An increasing amount of electricity is produced from renewable resources instead of fossil fuels and nuclear power. Responsible for this change are mainly two reasons: First, the prices for fuel and fees on emissions are steadily rising. Second, the electricity generation from fossil fuels contribute negatively to the global climate change.

The drawback of naturally available energy is the varying uptime which can not be predicted exactly yet. To compensate the lack of power from wind and solar, additional capacities of variable power generation need to be provided by gas turbine power stations. Therefore and for the replacement of nuclear and coal power plants the International Energy Agency predicts an increasing market share for electricity form natural gas in Germany [36]. Similar scenarios are valid for many countries in Western Europe and everywhere in the world, where electricity base load is generated by fluctuating renewable resources.

One of the core processes in gas turbines is the combustion process. An innovative combustion concept will be studied within this work. By that the grid operators are offered a higher flexibility and faster responses on frequency fluctuations within the grid. Furthermore, the investigated combustion concept assures a clean electricity generation by meeting the constantly increasing constraints of pollutants emissions like nitrogen oxide and carbon oxide while at the same time the total efficiency is maximized.

1.1 Technical Background

In the past and today, companies, scientists and government put huge effort in fulfilling the emission requirements of gas turbines [45], as the limits are continuously reduced [7]. In parallel, the efficiency of gas turbines should be increased, which is closely coupled to a higher turbine inlet temperature.

Nitrogen oxides (NO_x) production is strongly coupled to high combustion temperatures. Obviously, reducing NO_x emissions and increasing efficiency are contradicting goals.

Basically, two different combustion regimes are found in gas turbines: diffusion flames, where fuel and air enter the combustion chamber separately and mix within the combustion chamber; and premixed combustion, where the fuel and air enter the combustion chamber already mixed with each other. In order to reduce NO_x in a diffusion flame, the thermal load through recirculation of vitiated air or injection of water is increased, causing a reduction of the peak temperatures. In premixed systems, combustion is close to the extinction limits, leading to a very lean premixed flame and to lower NO_x rates.

Both concepts are designed for full load operation. To be able to operate at different loads and still remain within emission limits, special precautions are necessary. Given that the air flow rate is almost fixed and can not be altered without variable compressor stages or complex bypass systems, generally the fuel mass flow rate is used to vary power output. While diffusion flames can be operated at different loads by changing the fuel mass flow rate. In lean premixed systems, the ratio of air and fuel supply must be kept within narrow limits. As the lean premixed systems generate the low NO_x emissions only within a narrow range, special technical solutions were developed for staging. These can be classified into three categories: the first approach is to switch to non premixed combustion within the burner. Therein, a certain amount of fuel is injected directly to the burner exit to sustain premixed combustion. But, this causes high NO_x mainly formed by the pilot flame.

A second approach is to operate only a certain number of burners. The burners are arranged in different groups, in order to supply fuel to each burner group individually. Thus, within part load, not all burners are in operation. Since the fuel is distributed equally on the operating burners, the equivalence ratio of the burners varies over the load. Switching on the subsequent group, the equivalence ratio must be increased in advance to avoid lean blow off. Equivalence ratio variations over the load causes high fluctuations of emissions because the combustion temperature and therefore the NO_x emission follows the equivalence ratio.

These fluctuations are compensated by unevenly distributing the fuel over all burners in operation. This is the third category of staging of gas turbine combustion systems. The first burner group is supplied with a equivalence ratio suitable for stable lean premixed operation. Afterwards fuel is supplied to the second group of burners. The fuel is burned while the first burner group acts as a pilot flame, although the equivalence ratio is too lean to form stable flames. Fuel is added to the second group until they reach the desired operation point and generate pilot flames for the subsequent group. This way, the load can be increased or decreased without oscillations in the NO_x emission. The challenge in this concept occurs at low load. It is favorable to mix pilot flame and piloted mixture very well, in order to achieve complete combustion. However, good mixing results in cooler flames when the neighbor burner groups do not operate. The temperature may no longer be sufficient to guarantee total oxidation of the fuel and thus, the performance decreases while unburned fuel is emitted.

The combustion process considered in detail in this thesis is characterized as a 'Late Lean Injection'. After a first combustion stage, where conditions are fixed to lean equivalence ratio of e.g. $\Phi = 0.5$, premixed jets are injected in a second stage at a higher equivalence ratio. The perpendicular injection at the second stage results in a jet in crossflow, formed by the vitiated gas of the first stage and the jet. Most importantly, both stages are fully premixed. This leads to a sequential combustion process because the premixed jet is injected downstream of the first stage. Such axially staged processes exhibit improvement potential for full load NO_x and part load burnout as well.

Although the 'Late Lean Injection' is innovative in its application, the basics, i.e. a perpendicular injection of a jet into a crossflow, has been widely investigated at least for mixing purposes. In the following, a brief review on publications concerning the simulation of a jet in crossflow configuration is given. First, papers focusing on mixing are discussed followed by studies on reacting jet in crossflow and its application. The literature review is ordered from simplest and fastest Reynolds averaged Navier Stokes (RANS) simulations to the time consuming and challenging Direct Numerical Simulations (DNS).

A general comparison of the performance of a variety of turbulence models is given by Karvinen and Ahlstedt [38]. They conclude that velocity computed by a k-ϵ turbulence model best fits the experimental velocities, whereas turbulence itself is underestimated all the time. A combination of RANS and Large Eddy Simulation (LES), Detached Eddy Simulation (DES) and Scale Adaptive Simulation (SAS), is used by Rusch et al. [61] to simulate a jet in crossflow at momentum ratio $J = 5.4$. The authors compare the results with LDA, thermocouple measurements and values from RANS and conclude that the far field can be predicted best with the SAS model. However, the simulation fails when predicting the near field measurements. Clayton and Jones [11] directly compare RANS and LES to experimental velocity data. The authors state that both approaches fit the experimental data quite well whereas the LES provides a better resolution of the recirculation regions than the RANS. The same results are found by Galeazzo et al. [21] and [22], who compare URANS, RANS and LES. The closest agreement between simulated and measured velocity is achieved using LES. The authors further compare simulations and experiments concerning passive scalar concentrations. Only the LES predicts the scalar fields sufficiently well, while URANS and RANS fail. Yuan and Street [71] perform a set of simulation using LES in combination with a dynamic sub grid scale eddy viscosity model to identify the jet bending mechanisms. The authors investigated velocity ratios of 2.0 and 3.3 in combination with a Reynolds Number of $Re = 1050$ and $Re = 2100$ and compare them to measurements. The simulation shows close agreement to the measured temperature. The error is smaller than 10 % although the simulation Re is smaller than the experimental once. The authors conclude that at the exit complex interactions between Reynolds number effects and pressure drag are present, whereas downstream crossflow entrainment controls the jet. It is also stated that at least for one jet diameter the jet pipe should be simulated, because the crossflow influences the jet upstream of the jet exit. Schlüter and Schönfeld [62] simulate a jet in crossflow with LES using a standard and a filtered Smagorinsky SGS model. The simulation results are validated by comparison against experimental measurements from different researchers. The authors reproduce the velocity distribution quite well, but with an error of 50 % in the near field $x/D < 4$. The computed turbulent kinetic energy distribution reproduces the trend correctly, but differs locally more than 100 %. Similarly, the temperature distribution from the simulation hardly predicts the experiment, whereas the trends were captured correctly. But from a different experiment, the mixture fraction of acetone was computed within an excellent agreement of ±5 %. Finally, the authors concluded that the filtered Smagorinsky preforms best among all comparisons. In order to improve the mixing of jet and crossflow, the influence of additional vortical motion through a swirling jet is considered by Denev et al. [18]. By means of LES the authors detect that an increasing swirl of the jet increases the turbulence level and the asymmetry of the flow field. But the higher turbulence level does not significantly improve the spatial mixing. In contrast to Denev et al., Prière et al. [59] achieved an improvement of mixing process by an additional vortex generator in the crossflow upstream of the jet. The authors consider a jet in crossflow with a momentum ratio of $J = 10.4$ at $Re = 150000$ with LES using the WALE SGS model, but did not include a comparison to experimental data for validation. Finally DNS data for a jet in crossflow were published [53], [19]. The considered configurations within these papers suffer from low Reynolds numbers and can not be applied to technical problems where turbulent flows dominate. Nevertheless, for fundamental investigations, DNS can deliver helpful insights into the processes occurring in the jet in crossflow configuration. Further, DNS data can be used in addition to measurements for validation of simplified simulation approaches. For example, Denev et al. [19] suggests to use the WALE SGS model instead of the standard Smagorinsky model, because of its better physical behavior regarding jet in crossflow configurations.

In summary, a transient LES is suitable for jet in crossflow simulations when both velocity and mixture must be predicted. DNS is too expensive in computational time and limited to laminar flows. URANS predicts velocities within a acceptable range but fails in predicting the mixture fraction. A more comprehensive review, including also experiments done so far, is available from Mahesh [49]. All mentioned scientists used round jet geometries for their research.

Less literature is available for chemical reaction in jet in crossflows. A simplified approach is presented by Denev et al. [15] introducing two artificial reacting scalars in addition to a passive scalar for mixing investigations. A higher reaction rate was found in region of higher turbulence, influenced by the coherent structures. A DNS with two artificial reacting scalars is performed by Denev et al. [17], [16] to asses the influence of the Schmidt number and the Damköhler number on combustion. Although due to the intermittency of the flow steady RANS has difficulties to predict the mixture correctly, a comparison of RANS and SAS predicting the auto ignition of hydrogen/nitrogen blends is presented by Invanova et al. [37]. Under reheat combustor conditions, the SAS model is able to predict the auto ignition process, whereas RANS is only able to calculate the flame surface after auto ignition with some limits. The auto ignition process itself is missed. Recently a turbulent DNS of a reacting hydrogen jet into a heated crossflow was published [27]. The aim was to figure out the stabilization method of the hydrogen diffusion flame, which is found to be located in a low velocity region between the counter rotating vortex pair. The authors use a joint PDF approach to model the combustion process and claim a correctly simulated flame position for the jet equivalence ratio of Φ=0.55 and Φ=1.02. However NO_x emissions are not taken into account.

A publication on NO_x modeling for reacting jets in crossflow is not known so far. Simulating NO_x emissions of a different configurations Hirano et al. [31] use LES and introduce a transport equation for NO. The source term for NO is made up of two mechanisms, the thermal and the prompt pathway. Each provides a source term, which is calculated using equilibrium assumptions. The reported results are in agreement with experimental values, but suffer from an incorrect temperature prediction of the combustion model. A similar approach is performed by Cannon et al, [8] using RANS and LES with a separate transport equation for NO. The NO source term is computed using the prompt pathway. The authors conclude that LES predicts results better compared to experimental results than the RANS. A different approach based on the flamelet assumption is developed by Ihme and Pitsch [35]. Again, a transport equation for NO is introduced, but the source term for NO is computed based on the flamelet progress variable from the flamelet library. The occurring closure problem in the NO transport equation was solved by scale similarity assumptions. Two cases were investigated: the Sandia D-flame and an air craft engine. It was found that the correct temperature profile is of utmost importance. Given that the flamelet model takes heat losses due to radiation into account, the NO model is able to predict the experimental values within a certain accuracy. Collonval and Polifke [13] extend the approach of tabulated chemistry. In the preheat- and fuel-consumption- zone the source term is tabulated based on mixture fraction and progress variable. In the post flame zone, the nitrogen oxide source term no longer depends on the flame progress variable. Therefore an algebraic approach, fitted to reactor simulation, is used as source term. But to compute the NO concentration from the algebraic expression, the residence time must be known. To calculate the residence time, an additional integration step is necessary. This is especially difficult when the products are diluted. However, the authors demonstrate an excellent agreement within a laminar diffusion flame.

Additional literature exists for jets in crossflow with reaction under pressure, but only from an experimental point of view. Since a design tool should be developed in this thesis, the focus is on numerical approaches. Therefore, references focusing on experiments are not further discussed.

1.2 Motivation and Outline

To achieve the goal of a higher load flexibility at constant or even improved pollutants concentrations, in particular for nitrogen oxides, axially staged combustion systems are under development. Unlike the widely used approach of fuel staging, where a separate fuel stream is injected into vitiated gas of an upstream combustion stage, a premixed air-fuel jet is perpendicularly injected into the vitiated gas flow. The equivalence ratios are adjusted such that the adiabatic flame temperature of the first stage is fixed while the jet equivalence ratio is varied. At full load, the design assumes a higher equivalence ratio of the jet than of the vitiated crossflow. Varying the jet equivalence ratio while keeping the first stage unchanged allows changing of the thermal power. In optimum cases, the NO_x emissions do not exceed the values obtained in unstaged operation, although the jet operates at higher equivalence ratio than the crossflow.

To investigate this combustion concept, a numerical tool is developed, which allows to predict the combustion process as well as the formation of the NO_x pollutants. This tool aims at atmospheric conditions as well as at engine conditions up to 20 bar. The atmospheric case is used to validate the model using measurements from an atmospheric test rig and to give further insights in the pollutant formation. Furthermore, the tool should close the gap between the atmospheric test rig and the engine in order to predict and investigate the performance of axial staging at pressurized conditions.

In chapter 2 the basic theory needed to understand the processes present in staged combustion is described. The subsequent chapter gives a summary on concepts for the numerical description of reacting flows. A short overview of common combustion models including the two used in the this study is enclosed in section 3.4. The theory part of this thesis closes with the development of a new NO_x model. In chapter 5 non-reacting jet in crossflow large eddy simulations are validated by comparison with velocity and temperature fields from experiments at atmospheric conditions. Afterwards, the results from two different combustion models including the new NO_x model are compared with measurement data for velocity, temperature, flame shape and emissions. Finally, simulations at engine condition at 20 bar including the new NO_x model are presented. Two cases with an attached and a lifted flame are studied. A summary of the results is given in chapter 6.

2 Turbulence and Combustion Theory

In technical applications like gas turbines, it is challenging to obtain information on the fluid flow and the combustion process at each operation condition correctly. Therefore a theoretical description is useful. The combustion process is massively influenced by the flow. Especially the interaction of turbulence and combustion is important and complex at the same time. Therefore at first a generalized description of the fluid flow is given, followed by a chapter on turbulence. The last section introduces to combustion theory and reaction chemistry.

2.1 General Description of Flows

A fluid dynamic problem can be described by the Navier-Stokes equations. Neglecting gravity and using the Einstein notation the equations can be written as [58]:

Continuity

$$\frac{\partial \rho}{\partial t} + \frac{\partial \rho u_i}{\partial x_i} = 0, \tag{2.1}$$

Momentum

$$\frac{\partial \rho u_j}{\partial t} + \frac{\partial \rho u_i u_j}{\partial x_i} = -\frac{\partial p}{\partial x_j} + \frac{\partial \tau_{ij}}{\partial x_i}. \tag{2.2}$$

The density is symbolized by ρ and u_i represents the i-th component of the velocity. The term τ_{ij} describes the elements of the shear stress tensor and is defined as

$$\tau_{ij} = 2\mu(\frac{\partial u_i}{\partial x_j} + \frac{\partial u_j}{\partial x_i}) - \frac{2}{3}\mu\delta_{ij}\frac{\partial u_k}{\partial x_k}. \tag{2.3}$$

In reacting flows the fluid consists of k different species. Therefore, in addition to the continuity equation an equation for each species mass fraction Y_k must be considered.

Species

$$\frac{\partial \rho Y_k}{\partial t} + \frac{\partial}{\partial x_i}(\rho(u_i + V_{k,i})Y_k) = \rho \dot{\omega}_k \tag{2.4}$$

The source term for species k is described by $\dot{\omega}_k$ where $V_{k,i}$ is the diffusion velocity of the species k in the i-th direction. $V_{k,i}$ is usually approximated by Fick's law,

$$\rho V_{k,i} Y_k \approx -D_k \frac{\partial Y_k}{\partial x_i}, \tag{2.5}$$

with D_k representing the diffusion coefficient.

Energy

And, of course, an equation must be considered for the energy release by the chemical process. In that, the energy equation is expressed in terms of the sensible enthalpy h_s.

$$\frac{\partial \rho h_s}{\partial t} + \frac{\partial \rho u_i h_s}{\partial x_i} = \frac{\partial p}{\partial t} + \frac{\partial \rho u_i p}{\partial x_i} + \frac{\partial \tau_{ij} u_i}{\partial x_j} - \frac{\partial q_i}{\partial x_i} + \rho \dot{\omega}_{h_s} \tag{2.6}$$

The heat release rate ω_{h_s} is computed by

$$\dot{\omega}_{h_s} = -\sum_{k=1}^{N} \Delta h^0_{f,k} \dot{\omega}_k \tag{2.7}$$

where $h^0_{f,k}$ represents the standard enthalpy change of formation. The term q_i in equation 2.6 is defined as

$$q_i = -\lambda \frac{\partial T}{\partial x_i} + \rho \sum_{k=1}^{N} h_k Y_k V_{k,i} \tag{2.8}$$

where the thermal conductivity is represented by λ and temperature by T. Again, the diffusion velocity is approximated by Fick's law (equation 2.5).

To close the equation system, the ideal gas law is applied,

$$p = \rho R T \tag{2.9}$$

using the specific gas constant R.

Equations 2.1 - 2.6 show the general form upon which further simplifications are made. The viscous heat source term $\frac{\partial \tau_{ij} u_i}{\partial x_j}$ in equation 2.6 is neglected as its influence is several orders smaller compared to the other terms. Because of the same reason, the enthalpy transport by species diffusion $\rho \sum_{k=1}^{N} h_k Y_k V_{k,i}$ is neglected. Finally, the heat flux term in equation 2.8 is simplified to $-\frac{\lambda}{C_p}\frac{\partial h_s}{\partial x_i}$.

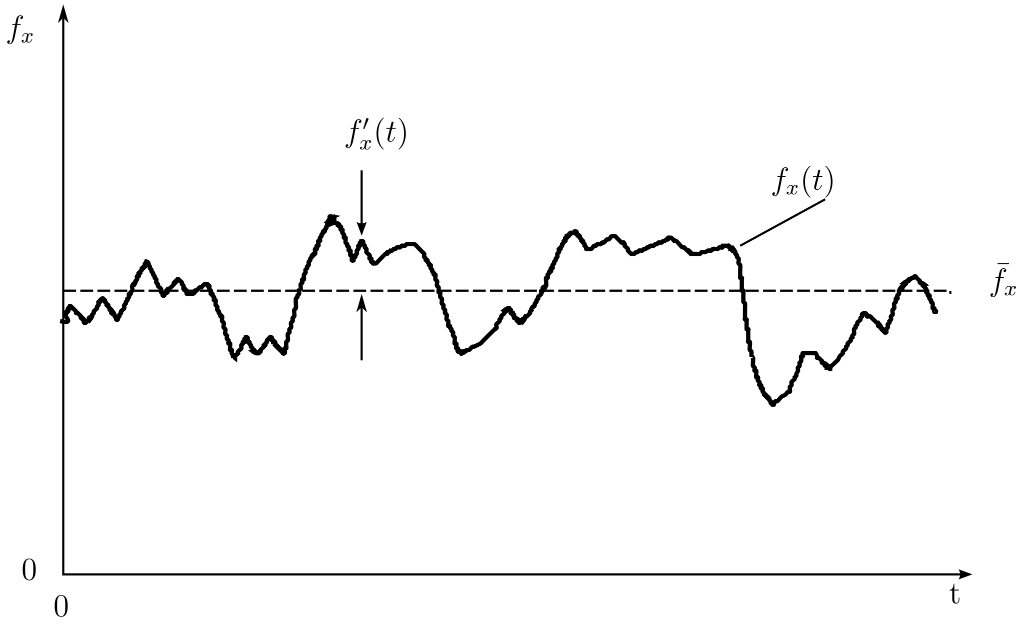

Figure 2.1: Fluctuations of a variable f over time.

2.2 Turbulence Theory

In technical applications almost all flows are turbulent whereas laminar flows play a important role in many generic theoretical investigations [14]. To separate between turbulent and laminar flows, a dimensionless Reynolds number Re [60] is used, which is composed of a velocity u, a characteristic length l and the kinematic viscosity ν.

$$Re = \frac{ul}{\nu} \tag{2.10}$$

For small Re-numbers any fluctuation in the velocity field is immediately damped by viscous forces of the fluid. In a stationary flow, the mean velocity $\bar{u}_i$ is identical to the instantaneous velocity $u_i(t)$ and the flow is laminar. With increasing Re-number the fluctuations grow and the mean velocity differs from the instantaneous velocity. Thus, $u_i(t) = \bar{u}_i + u'_i$, where u'_i denotes the fluctuation in velocity and the flow is turbulent.

Exemplarily, figure 2.1 shows fluctuations f'_x of f_x over time t. In principle the curve displaying fluctuating values in figure 2.1 is also valid for all transported variables, like temperature for example.

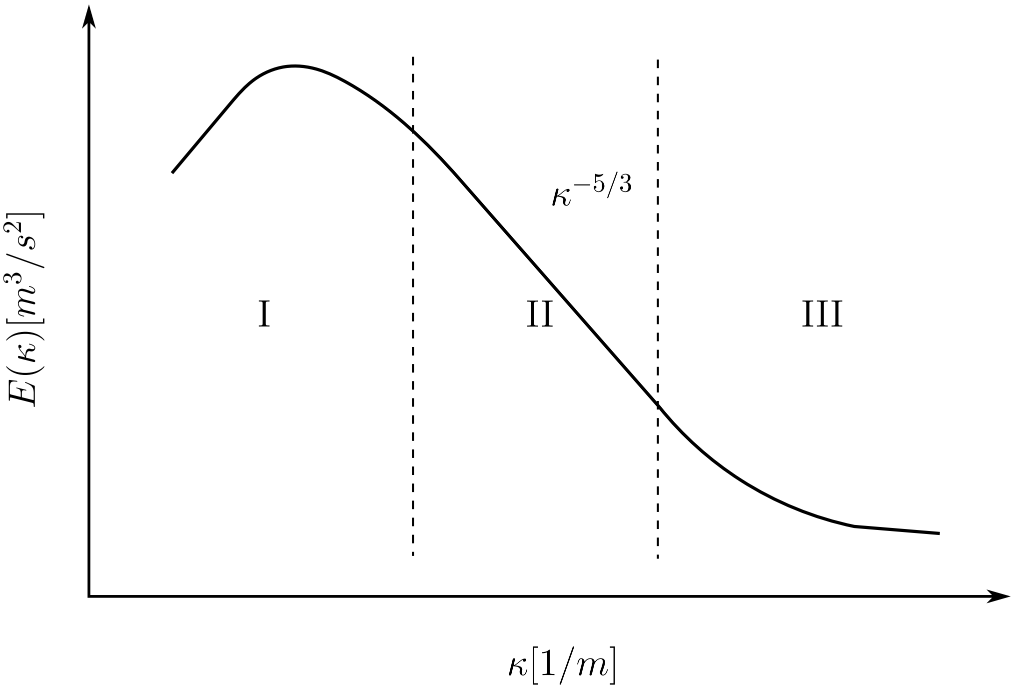

Figure 2.2: Spectrum for turbulent kinetic energy dependent on the wave number.

The kinetic energy of the velocity fluctuations in all directions sums up to the turbulent kinetic energy,

$$k = \frac{u_x'^2 + u_y'^2 + u_z'^2}{2} \tag{2.11}$$

which can be used to calculate a mean velocity fluctuation under the assumption of isotropic turbulence:

$$u_i' = \sqrt{\frac{2}{3}k}. \tag{2.12}$$

The model of eddies and corresponding wave numbers is an option to describe turbulence fluctuations, which are basically vortices having a certain radius. The wave number corresponds to the circumference of the vortices. All eddies can be sorted by their wave number. In figure 2.2, the energy contained in the different eddies is displayed. It can be distinguished between three different regions [14].

The region I in figure 2.2 contains the biggest eddies with most of the energy. These eddies extract their energy from the mean flow and can build coherent structures. These largest eddies can also be characterized by the integral length scale l_t and its corresponding integral time scale $t_t \approx \frac{l_t}{u'_{RMS}}$. Based on the integral length scale a turbulent Reynolds number can be defined in analogy to equation 2.10:

$$Re_t = \frac{u' l_t}{\nu}. \tag{2.13}$$

The energy of the larger eddies is then transferred to subsequent eddies.

From region I energy is transferred to region II. In region II a transfer of energy from larger to smaller eddies takes place. In this cascade process, the energy transfer per time unit is given by ϵ. As the cascade concept assumes only energy transfer from larger to smaller scales, the number of eddies increases because the total energy at each wave number must be constant. Together with the wave number of the eddies, the energy in this region can be computed by

$$E(\kappa) = C \cdot \epsilon^{\frac{2}{3}} \kappa^{-\frac{5}{3}}. \tag{2.14}$$

Equation 2.14 is also known as the Kolmogorov spectrum law.

While the energy per eddy decreases with decreasing wave number, the viscous stress gets large in comparison to the kinetic energy per eddy. The turbulent kinetic energy of eddies in region III in figure 2.2 is transformed into thermal energy. The length scale characterizing this process of energy conversion is the Kolmogorov length scale l_η and Kolmogorov time scale t_η.

$$l_\eta = \left(\frac{\nu^3}{\epsilon}\right)^{1/4} \tag{2.15}$$

$$\tau_\eta = \left(\frac{\nu}{\epsilon}\right)^{1/2} \tag{2.16}$$

2.3 Combustion Theory

2.3.1 Basic Combustion Principle

In general, combustion describes the exothermic oxidation of fuel by oxygen. The stoichiometric conversion follows equation 2.17.

$$\nu_1'\mathrm{S}_1 + \nu_2'\mathrm{S}_2 + \ldots \rightarrow \nu_1''\mathrm{S}_3 + \nu_2''\mathrm{S}_4 + \ldots \tag{2.17}$$

At stoichiometric conditions the exact amount of oxygen needed to oxidate the fuel totally is provided. Therefore, no unburnt fuel and no oxygen exist in the product in the ideal case. Exemplarily, this is shown for methane as fuel in equation 2.18.

$$\mathrm{CH_4} + 2\mathrm{O_2} \rightarrow \mathrm{CO_2} + 2\mathrm{H_2O} \tag{2.18}$$

In technical applications the amount of oxygen often differs from the stoichiometric value. In this thesis, the equivalence ratio Φ is used to describe the fuel/oxygen ratio. Φ is defined as the fuel/oxidizer ratio divided by the stoichiometric fuel/oxidizer [24].

In an exothermic reaction the enthalpy at standard conditions (1,013 bar and 293 K) of the products on the right hand side of equation 2.17 is higher than the enthalpy at the same conditions of the reactants on the left hand side [1].

$$\Delta H_R^0 = H_{Prod}^0 - H_{Reac}^0 \tag{2.19}$$

Equation 2.18 shows the global reaction mechanism of methane combustion. This global mechanism is a simplification of the real chemical processes consisting of many intermediate processes which involve a lot more species and reaction steps. As the consequence different reaction paths and backward reactions have to be considered to capture the combustion process adequately. All these reactions and species can be written in a compact notation [67]:

$$\sum_{\mathrm{k=1}}^{\mathrm{N_{species}}} \nu_{\mathrm{ki}}'\mathrm{S_k} \leftrightarrow \sum_{\mathrm{k=1}}^{\mathrm{N_{species}}} \nu_{\mathrm{ki}}''\mathrm{S_k}, \tag{2.20}$$

where the index k represents the k-th species and the subscript i is for the i-th equation in the detailed reaction scheme. The number of involved species and reactions varies. For example the Leeds Mechanism 1.5 uses 37 species and 175 reactions [33] whereas another mechanism from Gallway consists of 118 species and 663 reactions [56]. In this thesis, the GRI3.0

with 53 species and 325 reactions [65] is used to compute reference values as it is widely used for investigations concerning NO_x emissions. A variety of simplified mechanisms exists in between these quite large schemes and the net reaction shown in equation 2.18. In preliminary CFD investigations, different simplified mechanisms are evaluated concerning the source term for finite rate combustion models: the one step mechanism including four species and the two step mechanism using five species from Westbrook and Dryer [70] as well as the two step mechanism with five species from Biberitzky et al. [3].

Experimental investigation confirmed the model of law of mass action [24] implied in the formulations from equation 2.17-2.20. These species are formed at the same speed as their predecessors are consumed. Thus, the rate of formation of species i can be expressed as product of reactant concentrations to the power of their stoichiometric coefficient multiplied by a proportional constant:

$$RR_i = k(T) \prod_{j=0}^{N} X_j^{\nu'_j}. \tag{2.21}$$

The change in concentration of species k is calculated using all production and destruction terms as chemical reactions takes place in both directions. In combination with equation 2.21 the concentration change over time can be written in the following way:

$$\frac{d[X_i]}{dt} = [\nu''_i - \nu'_i]\, k(T) \prod_{j=0}^{N} [X_j]^{\nu'_j}. \tag{2.22}$$

The product concentration used here can be calculated by

$$[X_k] = \frac{n_k}{V} = \frac{p_k}{R_u T} = \frac{X_k p_{tot}}{R_u T}. \tag{2.23}$$

As long as the ideal gas law is valid, the partial pressure can be computed directly by the mole fraction of species k:

$$X_k = \frac{n_k}{n_{ges}}. \tag{2.24}$$

Alternatively, the mass fraction (Equation 2.25) can be used to compute the mole fraction of species k (Equation 2.26).

$$Y_k = \frac{m_k}{m_{ges}} \tag{2.25}$$

$$X_k = Y_k \frac{M_{mean}}{M_k} \tag{2.26}$$

The last unknown variable is the proportional constant k. As indicated by T, the proportional factor strongly depends on the temperature. This factor is approximated by the Arrhenius equation

$$k = AT^n e^{-E_A/(R_u T)} \tag{2.27}$$

using the activation energy E_A and the temperature T. Additionally, a proportional factor A is used. In most cases, the exponent of the temperature n is equal to zero such that the term T^n is neglected. Details on the basic principles of the Arrhenius approach can be taken from [24]. The values for A, n and E_A for the corresponding reaction schemes are listed in Appendix B.

2.3.2 Chemical Reactor Theory

To investigate a reacting composition over a time period in detail, the basic conservation equations of mass and energy are coupled with chemical kinetics. Considering only systems where diffusion can be neglected because of a uniform distribution all over the domain, the analysis stays simple.

There are several ideal reactors discussed in literature, which fulfill a perfectly mixedness [1, 67]. The simplest ideal reactors are closed systems, where the mass is constant over time and only the pressure or the volume changes. These reactors are called constant volume, fixed-mass reactors and constant pressure, fixed-mass reactors. A more sophisticated setup is a perfectly stirred reactor, also known as well stirred reactor. In this setup the species composition within the reactor is not time dependent as it operates at steady state. The PSR reactor has the same amount of inflow and outflow mass stream but in opposite directions. Within the control volume, the reactor is perfectly mixed. A fourth reactor of perfectly mixedness, at least in radial direction is a plug flow reactor. This can be understood as a series of PSR where one PSR gets the input from the reactor before and provides the input to the next reactor by its output.

Generally, a chemical reactor is fully described by the continuity and energy equation shown in equation. 2.28 and equation. 2.29.

Continuity

$$\frac{dm}{dt} = \sum_{in} \dot{m}_{in} - \sum_{out} \dot{m}_{out} + \dot{m}_{wall} \tag{2.28}$$

Energy

$$\frac{dU}{dt} = -p\frac{dV}{dt} - \dot{Q} + \sum_{in} \dot{m}_{in} h_{in} - h \sum_{out} \dot{m}_{out} \tag{2.29}$$

In this thesis, the computational tool to calculate a chemical reactor is Cantera [26]. In this software, each reactor is described by the continuity and energy conservation equation from above incorporating the ideal gas law. The sort of reactor type is not defined by the formulation of the equations (these are always similar, not depending on the reactor type) but by the definition of the boundary conditions.

The fixed mass constant pressure reactor, which is widely used in this thesis, is based on equations 2.30 and 2.31. The derivation of both equations can be found in section A of the Appendix.

$$\frac{dY_k}{dt} = \frac{\dot{m}_{k,gen}}{m} \tag{2.30}$$

$$mc_p\frac{dT}{dt} = -\dot{Q} - \sum_{k} h_k \dot{m}_{k,gen} \tag{2.31}$$

2.3.3 Laminar and Turbulent Flames

As combustion is controlled by thermal diffusion and mass diffusion the flat flame is another suitable model. Here, combustion is described as a freely propagating, premixed flame at constant pressure. The setup of the zero dimensional test cases is extended to a one dimensional problem. Furthermore, a momentum equation and species equations are introduced which also take convection and diffusion terms into account. As the resulting system grows with an increasing number of involved species, efficient solution algorithms are needed for the stiff system of equations.

In the laminar freely propagating flame with an equivalence ratio Φ the reactants are consumed with its laminar flame speed s_l. This value gives the velocity where the flame moves through the fresh gas and consumes it. Depending on the laminar flame speed a chemical time scale t_c can be defined which represents the time needed to convert the fuel-air mixture. Flame speed and chemical time scale correlate with each other according to equation 2.32

$$s_l = \frac{\delta_l}{t_c} \tag{2.32}$$

The correlation factor δ_l can be interpreted as the laminar flame thickness.

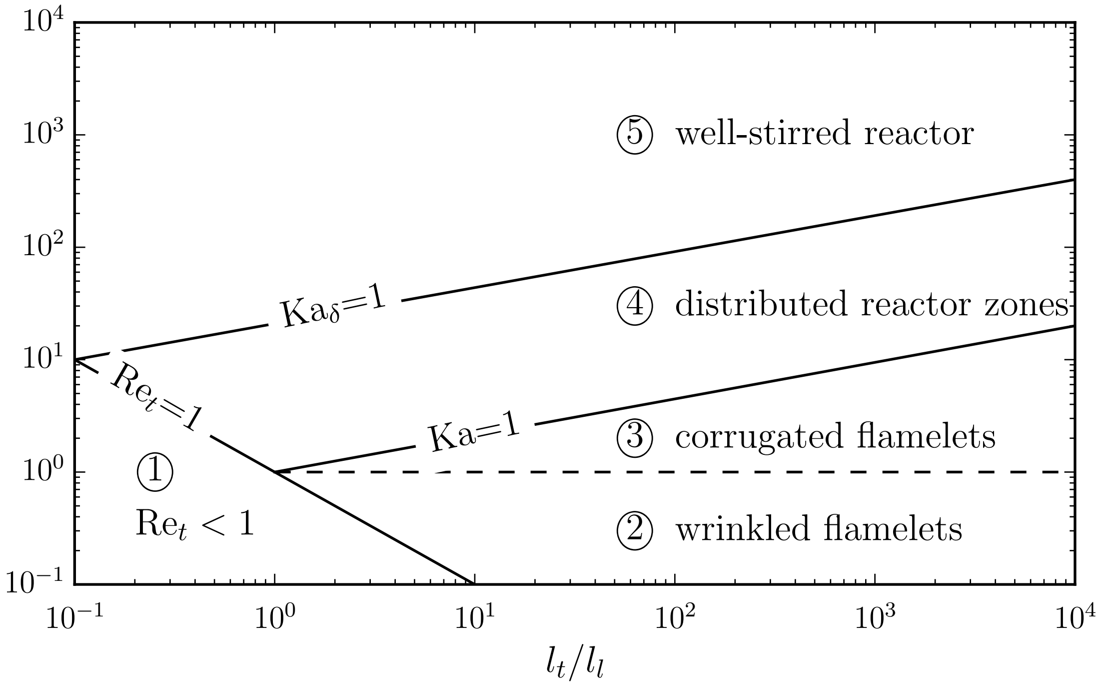

Figure 2.3: Diagram of Borghi and Peters showing the different combustion regimes [4], [55].

When characterizing the interaction of turbulence and flame propagation two dimensionless numbers are used [58]. The Damkoehler number Da compares the integral time scale and the chemical time scale.

$$Da = \frac{t_t}{t_c} \tag{2.33}$$

Further, the Karlovitz number Ka shows the relationship between chemical time scale and Kolmogorov time scale,

$$Ka = \frac{t_c}{t_\eta}. \tag{2.34}$$

The diagram 2.3, originally developed by Borghi [4] and later modified by Peters [55], shows different premixed flame types depending on the dimensionless numbers from equations 2.13, 2.33 and 2.34.

Different turbulence levels provide different flame shapes. For $u'/s_l < 10$, $l_t/l_l < 10$ and $Re_t < 1$ flames are laminar and no turbulence is present. With increasing turbulence level, the flame becomes wrinkled (region 2). Increasing the turbulence further, the flame becomes corrugated, displayed in region 3 in figure 2.3. At even higher turbulence a further increase in flame surface area takes place, resulting in distributed reaction zones, represented by region 4. Finally, the flame as defined earlier can no longer exist and a well stirred reactor develops in region 5.

2.3.4 Formation of Nitrogen Oxides

During a combustion process not only fuel is oxidized to its products, but also side products are formed. One group of side products are nitrogen oxides. This group mainly consists of nitrogen oxide (NO) and nitrogen dioxide (NO_2). Only NO and NO_2 are of technical relevance and are usually grouped to NO_x.

The formation of NO occurs via several pathways. Four of them are considered in this thesis: the thermal pathway of Zeldovich, the prompt path way of Fenimore, the pathway of intermediate N_2O and finally the pathway of NNH. As only methane is used as fuel which does not contain any nitrogen. Only nitrogen included in the air can contribute to NO_x formation.

The Zeldovich mechanism describes the formation of NO at high temperatures by two chain reactions,

$$\mathrm{N_2 + O \leftrightarrow N + NO}, \tag{2.35}$$

$$\mathrm{N + O_2 \leftrightarrow NO + O}. \tag{2.36}$$

These two reactions are extended by

$$\mathrm{N + OH \leftrightarrow NO + H}. \tag{2.37}$$

Reactions 2.35 and 2.36 together with reaction 2.37 are known as thermal NO mechanism or extended Zeldovich mechanism [67]. Both O and OH are important for the fuel oxidation process, as described by Smith et al. [65]. Therefore the thermal NO generation is coupled with the fuel conversion process. Zeldovich suggests to separate both from each other, because the amount of formed NO is very small compared to the oxidation products [52]. Instead of coupling, an equilibrium approach can be used for the radicals. The incorporated error is small [52] and justifies the simplification.

The dissociation process of N_2 because of its quite large activation energy, strongly depends on temperature. Furthermore, the time scale of NO formation is large compared to the fuel oxidation process. Because of the temperature dependence and reaction speed, the extended Zeldovich mechanism is used for the post flame region, although the thermal mechanism starts right away in the flame.

The Fenimore mechanism is closely linked to hydrocarbon oxidation. Therefore this NO mechanism is also known as prompt NO pathway and occurs directly within the flame before thermal NO is formed in significant amounts. The pathway is quite complicated and depends on the equivalence ratio. Neglecting the formation of CH the main steps can be written as

$$\mathrm{CH + N_2 \leftrightarrow HCN + N} \tag{2.38}$$

$$\mathrm{C + N_2 \leftrightarrow CN + N} \tag{2.39}$$

where reaction 2.38 represents the rate limiting step. The following main reaction sequence dominates for $\Phi < 1.2$:

$$\mathrm{HCN + O \leftrightarrow NCO + H} \tag{2.40}$$

$$\mathrm{NCO + H \leftrightarrow NH + CO} \tag{2.41}$$

$$\mathrm{NH + H \leftrightarrow N + H_2} \tag{2.42}$$

$$\mathrm{N + OH \leftrightarrow NO + H} \tag{2.43}$$

Beside these reactions also other pathways are relevant for the formation of prompt NO. Details can be found in Miller and Bowman [52].

The N_2O intermediate mechanism plays an important role for fuel lean, premixed flames, where generally small amounts of NO_x are produced. Less hydrocarbon particles are available and the prompt mechanism gets inhibited. At the same time, the temperature decreases and less NO is formed by the thermal pathway. For low values of Φ ($\Phi < 0.8$), the following pathway gets more important:

$$\mathrm{O + N_2 + M \leftrightarrow N_2O + M} \tag{2.44}$$

$$\mathrm{H + N_2 \leftrightarrow NO + NH} \tag{2.45}$$

$$\mathrm{O + N_2O \leftrightarrow NO + NO} \tag{2.46}$$

The last mechanism taken into account for the formation of NO is limited to the NNH radicals, which form NO during their oxidation. The process is described by

$$\mathrm{N_2 + H \leftrightarrow NNH} \tag{2.47}$$

$$\mathrm{NNH + O_2 \leftrightarrow NO + OH} \tag{2.48}$$

and mainly contributes to NO production in the flame zone. This pathway is not investigated as far as the other three mechanisms mentioned earlier, but the NNH pathway currently gets more prominent [24]. At least for short residence times with temperatures between 1000 K and 2200 K this pathway significantly contributes to NO production independent of equivalence ratios [42].

3 Modeling of Reacting Flows

3.1 Direct Numerical Simulation

If the Navier Stokes equations 2.1 and 2.2 and the corresponding energy equation 2.6 are solved by Direct Numerical Simulation (DNS), turbulence is not modeled, but fully simulated. All turbulence scales must be resolved by the computational mesh. Using the theoretical ratio between smallest and largest turbulence scale of $Re^{3/4}$ a Reynolds number of 10^4 (which is a lot smaller than the Re numbers for reacting jets in crossflow of interest in practice) will result in 10^3 points in each direction and a total mesh of 10^9 cells. Along with this fact, the number of time steps can be estimated by a minimum of 100, which accounts for the ratio from smallest to largest timescale of $Re^{1/2}$ [68]. The time needed for one time step multiplied by the necessary time steps to resolve the given technical problem can hardly be run on any super computer.

Adding combustion to the DNS results in an even more expensive setup. The number of species involved in the combustion process increases the number of transported variables. In addition, a sufficient model for the calculation of the diffusion coefficients consumes huge amount of resources. The flame itself adds also a restriction to the cell size as the flame must be resolved at least with about 20 grid points [58]. Assuming a flame thickness of 0.5 mm for a hydrocarbon flame and standard conditions, and taking the total mesh size from above of 10^9 cells, only a cube with an edge length of 25 mm can be sufficiently resolved. The specification of the boundary conditions are also challenging, which can not be cyclic as it is often in non combustion cases. Therefore elaborate approaches have to be used to get rid of this boundary problem.

For these reasons described DNS cannot be applied to the technical application.

3.2 Reynolds Averaged Navier Stokes Simulation

Compared to the DNS, the Reynolds Averaged Navier Stokes (RANS) approach is an efficient method to reduce the computational effort needed for a simulation. The RANS concept uses the mass, momentum and energy equations, and decomposes each transported variable f into a mean value $\overline{f}$ and a fluctuating component f' [68]. Substituting f by mean and fluctuation in equations 2.1, 2.2 and 2.6 will lead to a number of unresolved terms like $\overline{\rho' u_i'}$ which must be modeled. The Favre average $\widetilde{f}$ is used, also known as density weighted average, to solve this problem. It is defined by

$$\widetilde{f} = \frac{\overline{\rho f}}{\overline{\rho}}, \tag{3.1}$$

which leads to the decomposition $f = \widetilde{f} + f'$ where $\widetilde{f'} = 0$. Putting it into the conservation equations, the RANS equations are obtained as follows:

$$\frac{\partial \overline{\rho}}{\partial t} + \frac{\partial \overline{\rho}\widetilde{u_i}}{\partial x_i} = 0, \tag{3.2}$$

$$\frac{\partial \overline{\rho}\widetilde{u_i}}{\partial t} + \frac{\partial \overline{\rho}\widetilde{u_i}\widetilde{u_j}}{\partial x_i} = -\frac{\partial \widetilde{p}}{\partial x_j} + \frac{\partial \overline{\tau_{ij}}}{\partial x_i} - \frac{\partial \overline{\rho}\widetilde{u_i' u_j'}}{\partial x_i}, \tag{3.3}$$

$$\begin{aligned} \frac{\partial \overline{\rho}\widetilde{h}_s}{\partial t} + \frac{\partial \overline{\rho}\widetilde{u_i}\widetilde{h}_s}{\partial x_i} = {} & \frac{\partial \overline{p}}{\partial t} + \widetilde{u_i}\frac{\partial \overline{p}}{\partial x_i} + \overline{u_i' \frac{\partial p}{\partial x_i}} + \overline{\tau_{ij}\frac{\partial u_i}{\partial x_j}} - \\ & \frac{\partial}{\partial x_i}\left(\overline{\lambda \frac{\partial T}{\partial x_i}} - \overline{\rho}\widetilde{u_i' h_s'} - \overline{\rho \sum_{k=1}^{N} h_k Y_k V_{k,i}} \right) + \overline{\rho}\overline{\dot{\omega}_{h_s}}, \end{aligned} \tag{3.4}$$

$$\frac{\partial \overline{\rho}\widetilde{Y_k}}{\partial t} + \frac{\partial}{\partial x_i}\left(\overline{\rho}\widetilde{u_i}\widetilde{Y_k} + \overline{V_{k,i} Y_k} + \overline{\rho}\widetilde{u_i' Y_k'}\right) = \overline{\dot{\omega}_k}. \tag{3.5}$$

Several unresolved terms appear within these equations by the averaging process. The laminar diffusion of species can be approximated by $\overline{V_{k,i} Y_k} \approx \overline{\rho}\overline{D_k}\frac{\partial \widetilde{Y_k}}{\partial x_i}$, the laminar diffusion flux of the heat can be calculated by $\overline{\lambda \frac{\partial T}{\partial x_i}} = \overline{\rho}\frac{\partial \widetilde{T}}{\partial x_i}$. The turbulent fluxes of enthalpy and species are modeled by a gradient approach

$$\overline{\rho}\widetilde{u_i' h_s'} = -\frac{\mu_t}{Pr_t}\frac{\partial \widetilde{h_s}}{\partial x_i} \quad \mathit{and} \quad \overline{\rho}\widetilde{u_i' Y_k'} = -\frac{\mu_t}{Sc_t}\frac{\partial \widetilde{Y_k}}{\partial x_i} \tag{3.6}$$

using a turbulent Schmidt number Sc_t for the fluxes of the species and a turbulent Prandtl number Pr_t for enthalpy. The turbulent viscosity depends on the turbulence model, which is used to close the Reynolds stress term $\widetilde{u_i'' u_j''}$ by the classical Boussinesq approach:

$$\overline{\rho}\widetilde{u_i' u_j'} = -\mu_t \left(\frac{\delta \widetilde{u}_i}{\delta x_j} + \frac{\delta \widetilde{u}_j}{\delta x_i} + \frac{2}{3}\delta_{ij}\frac{\delta \widetilde{u}_k}{\delta x_k} \right) + \frac{2}{3}\overline{\rho}k \tag{3.7}$$

Equation 3.7 is basically the viscous tensor τ_{ij}. Solutions of different complexity were proposed to model the turbulent viscosity. There are models with no additional transport equation like Prandtl mixing length, one equation models (Prandtl-Kolmogorov) and two equation models like k - ϵ model [68].

RANS is suitable for stationary problems, but it can also be used to treat time dependent problems. For time dependent problems it is known as unsteady RANS, URANS. But URANS still assumes a fully isotropic turbulence. In the presented case, this is not feasible. Therefore, RANS or URANS simulations are not suitable, but can still provide a useful initial solution for LES.

3.3 Large Eddy Simulation

A different approach to DNS and RANS modeling is to separate large turbulent scales from the small, isotropic ones and simulate only the large eddies while the small isotropic eddies are modeled. This type of simulation is known as Large Eddy Simulation (LES). In contrast to RANS, where time averaging is applied, in LES the filter operates in space. Therefore, LES is from the start time dependent. As the simulated turbulence scales are not isentropic, a three dimensional mesh is required.

Starting with the Navier Stokes equation 2.1 and 2.2, the field f is filtered retaining the large scales and rejecting the small ones.

$$\widehat{f}(\mathbf{x},t) = \int f(\mathbf{x}',t)G(\mathbf{x}-\mathbf{x}')d\mathbf{x}' \tag{3.8}$$

G represents the filter kernel and $\widehat{(\ )}$ symbolizes the filtered variable. The properties of a filter kernel itself must be consistency, $\int_{-\infty}^{\infty} G(\mathbf{x})d(\mathbf{x}) = 1$, linearity to guarantee $\widehat{f+g} = \widehat{f} + \widehat{g}$ and exchangeability of the time operator $\frac{\widehat{\partial f}}{\partial t} = \frac{\partial \widehat{f}}{\partial t}$ and the space operator $\frac{\widehat{\partial f}}{\partial x_i} = \frac{\partial \widehat{f}}{\partial x_i}$. Exchangeability is only valid for a constant filter width Δ for the whole domain. The filtering process in OpenFOAM is implicit and linked to the computational grid, which applies to most CFD codes. Therefore, the property of commutation in space is not satisfied. But if the the filter length evolves smoothly, the introduced error is small.

Theoretically, different filter types like the cut-off filter, the box filter or the Gauss filter can be applied. In OpenFOAM the box filter shown in equation 3.9 is applied by default in a first filtering process.

$$G(\mathbf{x}) = \begin{cases} 1/\Delta^3 & \text{if } |\mathbf{x_i}| \leq \Delta/2 \quad, i = 1,2,3 \\ 0 & \text{otherwise} \end{cases} \tag{3.9}$$

For the density changes within the combustion process, again a density weighted Favre filter is introduced [58].

$$\widehat{\rho f} = \widehat{\rho}\widetilde{f} = \int \rho f(\mathbf{x}', t) G(\mathbf{x} - \mathbf{x}') d\mathbf{x}' \tag{3.10}$$

Thus, the value of a variable f can be decomposed into a sum of filtered and subgrid values.

$$f(x,t) = \widetilde{f}(x,t) + f'(x,t) \tag{3.11}$$

Filtering and Favre averaging are applied to the conservation equations 2.1, 2.2, 2.4 and 2.6:

$$\frac{\partial \widehat{\rho}}{\partial t} + \frac{\partial \widehat{\rho}\widetilde{u}_i}{\partial x_i} = 0 \tag{3.12}$$

$$\frac{\partial \widehat{\rho}\widetilde{u}_i}{\partial t} + \frac{\partial \widehat{\rho}\widetilde{u}_i\widetilde{u}_j}{\partial x_i} + \frac{\partial \widehat{p}}{\partial x_j} = \frac{\partial \widehat{\tau}_i j}{\partial x_i} - \frac{\partial}{\partial x_i}\left(\widehat{\rho}\widetilde{u_i u_j} - \widehat{\rho}\widetilde{u}_i\widetilde{u}_j\right) \tag{3.13}$$

$$\frac{\partial \widehat{\rho}\widetilde{Y}_k}{\partial t} + \frac{\partial \widehat{\rho}\widetilde{u}_i\widetilde{Y}_k}{\partial x_i} = -\frac{\partial}{\partial x_i}\left[\widehat{V_{k,i}Y_k} + \widehat{\rho}\left(\widetilde{u_i Y_k} - \widetilde{u}_i\widetilde{Y}_k\right)\right] + \widehat{\dot{\omega}}_k \tag{3.14}$$

$$\begin{aligned} \frac{\partial \widehat{\rho}\widetilde{h}_s}{\partial t} + \frac{\partial \widehat{\rho}\widetilde{u}_i\widetilde{h}_s}{\partial x_i} = \frac{\partial \widehat{p}}{\partial t} + \widehat{u_i\frac{\partial p}{\partial x_i}} + \frac{\partial}{\partial x_i}\left[\widehat{\lambda\frac{\partial T}{\partial x_i}} - \widehat{\rho}\left(\widetilde{u_i h_s} - \widetilde{u}_i\widetilde{h}_s\right)\right] \\ + \widehat{\tau_{ij}\frac{\partial u_i}{\partial x_j}} - \frac{\partial}{\partial x_i}\left(\widehat{\rho \textstyle\sum_{k=1}^{N} V_{k,i}Y_k h_{s,k}}\right) + \widehat{\dot{\omega}}_T \end{aligned} \tag{3.15}$$

Again, after the filtering several unresolved terms appear that must be modeled or estimated. The Reynolds stress term $\widehat{\rho}\widetilde{u_i u_j} - \widehat{\rho}\widetilde{u}_i\widetilde{u}_j$ will be resolved by a sub grid turbulence model. The unresolved species flux $\widetilde{u_i Y_k} - \widetilde{u}_i\widetilde{Y}_k$ can be approximated by Fick's law using a sub grid diffusion coefficient which is calculated from the sub grid viscosity μ_{sgs} and a sub grid Schmidt number Sc_t:

$$\widetilde{u_i Y_k} - \widetilde{u}_i\widetilde{Y}_k = -\frac{\mu_{sgs}}{Sc_t}\frac{\partial\widetilde{Y}_k}{\partial x_i}. \tag{3.16}$$

The unresolved enthalpy flux $\widetilde{u_i h_s - \widetilde{u}_i\widetilde{h}_s}$is calculated in analogy to RANS but using the sub grid viscosity μ_{sgs}.

$$\widetilde{u_i h_s} - \widetilde{u}_i\widetilde{h}_s = -\frac{\mu_{sgs}}{Pr_t}\frac{\partial\widetilde{h}_s}{\partial x_i}. \tag{3.17}$$

Beside these fluxes, the filtered laminar flux for species can be approximated by $\widehat{V_{k,i}Y_k} = -\widehat{\rho}\frac{\mu}{Sc}\frac{\partial\widetilde{Y_k}}{\partial x_i}$ and the filtered laminar flux for enthalpy by $\widehat{\lambda\frac{\partial T}{\partial x_i}} = \lambda\frac{\partial\widehat{T}}{\partial x_i}$. The pressure velocity coupling is approximated by $\widehat{u_i\frac{\partial p}{\partial x_i}} = \widehat{u_i}\frac{\partial\widehat{p}}{\partial x_i}$. The filtered source term, which is a priory not given, is delivered by the combustion model of choice (section 3.4).

Different models for the Reynolds stress term have been published. An overview is given by Versteeg and Malalasekera [68]. In this thesis a model based on the Boussinesq eddy viscosity hypothesis, known as Smagorinsky model [64] is used. The authors suppose, that the sub grid scale Reynolds stress tensor $\widehat{\tau_i j}^{SGS} = -\widehat{\rho}\left(\widetilde{u_i u_j - \widetilde{u}_i\widetilde{u}_j}\right)$ is proportional to the resolved shear stress tensor by a scaling factor μ_{sgs}, which can be interpreted as sub grid viscosity.

$$\widehat{\tau}_{ij}^{SGS} - \frac{\delta_{ij}}{3}\widehat{\tau}_{kk}^{SGS} = -\mu_{SGS}\left(\frac{\partial\widehat{u}_i}{\partial x_j} + \frac{\partial\widehat{u}_j}{\partial x_i}\right) = -2\mu_{SGS}\widehat{S}_{ij} \tag{3.18}$$

This sub grid viscosity is computed based on the theory of Prandtl's mixing length consisting of a constant C_s (≈ 0.2), the filter width Δ, the integral length scale l_t and the averaged strain rate $|S_{ij}|$:

$$\mu_{sgs} = \widehat{\rho}C_s^2\Delta^{4/3}l_t^{2/3}|\widehat{S}| = \widehat{\rho}C_s^2\Delta^2\sqrt{\widehat{S}_{ij}\widehat{S}_{ij}} \tag{3.19}$$

On the sub grid scale, the integral length scale can be replaced by the filter width, displayed in the rightmost term in equation 3.19. A disadvantage of this approach is the constant C_s which must be determined in advance. To solve the problem, a dynamic calculation of the constant has been proposed in [23, 47]. Basically a second filtering is applied after the first filtering assuming the same value for C_s. Afterwards, the difference in the stress tensor between the two filtering steps is compared to the test filter, in order to calculate a corresponding scaling constant C_s. Further details can be found in [47].

In the context of LES suitable boundary conditions are a key feature. Especially a correct choice of the boundary condition for the turbulent fluctuations is difficult since the fluctuations must be consistent with the energy spectra. Without a correct distribution of the energy, the fluctuations will immediately dissipate. Therefore, an incorrect turbulent boundary condition is one of the major reasons why simulations fail to predict experiments correctly [51]. In the presented setup, the turbulent fluctuations are calculated using a precursor field according to Kempf and Klein [39]. Details are given in section C in the appendix.

3.4 LES Premixed Combustion Modeling

In this section a short overview of existing combustion models is given, which are used in LES. The reason for modeling the combustion process and not computing it directly, as mentioned in section 2.3, is computational cost. In addition, the computational mesh of a LES is not able to resolve the flame front. Tightening the grid is directly proportional to the computational costs. Even more important is the stiffness of the complex reaction schemes, which forces small time steps and hence increases computational costs further.

Nevertheless, for the species equation 3.14 the source term $\widehat{\dot{\omega}}_k$ from combustion is needed. To calculate $\widehat{\dot{\omega}}_k$, different simplified approaches are common, grouped into four categories. There are finite rate models, turbulent mixing length assumptions, flame surface density models and probability density function (PDF) models.

3.4.1 Overview of Combustion Models

Probability Density Function Model

Starting with the last group of combustion models, a probability density function is used to close the balance equations and calculate the filtered source term. Theoretically, the mass fractions and their moments are used to calculate the filtered source term. This procedure is quite expensive. For each involved species at least one additional balance equation for its fluctuation must be solved. Thus, the combustion process is simplified by two variables, mixture fraction Z and progress variable C:

$$Z = \frac{sY_f - Y_o + Y_{o,0}}{sY_{f,0} + Y_{o,0}}, \tag{3.20}$$

$$C = \frac{Y_{CO_2} - Y_{CO_2,0}}{Y_{CO_2,eq} - Y_{CO2,0}}. \tag{3.21}$$

In a strictly premixed case, the mixture fraction may be omitted. For a partially premixed case also the mixture fraction is of interest, as it can change with time and location. Therefore, four balance equations must be considered:

$$\frac{\partial \widehat{\rho}\widetilde{C}}{\partial t} + \frac{\partial \widehat{\rho}\widetilde{u}_i\widetilde{C}}{\partial x_i} = -\frac{\partial}{\partial x_i}\left[D_k \frac{\partial \widehat{\rho}\widetilde{C}}{\partial x_i}\right] + \widehat{\dot{\omega}}_C \tag{3.22}$$

$$\frac{\partial \widehat{\rho}\widetilde{C}''}{\partial t} + \frac{\partial \widehat{\rho}\widetilde{u}_i\widetilde{C}''}{\partial x_i} = -\frac{\partial}{\partial x_i}\left[D_k \frac{\partial \widehat{\rho}\widetilde{C}''}{\partial x_i}\right] - 2D_k\rho\widehat{\frac{\partial C}{\partial x_i}\frac{\partial C}{\partial x_i}} + 2\widehat{C\dot{\omega}}_C \tag{3.23}$$

$$\frac{\partial \widehat{\rho}\widetilde{Z}}{\partial t} + \frac{\partial \widehat{\rho}\widetilde{u}_i\widetilde{Z}}{\partial x_i} = -\frac{\partial}{\partial x_i}\left[D_k \frac{\partial \widehat{\rho}\widetilde{Z}}{\partial x_i}\right] \tag{3.24}$$

$$\frac{\partial \widehat{\rho}\widetilde{Z}''}{\partial t} + \frac{\partial \widehat{\rho}\widetilde{u}_i\widetilde{Z}''}{\partial x_i} = -\frac{\partial}{\partial x_i}\left[D_k \frac{\partial \widehat{\rho}\widetilde{Z}''}{\partial x_i}\right] - 2D_k\rho\widehat{\frac{\partial Z}{\partial x_i}\frac{\partial Z}{\partial x_i}} \tag{3.25}$$

Using the mixture fraction and the progress variable together with a PDF, the filtered source term $\widehat{\dot{\omega}}_C$ can be computed from:

$$\widehat{\dot{\omega}}_C = \widehat{\rho}\int_0^1 \frac{\omega_C}{\rho} P(C)P(Z)dCdZ. \tag{3.26}$$

The probability density function P must be given for this step. The approaches for treating the probability density function P differ between presumed shape PDF and a transported PDF approach. A widely used PDF function for the presumed PDF is the β-function as shown by Huang and Lipatnikov [32]. A more complicated approach is the transported PDF, which is calculated during simulation as explained by Harworth [30]. An application of the transported PDF can be found in Kulkarni [43], where the PDF is calculated from a series of different possible compositions of each cell.

The PDF approach provides turbulence flame interaction because the subscale fluctuations are taken into account. Nevertheless, the transport equations for mean and variance generate unclosed terms. These must be resolved by appropriate models. Further, the independence of progress variable and mixture fraction is questionable. However, for the presumed PDF approach, this is a requirement. Violating the requirement, the validity of a presumed PDF approach has not been clarified.

Flame Surface Density Model

Flame surface density approaches assumes that the chemical time scale is small compared to the Kolmogorov time scale. This can be interpreted as a very thin layer which can only be wrinkled by the smallest turbulence scales and is not disturbed by thickening. Herein, the flame itself is a convolution of single, laminar flamelets [55]. These flamelets are computed by a counter flow flame using a chemical mechanism of choice. The resulting flame speed is transferred to a table. This table stores the entire flame speeds needed for the simulation. The source term $\widehat{\dot{\omega}}_C$ in equation 3.22 can be interpreted as volumetric source term. It is computed by a consumption speed averaged along the surface $\langle s_c \rangle$, the surface density $\sum$ and the unburned gas density ρ_0:

$$\widehat{\dot{\omega}_c} = \rho_0 \, \langle s_c \rangle \sum . \tag{3.27}$$

The consumption speed is taken from a flamelet library whereas the surface density, describing the wrinkling of the flame surface, is derived by algebraic expressions from turbulence intensity or can be computed by a balance equation [58].

The level set model is closely related to the flamelet approach. Again, the flamelet assumptions must be fulfilled. The flame surface is not defined by a progress variable but by an artificial variable G. G is transported by a conservation equation [57],

$$\frac{\partial \widehat{\rho}\widetilde{G}}{\partial t} + \frac{\partial \widehat{\rho}\widetilde{u}\widetilde{G}}{\partial x_i} = \rho_0 \widehat{s}_t |\nabla \widehat{G}|, \tag{3.28}$$

where s_t is the turbulent flame speed. The turbulence-flame interaction is taken into account by the statistical distribution of G due to turbulence which is then applied to the species distribution.

If the flamelet assumption is fulfilled, the flame surface density approach allows sufficient modeling of the filtered reaction source term and provides reasonable results [43]. However, as the combustion regime of interest is not fully covered by the flamelet assumption, this model has been discarded.

Eddy Breakup Model

In the turbulent mixing length models, the chemistry is supposed to be infinitely fast. So the combustion process is only controlled by the mixing process where enthalpy is transported from the combustion products to the reactants [58]. In premixed flames, mixing controlled combustion is valid only for very high turbulent Damköhler numbers. Furthermore, the flame is considered as a composition of eddies filled either with burned or unburned gas pockets. Then, the chemical reaction rate can be computed from the turbulent mixing time τ_{EBU} and the fluctuations of the progress variable C'' [66], also known as Eddy Breakup Model.

$$\widehat{\dot{\omega}_c} = C_{EBU} \widehat{\rho} \sqrt{\frac{\widetilde{C''}}{\tau_{EBU}}} \tag{3.29}$$

The model constant C_{EBU} has an order of one. Caused by the fast chemistry, the flame is infinitely thin. The resulting fluctuations of the progress variable C'' can be modeled from only two values, 1 and 0. The value of 1 represents the product side of the flame and 0 the unburned side of the flame:

$$\widetilde{C''} = \widetilde{C}\left(1 - \widetilde{C}\right). \tag{3.30}$$

The turbulent time scale τ_{EBU} is derived from the integral time scale, computed from turbulent kinetic energy k and its dissipation rate ϵ:

$$\tau_{EBU} = \frac{k}{\epsilon}. \tag{3.31}$$

In the LES context, the turbulent time scale is interpreted as a sub grid turbulence time scale $\tau_{EBU,SGS}$, thus τ_{EBU} can be replaced by $\tau_{EBU,SGS}$:

$$\tau_{EBU,SGS} \approx \frac{l_\Delta}{u'_{SGS}} \approx \frac{\Delta}{\sqrt{k_{SGS}}}. \tag{3.32}$$

A sub grid time scale, similar to the previous integral length scale, is defined by the sub grid turbulence length scale, because combustion takes place on the sub grid scale. The sub grid turbulence length scale is proportional to the cell or filter size and a sub grid turbulent fluctuation velocity u'_{SGS}. This velocity is proportional to the square root of the sub grid turbulent energy. Both, filter size and sub grid turbulent energy are directly available in LES simulations. The chemical reaction rate can be rewritten to:

$$\widehat{\omega}_C = C_{EBU} \widehat{\rho} \frac{1}{\tau_{EBU,SGS}} \widetilde{C} \left(1 - \widetilde{C}\right). \tag{3.33}$$

In LES the model constant C_{EBU} is very sensitive to Re number and mesh size and must be separately defined for each single case [58]. Furthermore, in the combustion regime of the presented configuration, the requirement of a mixing controlled combustion where $Da >> 1$, is not fulfilled.

The last group of combustion models are finite rate models. The simplest finite rate model is a pure Arrhenius approach used for calculating the filtered source term. In a pure Arrhenius approach, the sub grid scale contributions to the reaction source term are neglected [69].

$$\widehat{\omega}_{fuel} = A e^{E_A/(R\widehat{T})} \left[\widehat{Y}_{fuel}\right]^{\nu_{fuel}} \left[\widehat{Y_{oxidator}}\right]^{\nu_{oxidator}} \tag{3.34}$$

In contrast to the time scale of the turbulent mixing length model, the turbulent time scale is much smaller than the chemical time scale. Therefore, the simple Arrhenius approach can only be used for small Da. The exact reaction mechanism depends on the transported number of species. Generally, a reduced reaction mechanism is preferred because of lower computational costs. The computational mesh must be able to resolve the flame such that the model can be applied for CFD. Reasonable results can be achieved for reactive flows in boundary layers, where the mesh resolution is fine enough to resolve the fluid wall interaction. Because the micro mixing due to the turbulence is not correctly captured, this approach is not sufficient for combustion simulations of technical interest.

Partially Stirred Reactor Model

A mixing factor for turbulence chemistry interaction is introduced to extend the pure Arrhenius approach to a turbulent combustion model, the partially stirred reactor (PaSR) model. The basic idea of this model is separating each control volume into a volume fraction of fine structures ($*$) and a volume fraction of large structures (0) [25]. In the zone with fine structures micro mixing and reaction takes place. In the large structure zones no reaction occurs, because micro mixing is not completed yet. The reaction progress $\dot{\omega}_i$ can then be written as

$$\tilde{\rho}\left(Y_i^* - Y_i^0\right)/\tau^* = \dot{\omega}_i(\tilde{\rho}, Y_i^*, T^*). \tag{3.35}$$

Similarly, the heat release rate on the sub grid scale is

$$\tilde{\rho}\sum_{i=1}^{N}\left(Y_i^* h_i^* - Y_i^0 h_i^0\right)/\tau^* = \sum_{i=1}^{N} h_{i,f}^0 \dot{\omega}_i(\tilde{\rho}, Y_i^*, T^*). \tag{3.36}$$

The variable τ^* describes the sub grid mixing time. With κ^* being the reacting volume fraction, the filtered resolved species mass fraction can be composed from reacting and non reacting structures:

$$\widehat{Y_i} = \kappa^* Y_i^* + (1-\kappa^*) Y_i^0. \tag{3.37}$$

In the same manner the filtered temperature is composed: $\widehat{T} = \kappa^* T^* + (1-\kappa^*) T^0$. Using the reacting volume fraction κ^* within the balance equation for the reacting mass fraction of species i gives

$$\tilde{\rho}(Y_i^* - \widehat{Y_i}) = (1-\kappa^*)\tau^* \dot{\omega}_i(\tilde{\rho}, Y_i^*, T^*). \tag{3.38}$$

Similarly, κ^* is used for the overall energy

$$\tilde{\rho}\sum_{i=1}^{N}\left(Y_i^* h_i^*(T^*) - \widehat{Y_i^0}\widehat{h_i^0}(\widehat{T})\right) = (1-\kappa^*)\tau^* \sum_{i=1}^{N} h_{i,f}^0 \dot{\omega}_i(\tilde{\rho}, Y_i^*, T^*). \tag{3.39}$$

The equation system is closed since the sub grid time scale τ^* and the reacting volume fraction are known variables [2]. The sub grid time scale τ^* must represent all time scales of the unresolved flow. Thus, τ^* is formed of a geometrical mean of shear time scale $\tau_\Delta = \Delta/u'$ and the Kolmogorov time scale $\tau_k = \frac{\Delta}{u'}$,

$$\tau^* = \sqrt{\tau_\Delta \tau_k} \approx \nu^{1/4} \Delta^{3/4} u'^{-5/4}. \tag{3.40}$$

The reacting volume fraction κ^* within one cell can be derived from the volume fractions for small scales to the total cell. The combustion process is assumed to be sequential and works in two steps, a mixing step and the reaction step. Each fluid element must pass both steps. When considering a fixed cell volume ΔV, a fluid element needs the mixing time τ^* plus the chemical time τ_c to pass the cell. Vice versa the volume ΔV can be rewritten as $\Delta V = (\tau^* + \tau_c)\dot{m}/\widetilde{\rho}$. The reacting volume fraction ΔV^* can be defined similarly, $\Delta V^* = \tau_c \dot{m}/\widetilde{\rho}$, and thus, the reacting volume fraction is represented in time scale of $\kappa^* = \frac{\tau_c}{\tau^* + \tau_c}$. The chemical time τ_c is approximated by $\tau_c \approx \frac{\nu}{s_l^2}$. Using these assumptions, the filtered reaction rate can be computed. The filtered balance equation for the species, using the PaSR model, can be written as

$$\begin{aligned} \frac{\partial \widehat{\rho} \widetilde{Y_k}}{\partial t} + \frac{\partial \widehat{\rho} \widetilde{u}_i \widetilde{Y_k}}{\partial x_i} = -\frac{\partial}{\partial x_i} \left[\widehat{\overline{V_{k,i} Y_k}} + \widehat{\rho} \left(\widetilde{u_i Y_k} - \widetilde{u}_i \widetilde{Y_k} \right) \right] + \\ M_k P_{kj} [\kappa^* \dot{\omega}_k(\widehat{\rho}, Y_k^*, T^*) + (1 - \kappa^*) \dot{\omega}_k(\widehat{\rho}, Y_k^0, T^0)]. \end{aligned} \tag{3.41}$$

In general, the last term $\dot{\omega}_k(\widehat{\rho}, Y_k^0, T^0)$ can be neglected. It depends exponentially on T and is much smaller than $\dot{\omega}_k(\widehat{\rho}, Y_k^*, T^*)$ [10].

The PaSR model is selected because of its simplicity and its ability to use an Arrhenius expression for finite reaction rate. Theoretically, chemical and mixing time scales are not initially fixed and thus it is not linked to a certain Da number range.

Thickened Flame Model

The thickened flame model also belongs to the group of finite rate chemistry models. The idea is to thicken the flame artificially to be able to resolve the flame profile on the resolved scales. The laminar flame speed s_l^0 is proportional to the diffusion coefficient D and the reaction rate $\dot{\omega}$, $s_l^0 \approx \sqrt{D\dot{\omega}}$.

At the same time, the flame thickness δ_l^0 depends on the diffusion coefficient and the flame speed, $\delta_l^0 \approx D/s_l$. It has been shown by O'Rourke and Bracco [54], that the flame thickness can be scaled without changing the flame speed if the diffusion coefficient is multiplied whereas the reaction rate is divided at the same time by the same value F. The superscript "1" represents the thickened flame values.

$$s_l^1 \approx \sqrt{DF\frac{\dot{\omega}}{F}} = \sqrt{D\dot{\omega}} \text{ or } s_l^1 = s_l^0 \tag{3.42}$$

$$\delta_l^1 \approx D * F/s_l^0 \approx F\sqrt{\frac{D}{\dot{\omega}}} \text{ or } \delta_l^1 = F\delta_l^0 \tag{3.43}$$

A problem arises in the preheating zone of the flame when the diffusion coefficient is directly multiplied by the thickening factor. If the molecular diffusion coefficients are modified, the mixing of species changes, too. But, laminar flame speed is expected to be very sensitive to species composition and mixing state. To avoid an influence on the diffusion coefficients outside of the flame, the thickening factor is only unequal to one directly within the reaction zone. Next to the reaction zone, the thickening factor is decreased according to an approach by Legier at al. [46]: A flame sensor Ω is introduced, which is used to keep the thickening factor between one and the manually fixed maximum value F_{max}. The sensor Ω can be derived from an Arrhenius like expression for a one step reaction scheme and the activation energy is reduced by $\Gamma < 1$, here $\Gamma \approx 0.5$.

$$\Omega = Y_{fuel}^{\nu_{fuel}} Y_{ox}^{\nu_{ox}} e^{-\Gamma \frac{T_a}{T}} \tag{3.44}$$

Finally the thickening factor F is afterwards calculated according to

$$F = 1 + (F_{max} - 1) tanh\left(\beta\frac{\Omega}{\Omega_{max}}\right) \tag{3.45}$$

The maximum value Ω_{max} can be calculated directly from equation 3.44 by inserting values for stoichiometric conditions. The model constant β describes the transition between thickened and non thickened reaction zone and smoothes the regime of F avoiding steep gradients in the computational field. In this thesis, β is set to 2.5.

Under ideal conditions flame turbulence interaction can be resolved with this approach. However, not the same turbulent scales as in reality wrinkle the flame. Larger turbulent eddies increase the flame stretch if the flame is thicker and turbulent eddies which would have increased the flame surface through flame wrinkling may now increase the flame stretch. Turbulent structures usually increasing the flame speed act now in a negative way and decrease the flame speed. When the chemical time scale $\tau_c = \delta_l^1/s_l^1$ is increased by the thickening factor F, also other characteristics of the flame are altered. The Da number is decreased by the thickening factor F, which results in a lower turbulence sensitivity of the flame. The underestimated turbulence flame interaction is compensated by introducing an efficiency factor E.

The efficiency factor in the thickened flame model can be calculated by comparing the wrinkling Ξ of the real flame front with the wrinkling of the thickened flame front [12]. The wrinkling Ξ in Collin et al. [12] is calculated based on Meneveau and Poinsot [50]:

$$\Xi = 1 + \alpha\Gamma\left(\frac{\Delta_e}{\delta_l}, \frac{u'_{\Delta_e}}{s_l^0}\right)\frac{u'_{\Delta_e}}{s_l^0}. \tag{3.46}$$

The model constant α is defined by

$$\alpha = \beta\frac{2ln(2)}{3c_{ms}(Re^{0.5} - 1)}, \tag{3.47}$$

where $\beta \approx 1$ and $c_{ms} = 0.28$. α is estimated by 0.01 in the presented calculations. The function Γ is given by

$$\Gamma\left(\frac{\Delta_e}{\delta_l}, \frac{u'_{\Delta_e}}{s_l^0}\right) = 0.75\ exp\left[-\frac{1.2}{(u'_{\Delta_e}/s_l^0)^{0.3}}\right]\left(\frac{\Delta_e}{\delta_l^1}\right)^{2/3}. \tag{3.48}$$

In equation 3.46, the second term on the right describes the increase of wrinkling through turbulent stretch based on the turbulent velocity fluctuation. A test filter scale Δ_e is introduced to estimate the efficiency function.

$$\Delta_e = \delta_{sl}^1 = F\delta_{sl}^0 > \Delta \tag{3.49}$$

Δ_e is used in order to calculate the efficiency function. The test filter width has to be chosen carefully such that the test filter width is comparable to the thickened flame width and always larger than the applied filter width Δ. The idea is to calculate the flame wrinkling by the LES filter width and by the thickened flame width, represented by Δ_e. The variable E compares both wrinkling values assuming similarity.

$$E = \frac{\Xi_{\delta_l=\delta_l^0}}{\Xi_{\delta_l=\delta_l^1}} > 1 \tag{3.50}$$

The species conservation equation is combined with the thickened flame model using the thickening factor F and the efficiency factor E. This results in the following conservation equation.

$$\frac{\partial \hat{\rho}\widetilde{Y}_k}{\partial t} + \frac{\partial \hat{\rho}\widetilde{u}_i\widetilde{Y}_k}{\partial x_i} = -\frac{\partial}{\partial x_i}\left[FE\widehat{V_{k,i}Y_k} + \hat{\rho}\left(\widetilde{u_iY_k} - \widetilde{u}_i\widetilde{Y}_k\right)\right] + \frac{E}{F}\dot{\omega}_k(\hat{\rho}, \widetilde{Y}_k, \widetilde{T}) \tag{3.51}$$

3.5 Modeling of Nitrogen Oxides Formation

The $\mathrm{NO_x}$ models used in literature can be separated into a group where the $\mathrm{NO_x}$ calculation is part of the simulation and in a group where the $\mathrm{NO_x}$ calculation is performed after the simulation is finished. It is common that *in situ* approaches can provide more detailed information compared to the post processing methods. The differences are the input values, where post processing methods have only access to the mean and the variance of variables. The specific constellation at one time is not available. Vice versa, usually the post processing running time is much smaller than the in situ approach as it must be executed only once and not at every time step.

The effort for predicting $\mathrm{NO_x}$ emissions depends on the selected combustion model. The source term is already available, if detailed chemistry is involved and the reaction mechanism already takes $\mathrm{NO_x}$ into account. The $\mathrm{NO_x}$ source term must be computed separately if a reduced chemical approach or a empirical flame speed equation is used.

In section 2.3.4, different pathways for $\mathrm{NO_x}$ and their importance together with the progress variable are listed. In figure 3.1 the relevance of these pathways for the total $\mathrm{NO_x}$ production is shown, based on a flat flame under atmospheric pressure with an unburnt gas temperature of 636 K and an equivalence ration of 0.66. The heat loss of the burner plate causes a decrease of the flame temperature from adiabatic 2036 K to 2005 K. It is difficult to calculate the NO_x production of the different pathways directly. Thus, the N_2 consumption for NO_x production for the different reactions is integrated in time. It can be observed, that the NNH and N_2O pathways are the important paths in this regime, forming 70 % of the total NO_x. The contribution of the Zeldovich path in figure 3.1 and figure 3.2 rises with time, but at a decreasing rate. The corresponding source term for NO_x decreases with time, but the combustion is completed and the progress variable is constantly 1. A change of the NO_x source term can not be taken into account at progress variable of 1. This is an important fact, because in a classical combustion model approach based on a progress variable it is therefore hard to capture the thermal NO_x correctly. The mismatch of NO_x source term and progress variable gets even worse when the pressure rises. This can be concluded from the contribution of the Zeldovich pathway in figure 3.2, showing the results from the same flat flame as figure 3.1 but at 20 bar.

Concerning the other NO_x pathways it can be concluded from figures 3.1 and 3.2 that they contribute significantly only during the combustion process within the flame. The source terms from the NNH-mechanisms, the N_2O-mechanism and the Fenimore mechanism can be neglected when all fuel is consumed. This observation leads to a separation into two zones: The flame zone, where the fuel consumption takes place and a post flame zone, where all fuel is already oxidized, but NO_x is still formed.

The presented NO_x prediction model is based on the idea of separating a flame in a flame zone and a post flame zone. To separate between these two regions, a progress variable of 0.99 is identified. Additionally, it is assumed that the very small total amount of generated NO_x does not alter the combustion processes. The total mass fraction of NO_x is several magnitudes smaller than the mass fractions of the species involved in reduced chemistry. Thus the process of NO_x formation has no influence on the combustion process. This results in a sequential procedure where the NO_x calculation is coupled to combustion, but the combustion process is not coupled to the

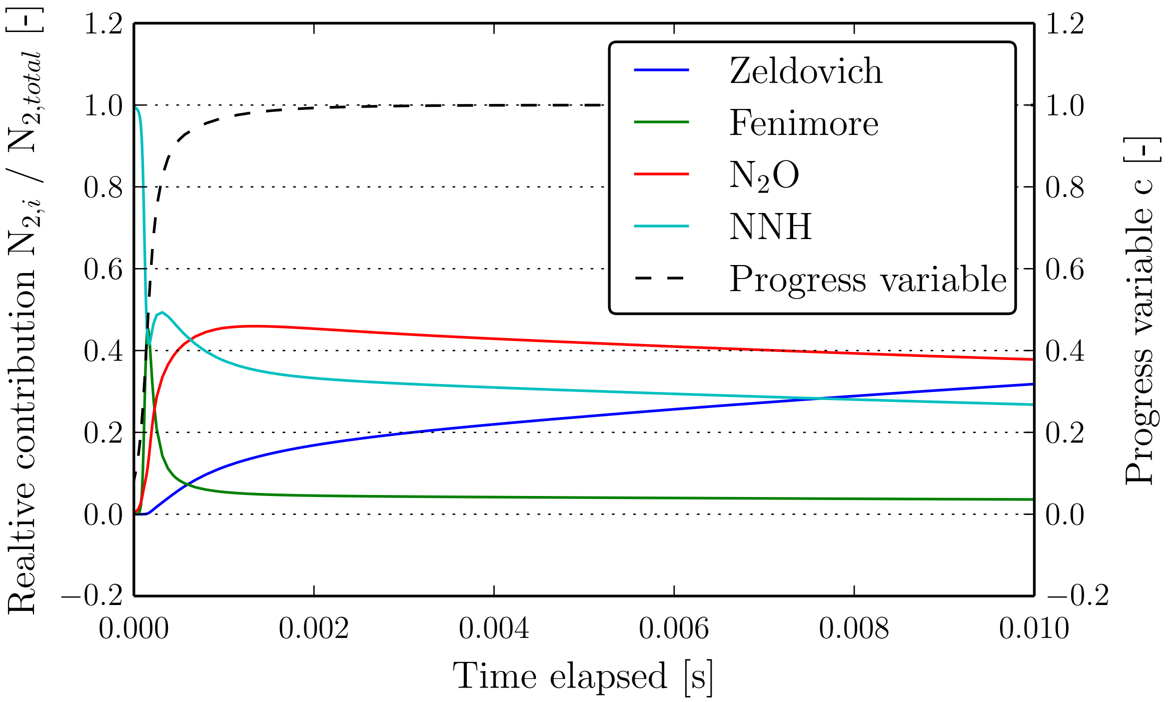

Figure 3.1: Overview of the contribution of the four NO_x pathways depending on the total NO_x production for a methane flame at $\Phi = 0.66$, a fresh gas temperature of 636 K and a pressure of 1 bar. The second y-axis shows the progress variable. The time is set to zero at a temperature of 1000 K.

NO_x calculation.

The information from the combustion process is transferred by two variables, the mixture fraction Z and the progress variable C. In reduced chemistry, these variables are not used. Therefore, these values must be generated by additional transport equations like equation 3.22 and 3.24. From Z and C the reaction source term $\widehat{\omega}_{NO}$ for the NO transport equation

$$\frac{\partial \widehat{\rho} \widetilde{Y}_{NO}}{\partial t} + \frac{\partial \widehat{\rho} \widetilde{u}_i \widetilde{Y}_{NO}}{\partial x_i} = \frac{\partial}{\partial x_i} \left[\widehat{\rho} \left(\frac{\mu}{Sc} + \frac{\mu_{sgs}}{Sc_t} \right) \frac{\widetilde{Y}_{NO}}{\partial x_i} \right] + \widehat{\omega}_{NO} \tag{3.52}$$

is computed, depending on the zone. In the combustion zone a tabulated approach is used whereas in the post flame zone a partial equilibrium approach is taken into account.

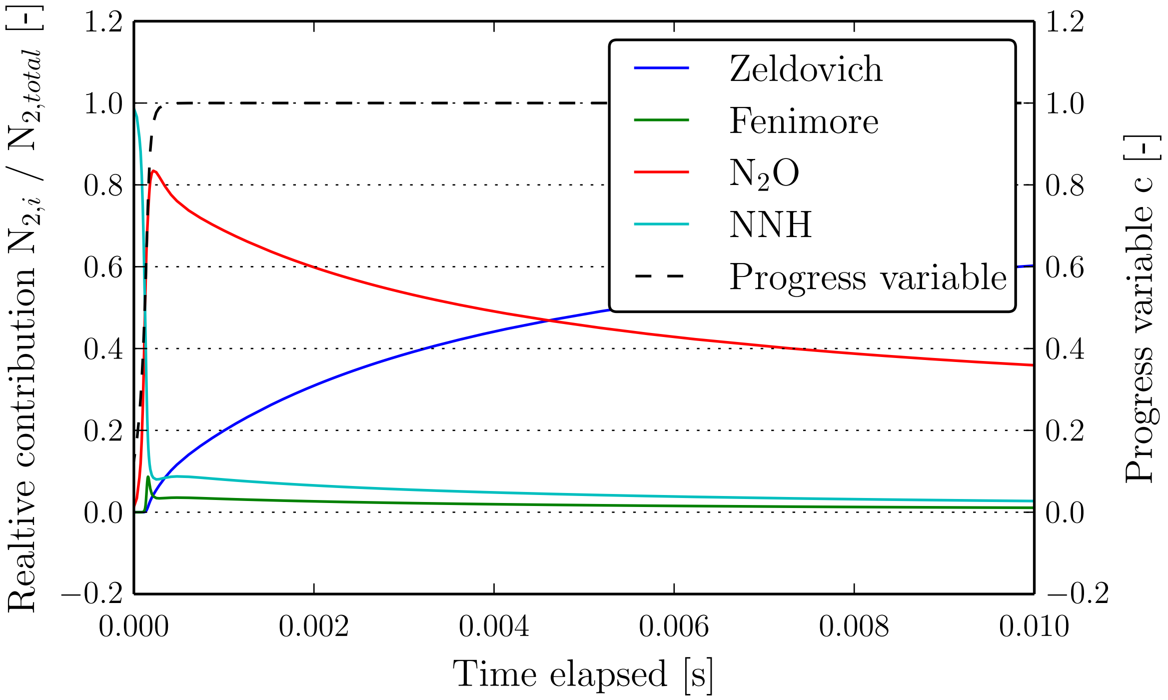

Figure 3.2: Overview of the contribution of the four NO_x pathways depending on the total NO_x production for a methane flame at $\Phi = 0.66$, a fresh gas temperature of 636 K and a pressure of 20 bar. The second y-axis shows the progress variable. The time is set to zero at a temperature of 1000 K.

3.5.1 Tabulated Chemistry

The tabulation is done within the two dimensional space of mixture fraction and progress variable. Therefore, a constant mass, constant pressure reactor (see 2.3.2) is used to generate the table values. The reactor composition is computed from the mixture fraction variable. The content of the reactor moves towards the equilibrium state as a function of time. The time of ignition of a reactor simulation is calculated using a temperature rise of one percent of the total temperature rise to the adiabatic flame temperature. From the reactor calculations the source terms for the species NO and NO_2 are extracted together with the related progress variable. Afterwards, the different source terms for NO and NO_2 are summed up. Together with the related progress variable, they are stored in a table. The progress variable is defined by the concentration of CO_2.

3.5.2 Partial Equilibrium

In the partial equilibrium approach fast reactions are separated from slow reactions. Usually, fast reactions are chain-propagating mechanisms [67] which are closely related to the fuel consumption process, slow reactions are third body reactions. The NO source term in the post flame zone is formed by thermal NO_x, described by the reaction mechanisms 2.35 to 2.37 of Zeldovich,

$$\frac{d[NO]}{dt} = 2k_{f,2.35}[O][N_2]\frac{\left(1-\frac{k_{r,2.35}k_{r,2.36}[NO]^2}{k_{f,2.35}[N_2]k_{f,2.36}[O_2]}\right)}{\left(1+\frac{k_{r,2.35}[NO]}{k_{f,2.36}[O_2]+k_{f,2.37}[OH]}\right)}, \tag{3.53}$$

where the index numbers point to the corresponding Zeldovich reactions. Herein, the concentration of radicals OH and O of a reduced chemistry are mostly unknown. Assuming a partial equilibrium, the concentration of O is calculated by the reaction [44]

$$O_2 + M \leftrightarrow O + O + M \tag{3.54}$$

resulting in

$$[O] = 36.64T^{0.5}[O_2]^{0.5}e^{-27123/T} \tag{3.55}$$

The radical concentration of OH can be estimated analogous to equation 3.55, still assuming the partial equilibrium approach:

$$[OH] = 212.9T^{-0.57}[O]^{0.5}[H_20]^{0.5}e^{-4595/T}. \tag{3.56}$$

The reaction coefficients of equation 3.53 are often taken from Hanson and Salimian [29]. The authors compare NO concentrations derived from their rate coefficients to several experiments concerning thermal NO. But the NO reaction rates of Hanson and Salimian differ by 30 % from the values of the GRI3.0 mechanism [65]. Consequently, computations using the accepted reaction rates [29] would miss the reference values generated with the full chemistry of GRI3.0. Therefore, the reaction rate coefficients are computed using the values from the GRI3.0 mechanism.

$$k_{f,2.35} = 2.70E07 \exp(-178.6/T) \qquad [m^3/(kmols)] \tag{3.57}$$
$$k_{f,2.36} = 9.00E03T \exp(-3270.9/T) \qquad [m^3/(kmols)] \tag{3.58}$$
$$k_{f,2.37} = 3.36E07 \exp(-193.7/T) \qquad [m^3/(kmols)] \tag{3.59}$$

The corresponding reaction rates of the opposite direction are not explicitly given in Smith et al. [65]. The backward reaction rate is computed by the relation between the Gibbs free energy ΔG and the equilibrium constant k_{eq}. The Gibbs free energy is the difference of chemical potential between the reactants and the products.

$$\Delta G = -RTlnk_{eq} \tag{3.60}$$

A criterion for using tabulated chemistry or the partial equilibrium approach, respectively, must be found in order to apply the suitable model to the combustion zone. The progress variable, shown in figures 3.1 and 3.2, is well suited for this purpose, because it is already available and sensitive to the combustion zones. The combination of both models is necessary because under atmospheric conditions the Fenimore-, the NNH- and the N_2O-mechanism are predominant. The developed model must provide this ability to allow a validation against experimental data. Under pressurized conditions, the contribution of the thermal pathway gets dominant with time, whereas the Fenimore mechanism is negligible.

The presented NO_x model within a CFD simulation can be applied during the simulation (*in situ*) based on instantaneous values or in a post processing step by using only mean values of species, temperature, progress variable and mixture fraction. The advantage of an *in-situ* application is a more realistic result of NO_x emissions. The source term for equation 3.52 in an *in situ* application is taken from the table or it is calculated from equation 3.53 based on filtered variables. Fluctuations of e.g. the temperature on the large scale are taken into account. Subgrid fluctuations, which are not calculated but modeled, influence the filtered variable in their conservation equation only by the subgrid term. In a post processing application of the new NO_x model only mean values are taken into account.

3.5.3 Validation

The functionality of the NO_x model is demonstrated by computing a laminar burner stabilized flame using OpenFOAM on a one dimensional grid with 500 cells. The reference flame is computed using the detailed chemistry from GRI3.0 [65]. In the second case, one step chemistry [70] is combined with the new NO_x model. The equivalence ratio is set to 0.66 at a gas temperature of 800 K under atmospheric pressure. The inlet velocity is optimized to a minimal heat loss of the burner plate to restrict lift-off and avoid blow-out of the flame.

In figure 3.3, the results of reference flame and new model are displayed in terms of total NO_x concentrations and temperatures. In the reference case, NO, NO_2 and N_2O are summed up to total NO_x concentration. Basically, both flames agree quite well. The final values for temperature and NO_x are almost identical and predict the corresponding measurement values from an experiment. Deviations are found within the flame. The temperature rise occurs faster when using one step chemistry than detailed chemistry because the one step chemistry does not consider intermediate products. However, using detailed chemistry intermediate species starting the chain reactions are taken into account. Consequently the reaction zone of one step chemistry is thinner. Neglecting intermediate species also influences the NO_x profile. NO_x emissions grow faster using the new NO_x model than when they are computed from detailed chemistry.

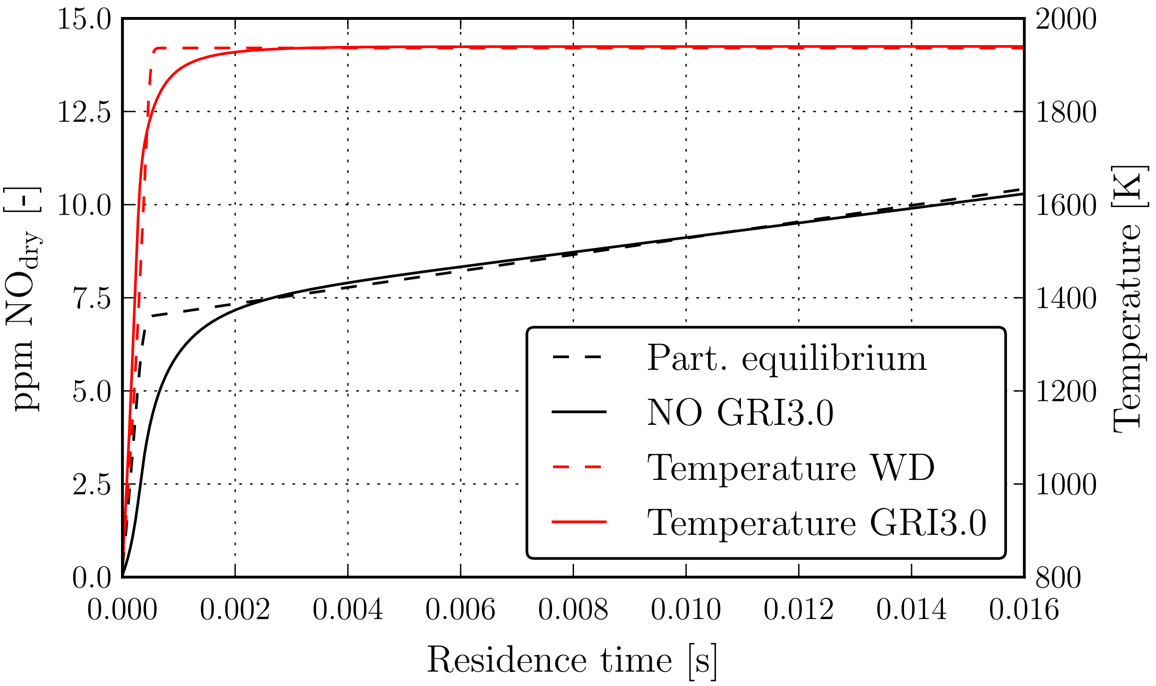

Figure 3.3: Comparison of NO_x production of a flat flame using detailed chemistry or the coupling of tabulation with partial equilibrium.

4 LLI Test Rig

In parallel to the simulation an experiment has been set up by Schmitt et al. [63]. Measurements from this test rig are used to verify the simulated data. Thus, the test rig is described in the following paragraphs.

Although modern heavy duty gas turbines are operated at a pressure of approx. 20 bar, the test rig is built for atmospheric condition because of practical reasons. Scaling of the operation condition of the test rig is necessary to reproduce a comparable combustion process and to compensate for the pressure effects. The scaling is calculated on the ignition delay Damköhler number which is defined as

$$Da_{\tau_{ign}} = \frac{\tau_t}{\tau_{ign}} = \frac{l_t}{u'_{rms}} \frac{1}{\tau_{ign}}, \tag{4.1}$$

where l_t is the integral length scale, u'_{rms} the mean velocity fluctuation and τ_t and τ_{ign} the turbulent and chemical time scale, respectively. It is assumed that the combustion processes are similar if $Da_{\tau_{ign},eng} = Da_{\tau_{ign},exp}$. The ignition delay of methane is assumed to correlate with $\tau_{ign} \propto p^{-1}$ resulting in a scaling factor of $\frac{Da_{\tau_{ign,eng}}}{Da_{\tau_{ign,exp}}} = \frac{\tau_{ign,exp}}{\tau_{ign,eng}} = 20$. To obtain the scaling factor, the experimental velocity is reduced to a factor of $\frac{1}{5}$ while the integral length scale, characterized by the jet diameter, is increased by a factor of 4.

In figure 4.1 the test rig is schematically shown. In the plenum methane and preheated air at 670 K are mixed. In the primary combustion the 16 flames consume the fuel air mixture before the vitiated gas enters the secondary combustion zone at a temperature of 1760 K. In the second combustion zone a pipe is mounted perpendicular to the test rig which generates a premixed methane air jet in the crossflow of vitiated gas. The equivalence ratio of the jet is varied, whereas the equivalence ratio in the plenum is fixed. Like the reactants of the crossflow, the jet is preheated. The jet diameter can be modified using different inserts which reduce the diameter from a maximum of 100 mm to 50 mm or 15 mm. When the jet enters the second

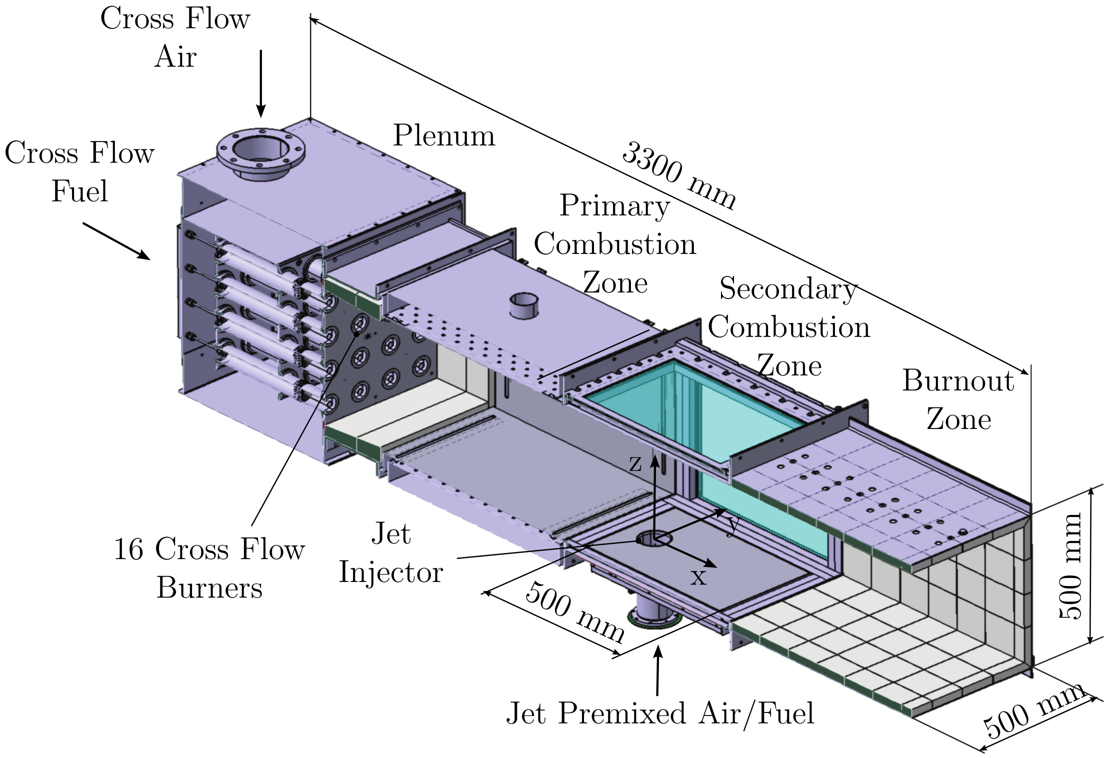

Figure 4.1: Experimental test rig consisting of first combustion stage, first combustion chamber, second combustion chamber with jet inlet and exhaust gas section.

combustion chamber, the jet starts burning and a flame of a complex shape is generated. The last segment is designed for burn out to complete the combustion process and avoid emissions of unburned products.

The coordinate system shown in figure 4.1 is used in the following. The origin of the coordinate system is at the center of the jet orifice at the bottom of the secondary combustion zone. The x-axis is aligned with the direction of the crossflow, whereas the z-axis is orientated in the direction of the jet at its origin. The y-axis completes the orthogonal coordinate system.

All measurements are taken in the second combustion zone. The casing of the second combustion zone is built of glass on three sides to apply optical measurement techniques. The velocity is measured by particle laser induced fluorescence (PLIF) on the symmetry plane along the axial direction. The mixing of jet and crossflow is measured by a thermocouple traversed in a cross section plane perpendicular to the x-axis. The spacing of the measurement grid is 10 mm in both directions, if not mentioned otherwise. Finally NO and NO_2 measurements are performed in a cross section perpendicular to the x-axis. The measurement plane is identical to the cross section which is directly between the second combustion zone and the burn out zone. This plane is located 400 mm downstream of the center of the jet exit. The NO_x measurements provide mean values and no instantaneous data because of technical reasons.

5 Results and Discussions

5.1 Atmospheric Jet in Crossflow Simulations

LES requires a computational grid which is generated depending on the expected turbulence and chemical length scales. Simultaneously, the total cell number is limited by the available computational hardware. An adapted mesh approach is used to fulfill the requirements. The grid includes the second combustion chamber of the test rig and a pipe with a length and a diameter of 100 mm as shown in figure 5.1. The mesh is locally refined where jet material is expected. These regions are found by a previous simulation using RANS on a grid with uniform cells neglecting chemical reaction. Then the predicted location of jet material is enclosed by a bend, conical interface. It starts at the jet entrance and stops at the outlet of the domain at $x/D = 4$. In the following step the LES mesh is generated using ANSYS ICEM CFD. Each cell is hexahedral, resulting in a completely geometrically structured computational mesh. The region where jet material is located is equipped with smaller cells, whereas the rest of the domain is meshed coarser. The symmetry plane at $y/D = 4$ of this Mesh is displayed in figure 5.1.

The resulting mesh is a compromise of resolution and computation time and consists of about 3.2 million cells in total. The quality of the grid can be measured by the M-criteria, the ratio of unresolved turbulent kinetic energy to total kinetic energy. It is higher than 0.2 in the whole domain which is similar to an unresolved turbulence level of 20 % as expected in LES [6]. To compute 10 hydraulic residence times using 256 CPUs (8-way Opteron Dual-Core of 2.6 GHz connected with 10G Myrinet) 8 days are needed for a simulation without chemical reaction and 24 days with flame.

The results for different jet diameters will be presented below. A jet diameter of 100 mm is used for validation by measurements for velocity and temperature. Furthermore, a jet diameter of 50 mm is used to compare the

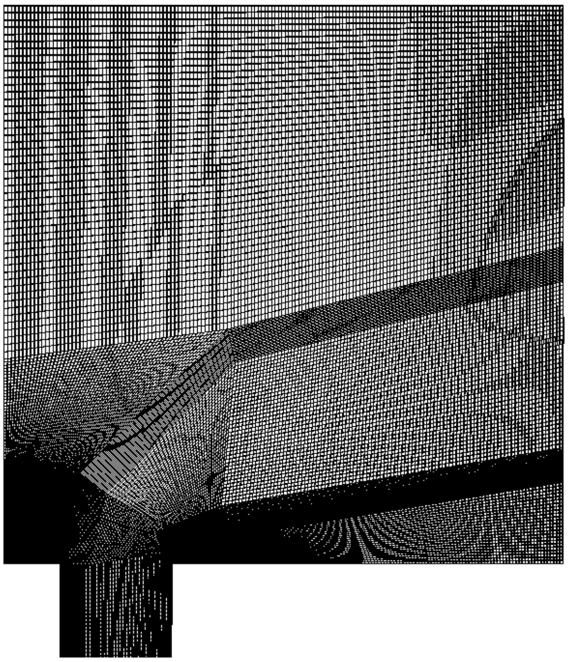

Figure 5.1: Symmetry plane showing the computational grid for a jet diameter of 100 mm.

results to measurements for temperature and emissions. Finally a jet diameter of 25.4 mm is used in the simulation of the pressurized configuration. The different diameters are realized by a diameter restriction in the jet pipe which is also taken into account by the computational mesh.

The presented adapted mesh approach needs a lot of manual interaction why it is time consuming. But different jet diameters, jet geometries and momentum ratios must be realized. Therefore, a faster approach is necessary. The snappyHexMesh utility shipped with OpenFOAM is found to simplify the mesh generation. It starts from a geometrical surface of the simulation domain and meshes it with uniform spaced grid. In several sequential steps, a castellated mesh is generated. The castellated approach uses a geometrical description of the mixing regions of the jet and refines the specified region until the desired resolution is reached. The final grid resolution is comparable to the grid resolution produced by the adapted mesh approach. The result for the 50 mm jet can be seen in figure 5.2. The

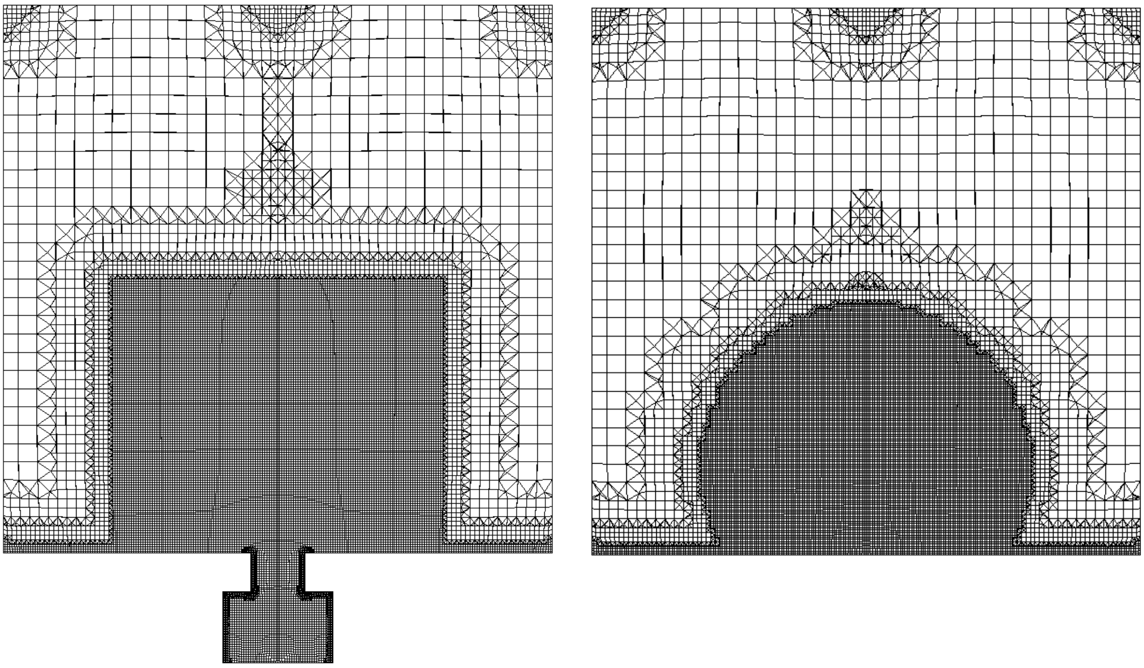

Figure 5.2: Slices perpendicular to the crossflow showing the computational grid for a jet diameter of 50 mm. On the left hand side at $x/D = 0$, on the right hand side at $x/D = 2$.

dimensions of the domain for a jet diameter of 50 mm equals 500 mm in all coordinate directions. The axis of the jet pipe coincides with the z-axis. The jet length is fixed to 100 mm. The castellated meshing procedure is limited in its mesh grading functionality. Generating the same resolution within the finest resolved regions, the castellated mesh results in a higher total cell number than the adapted mesh procedure does. Additionally, the lower turbulent length scale for the smaller jet diameters must be taken into account. The weakness in mesh grading and the smaller turbulent length scales results in a computational grid of about 4.2 million cells.

In LES the turbulence values applied at a inflow boundary condition have a crucial influence on the result. Turbulence within a LES is not represented as a single value but by resolved and unresolved fluctuations in velocity.

The resolved part must also fulfill the energy cascade described earlier (see chapter 2.2). If the energy spectrum is not taken into account and only random values are applied, the fluctuations due to turbulence applied on the inlet dissipates immediately. They do not have any effect on the flow field downstream. To satisfy the requirement of a energy spectrum, a precursor field only for turbulence is computed for every inflow boundary. Based on statistical methods, the velocity fluctuations at the inlet are computed from a random number field. Detailed information about the necessary mathematical steps to compute the velocity fluctuations from random numbers is given in appendix C and in Kempf et al. [39].

Before a LES is started a RANS is conducted in advance to provide starting values. Starting the LES from scratch turned out to be difficult and rarely successful.

5.2 Non-reacting Jet in Crossflow

5.2.1 Velocity Fields

The setup had to be chosen carefully to match the requirements of the experiment of Schmitt et al. [63]. Different authors [62] [22] have already shown that a large eddy simulation can predict the mean velocity of a jet in crossflow with good accuracy. In literature, the importance of correct turbulent inflow conditions is emphasized [58]. Schlüter and Schönfeld [62] did not find a significant influence of the sub grid turbulence model on the velocity fields of jets in crossflow. Taking these informations into account the jet in crossflow is simulated using the turbulence generator described in Appendix C and the dynamic Smagorinsky subgrid turbulence model. The jet in crossflow configuration comprises a jet diameter of 100 mm and a momentum ratio of $J = 6$. Both for crossflow and jet a turbulence intensity of five percent was applied. In the following, this jet in crossflow case is referenced as configuration 1 (see table D in the Appendix). Generally the displayed mean values are computed from simulations of ten hydraulic residence times of the crossflow in the domain. A longer averaging time does not alter the mean values. The simulation results for mean velocity are shown in figure 5.3 on the left. On the right the experimental data from a corresponding configuration are shown. In both the simulation and the experiment plot white streamlines are shown, including arrows indicating the direction. These streamlines are a visualization of the mean velocity and are calculated from the z and y component from the velocity vector. The values in figure 5.3 show the symmetry plane. From figure 5.3 can be concluded, that simulation and experiment agree very well. Both, velocity magnitudes and velocity direction at the jet entrance are predicted correctly. Furthermore, the crossflow of simulation and experiment agree in velocity magnitude but the direction deviates in the region between $z/D = 2$ and $z/D = 3$. The reason is a small leakage in the experimental test rig which caused entrainment of leakage air and modifies slightly the flow field. But this deviation is very small and should not have a significant influence on the interaction of jet and crossflow. The velocity trajectory of the jet is the

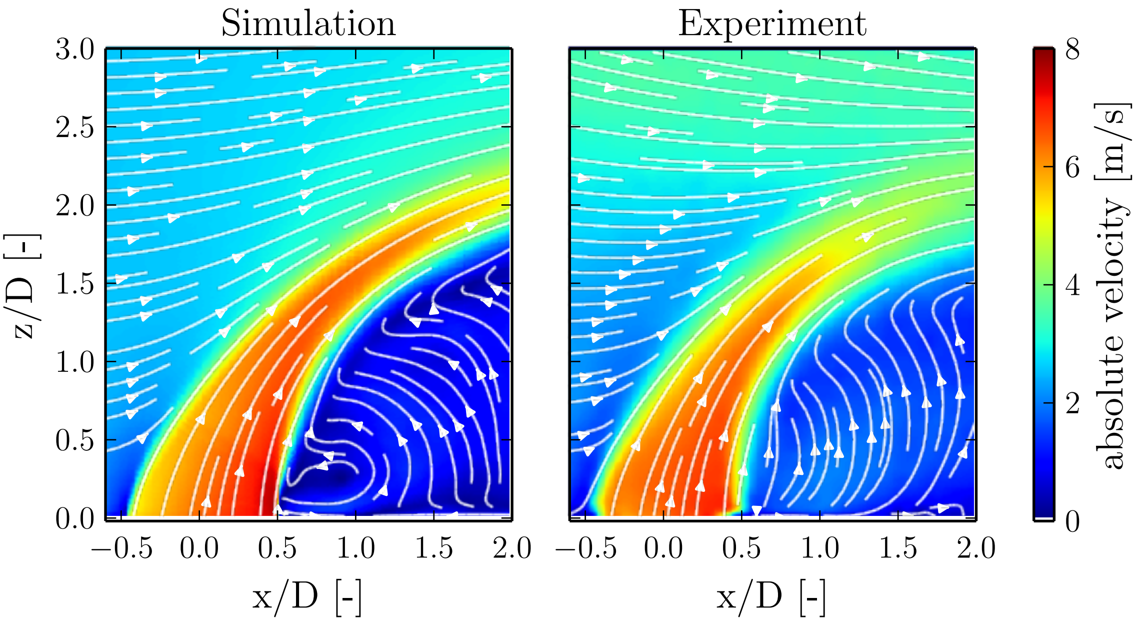

Figure 5.3: Mean velocity magnitude in the symmetry plane $y/D = 0$ of a non reacting JIC at $R = 6$. On the left hand side simulation values, on the right hand side experimental data.

same for LES and experiment.

In order to examine the agreement of experiment and LES in greater depth, a line plot over z/D at different positions in figure 5.3 is plotted in figure 5.4. The results for the simulated mean velocity are displayed as solid lines, the experimental values are displayed by circles. Additionally, the dashed lines show the results of a setup similar to configuration 1, neglecting the turbulence fluctuations at the inflows (configuration 2, see table D in the Appendix). It can be seen that the penetration depth of the jet fits the experiment, but the velocity magnitude is slightly overpredicted.

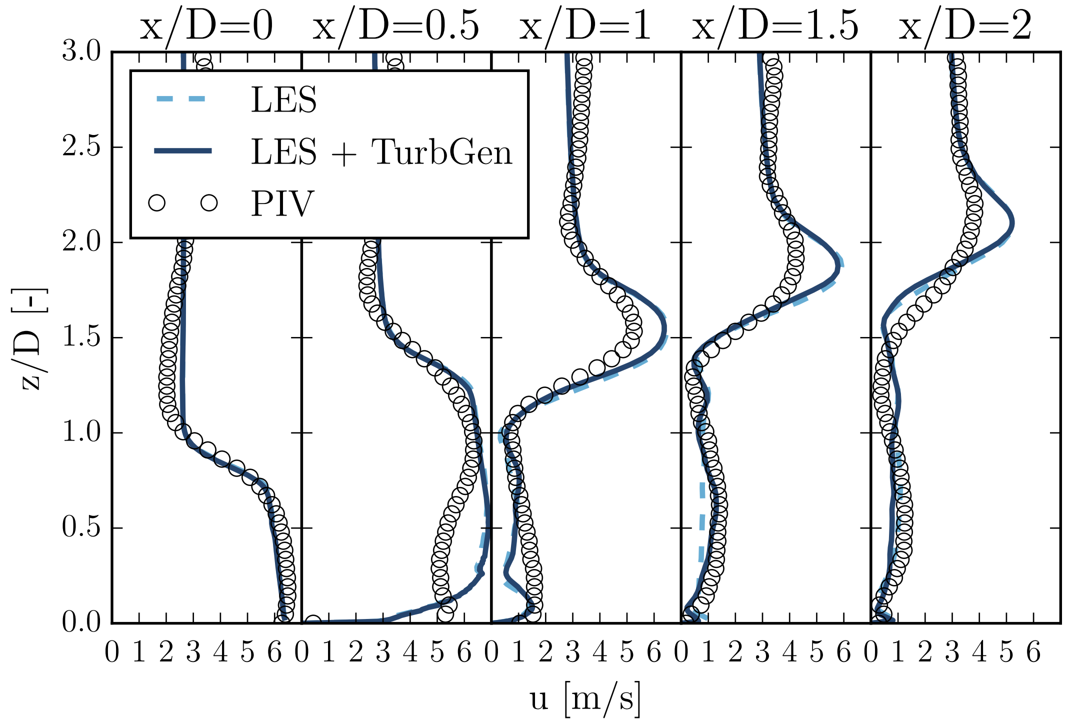

Figure 5.4: Mean velocity magnitude in the symmetry plane $y/D = 0$ at different x/D positions: light blue dashed solid line LES without turbulence generator, dark blue solid line LES including turbulence generator, circles representing experimental values.

Additionally, figure 5.4 reveals almost no difference between the simulation with and without turbulence generator at the inlet. Similar results can be observed from investigations with a fully turbulent pipe flow using different sub grid turbulence models. Computation of fully turbulent flow in a separate pipe and applying the results on the jet inlet did not show a significant difference to the synthetic turbulence generator applied at the inlet. Only minor changes where observed.

To explain these findings, the velocity fluctuations are displayed in figure 5.5 more in detail. Corresponding to figure 5.4 the mean velocity fluctuation calculated from mean fluctuating values in x and z direction are visualized. Again solid lines represent configuration 1, dashed lines configuration 2. The circles are measurement values. Although the absolute values of simulation and experiment differ, the locations of the maximal values agree with each other. Furthermore, the higher turbulent intensity on the lee side of the jet in contrast to the windward side is predicted correctly. The deviations between simulation and experimental can be explained by two reasons: The measured velocity fluctuations in the crossflow reveals a turbulent intensity of 50 %. For an undisturbed channel flow like the crossflow, this turbulence

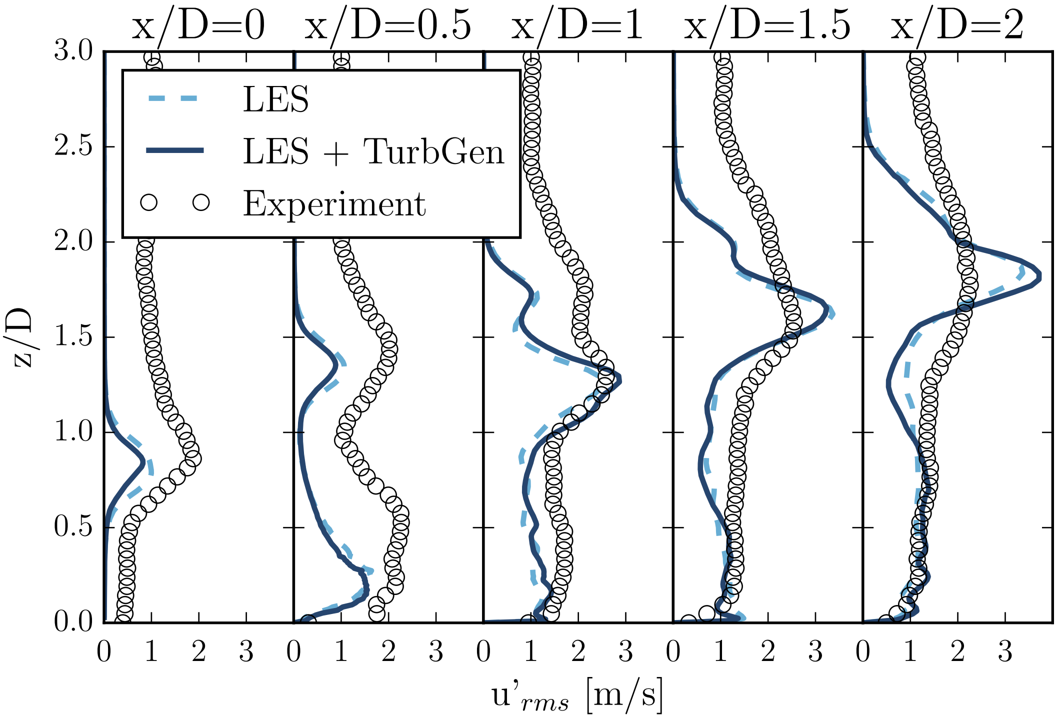

Figure 5.5: Mean velocity fluctuations in the symmetry plane $y/D = 0$ at different x/D positions: light blue dashed line LES without turbulence generator, dark blue solid line LES including turbulence generator, circles representing experimental values.

level is unphysically high. These values are not taken into account. The second reason is a difference in the averaged velocity fluctuations of simulation and experiment. The measured velocity fluctuations have different sources: velocity fluctuations due to turbulence and the velocity fluctuations due to large coherent structures. The experimental values displayed in figure 5.5 are time averaged results of a series of instantaneous experimental values. Therefore, velocity fluctuations due to large coherent structures contribute as well to mean velocity fluctuations as turbulence fluctuations do. In LES for the velocity fluctuations only fluctuations due to turbulence are taken into account. Therefore, experimental velocity fluctuations are expected to be higher than numerical values. This reason is more dominant where coherent structures are present and resolved. Although this is especially true for the locations where the peak values exist, the simulation overestimates the peak values at $x/D = 1.5$ and $x/D = 2$. At the peak location of $x/D = 2$, the mesh is already getting coarser. The influence of the subgrid model on the velocity fluctuation is increasing and does not capture the turbulence fluctuations correctly.

Focusing on the influence of the turbulence generator no dedicated difference between configuration 1 and 2 are found. Whereas the velocity fluctuations in configuration 1 are slightly higher at $x/D = 1$ and $x/D = 2$, they are smaller than in configuration 2 at $x/D = 0$ and $x/D = 1.5$. Further investigations with higher intensities and fully turbulent pipe flows do not show significant differences in the velocity values. It is concluded that for the computation of velocity profiles of a jet in crossflow configuration, a precise modeling of the turbulence structure at the inlet is not required. A similar investigation of the influence of the turbulence level at the boundaries on the species distribution is not possible as no instantaneous experimental data is available. Because an influence on the mixing process can not be excluded, in the following simulations the artificial turbulence generator is used.

5.2.2 Mixing

To evaluate and understand the mixing behavior of jets in crossflow, the quality of the simulation must be checked also for scalar transport. To distinguish between jet and crossflow, the jet in configuration 3 is heated to 393 K whereas the crossflow is at ambient temperature of 293 K. In configuration 3 the heated jet of a diameter of 50 mm is simulated at a momentum ratio of $J = 15$. In figure 5.6 the normalized temperature $\Theta = \frac{T - T_{cf}}{T_{jet} - T_{cf}}$ from the simulation and the corresponding experiment is plotted. At different x/D positions the computed values from LES are compared to measurements. Open circles represent experimental values whereas solid lines symbolize simulation values. The simulation values match the experimental data almost perfectly except at the position $x/D = 0.5$. The explanation for that deviation is not straightforward. In analogy to a round bluff body a low pressure region behind the jet is observed close to the bottom. The lower pressure forces the surrounding crossflow material to enter this region and results in the behavior shown in figure 5.6 at $x/D = 0.5$ and $0 < y/D < 2$.

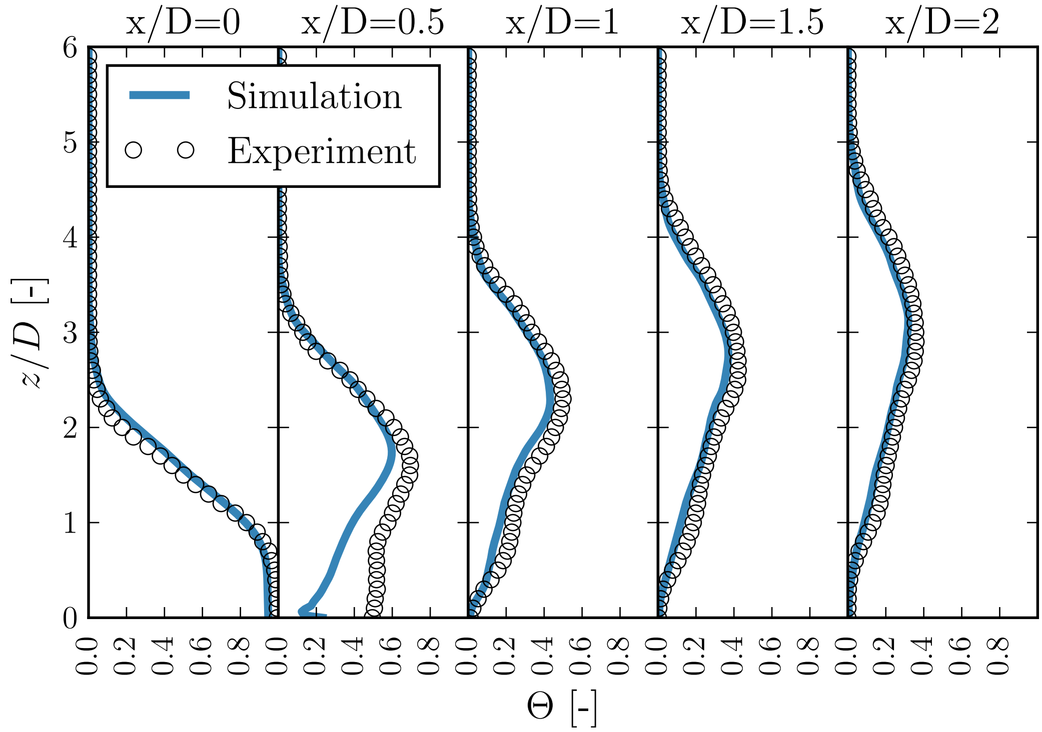

Figure 5.6: Mean normalized temperature in the symmetry plane $y/D = 0$ at different x/D positions for a momentum ratio of 15 and a jet diameter of 50 mm: the solid lines represent simulated values, the circles represents experimental data.

Therefore the simulated values seem feasible. In figure 5.6 the same phenomenon is also present in the experiment but to a lower extent. Unfortunately no velocity measurements are available for configuration 3 to further prove the explanation [21].

The simulation provides reliable data that agree well with experimental results not only for velocity but also for temperature. This allows to use LES to investigate the mixing behavior and mixing quality of jet in crossflow configurations for different jet geometries.

The interaction of jet and crossflow results in a complex interaction of different coherent structures of various size. Furthermore, the choice of jet geometry influences the vortex systems [28] and mixing. Additional turbulence in the jet can even further alter the mixing [18]. To examine the influence of geometry and turbulence on the mixture profile and the mixing speed, different geometries are investigated within the mixing study presented below.

Four different jet geometries are considered. First, a round (plain) jet with a diameter of 100 mm. Second, a swirling jet with the same diameter. The swirl is generated by a twisted tape with a width of 100 mm rotating counterclockwise for 90° around the z-axis within the jet pipe. The tip of the tape is located at a distance of 100 mm upstream of the jet orifice. The last two geometries consist of a slot with a length of 140.6 mm and a width of 56.2 mm. In one configuration the slot is aligned with the crossflow in x direction. In the other configuration the slot is orientated perpendicular to the crossflow. The center of all jet geometries is collocated within the origin of the coordinate system. All four geometries have the same cross section area.

For each geometry a LES is performed at a momentum ratio of $J = 6$. To track the mixing process the jet is heated to 393 K while the crossflow is at 293 K. Beside a higher temperature the jet contains a small mass fraction of argon $Y_{Ar} = 0.01$ used as tracer. These conditions correspond to configuration 4 (see table D in the Appendix).

To judge the mixing quality of the different geometries the spatial mixing deficiency (SMD) also discussed by Cardenas et al. [9] is used. Based on

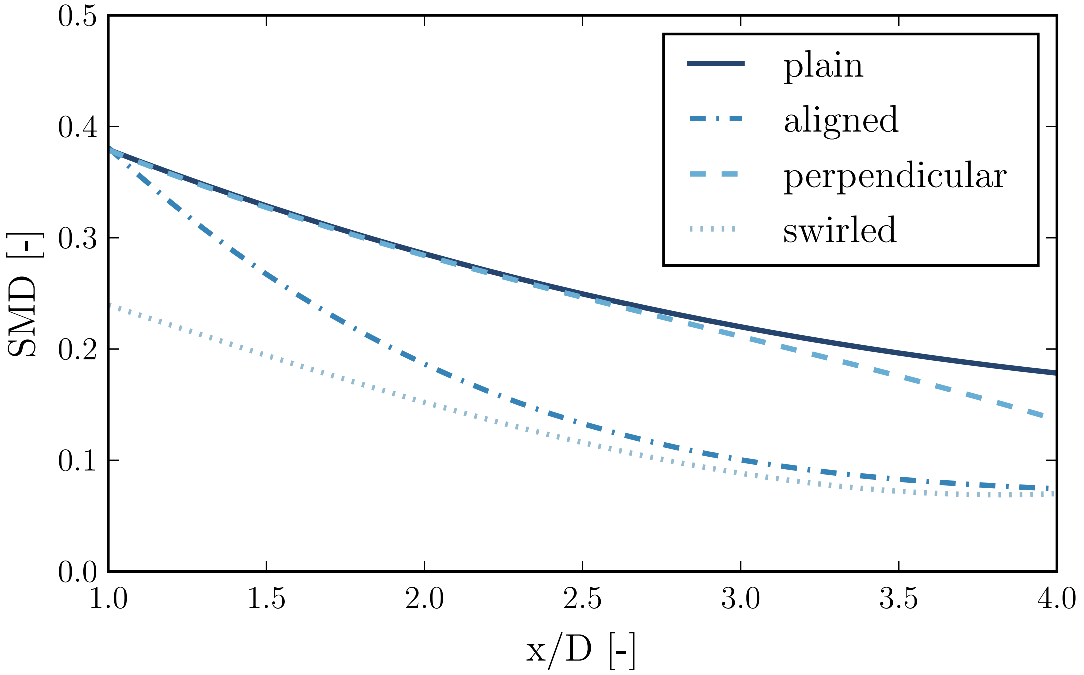

Figure 5.7: Mixing behavior displayed by SMD for different jet geometries.

Boss [5] the SMD value of a cross section is calculated by

$$\mathrm{SMD} = \frac{\mathrm{VAR}(\Phi)}{\mathrm{AVG}(\Phi)} = \frac{\sqrt{\frac{1}{M \cdot N} \sum_i^M \sum_j^N \left[\Phi_{i,j} - \frac{1}{M \cdot N} \sum_i^M \sum_j^N \Phi_{i,j}\right]^2}}{\frac{1}{M \cdot N} \sum_i^M \sum_j^N \Phi_{i,j}} \tag{5.1}$$

where the indexes i and j represent the row and column respectively. Φ is the normalized temperature calculated based on the temperature of the cross flow $T_{crossflow}$ and the temperature of the jet T_{jet} : $\Phi = \frac{T - T_{crossflow}}{T_{jet} - T_{crossflow}}$. The SMD values for the four geometries are calculated from the normalized temperature Θ of a series of cross sections normal to the x-axis and are displayed in figure 5.7. Although the SMD values are all within a comparable range, significant differences can be seen. Very close to the jet exit at $x/D = 1$ the SMD value from the twisted tape is more than 30 % lower than the SMD values from the other geometries. As the swirled jet contains much higher turbulent kinetic energy, this behavior seems feasible and was expected at least in comparison to the plain jet. Following the flow downstream the SMD value of the twisted tape falls continuously but not as fast as the SMD value of the aligned jet. Comparing the aligned and the swirled jet at $x/D = 4$ the aligned jet has almost reached the same mixing quality than the swirled jet. Comparing the swirled and the plain jet, the difference between both remains quite constant in downstream direction. The SMD values decrease with the same slope but keeping their offset value from each other at $x/D = 1$. The perpendicular jet differs only slightly from the plain jet in mixing quality. Starting at the same level of unmixedness, the perpendicular jet improves in terms of mixing quality more rapidly than the plain jet and outperforms the plain jet at the end of the domain significantly. Summing up, the swirled jet provides the best mixing behavior compared to the three other geometries. The plain jet mixes slowest followed by the perpendicular jet which one is only slightly better than the plain one. The aligned jet starts with a level of unmixedness similar to the plain and perpendicular geometries but after 3 diameters the mixing quality is comparable to the swirled jet geometry.

To explain the different mixing behavior the turbulent structures are examined in detail. To visualize the vortices the widely used Q criterion of Hunt et al. [34] is employed. The isosurfaces of the $Q = 3$ criterion of all four configurations are shown in figure 5.8. Additionally, the surfaces are colored by the magnitude of the velocity. To reference the vortex structures and make them locatable within the simulation domain, the exit of the jet into the crossflow is visualized with gray planes. First, the plain jet is considered top left. On the windward side of the jet the coherent structures known as ring vortices or shear layer vortices is clearly visible. These coherent structures are widely discussed in literature [20] [49]. They mix crossflow material with jet material as they rotate within the shear layer between jet and crossflow. From the color of these vortices it can be concluded, that the rotation speed of the vortices is comparably low. On the lee side of the jet an unstructured field of vortices is visible. The color of these regions also indicates lower velocities. The vortices of the plain jet which are directly in contact with the crossflow show velocities up to 3 m/s. Only the vortices directly next to the jet on the lee side show a higher velocity of up to 8 m/s. Nevertheless the mixing enhancement by the lee side vortices is limited. The reason is the low mass flux of crossflow material in this region. This can be seen from

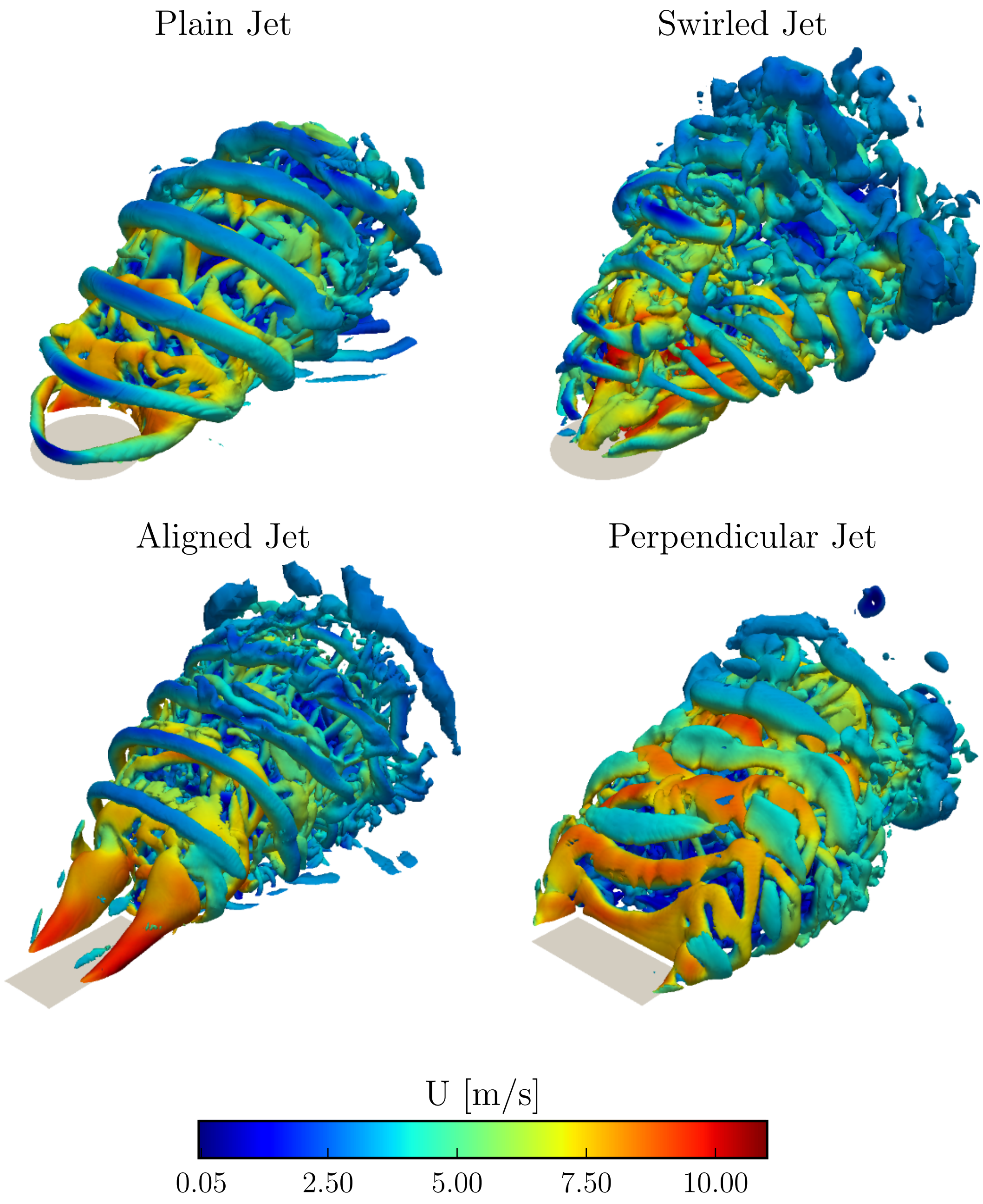

Figure 5.8: Isosurface of Q = 3 symbolizing coherent structures of the different jet geometries. The color represents the instantaneous velocity magnitude on the isosurface.

figure 5.3 where at the lee side velocities close to zero are shown. The jet acts as an obstacle in the flow and hinders the entrainment of crossflow material into the lee side of the jet. Not visible in 5.8 is the counter rotating vortex pair. For the plain jet this vortex system is expected to have a negligible influence on the mixing behavior as it performs only a rotation of 90° within the whole computational domain. Therefore it is not able to entrain significant amounts of crossflow material.

On the upper right the swirled jet geometry is displayed. The twisted tape generating the swirl is not visible as it is located 100 mm upstream of the jet exit. At the jet exit a swirl number of 0.14 is calculated. The vortex structures show two almost separated half jets which are surrounded by separated ring vortices. These eddies are not as clearly shaped as they are in the plane case but show higher velocities on their surfaces. The ring vortices do not combine until the end of the domain. They dissipate already within about three jet diameters. But in comparison with the plain jet the surface area of these shear layer vortices is larger as the vortices of the swirled jet are superior in number. Furthermore, the shear layer area between jet and crossflow is enhanced in comparison with the plain jet. Both the larger shear layer and the higher vortex surface enhance the mixing process. In figure 5.8 vortices within the jet right at the jet exit are shown. These eddies lead to the transport of crossflow material from the shear layer into the core of the jet. In comparison, within the plain jet no coherent structures are present right from the beginning. This can also be interpreted by a significantly higher turbulent intensity of the swirled jet than of the plain jet. Therefore, the transport of crossflow material in the plain jet is missing the convective processes originating from these large scale eddies. The plain and the swirled geometry also differ in penetration depth. The swirled geometry penetrates less. At the shown momentum ratio of $J = 6$ the swirled jet attaches to the bottom whereas the plain jet is clearly separated. The attachment to the bottom is also observed for higher momentum ratio of $J = 10.89$ [18]. In summary, the swirled jet mixes faster than the plain jet. The reasons are enhanced mixing of crossflow material into the shear layer and secondly higher turbulent intensity within the jet resulting in a faster transport of crossflow material in the core of the jet.

On the lower left of figure 5.8 the vortex system of the aligned jet is displayed. The most obvious differences to the other geometries are the two dominant vortices right at the jet exit. They start in the middle of the long side of the rectangular jet and generate the only vortex structure visible until $x/D < 0.5$. The velocity on the vortex structure reaches more than 10 m/s while the vortex interacts both with jet and crossflow material. This results in a high entrainment rate of crossflow material right from the start at $x/D = 0$. These two large vortices start to dissipate at $x/D = 0.5$ while moving downstream and initiate smaller turbulent structures within the jet. Similar turbulent structures within the jet can not be observed in the plain jet. Furthermore, the dissipation of the two large vortices from the beginning indicate the point of origin in x-direction for the shear layer vortices. But they do not persist in their smooth shape like in the plain jet. At about $x/D = 2$, the shear layer starts to dissipate into small eddies with varying orientation. These small eddies are located in the shear layer and have contact to both crossflow and jet material. Therefore, they enhance the mixing of jet and crossflow material. In comparison to the plain jet three factors are responsible for the different mixing quality. Firstly, two strong vortices in the shear layer next to the long edges entrain crossflow material into the jet. Secondly, these two strong vortices serve as source for turbulent fluctuations within the core of the jet in downstream direction. Thirdly, quick dissipation of the shear layer vortices into small, not orientated turbulent structures occurs, which additionally promote the entrainment of crossflow material.

The right bottom configuration on figure 5.8 displays the perpendicular jet. On the windward side of the jet large shear layer vortices develop. In comparison to the other three geometries, these front side shear layer vortices show a higher velocity of 5 m/s. But they are not as evenly formed as in the other cases. Generally mostly structures from the lee side of the jet are visible. These structures are similar to the lee side structures of the plain jet. The two symmetric vortex structures occurring in the aligned jet geometry can not be seen in the perpendicular case. Also the turbulent fluctuations in the core region are absent in the perpendicular jet geometry. Within the jet, the perpendicular and the plain geometry are looking very similar. The similarity in the unmixedness factor SMD displayed in figure 5.7 is also visible in the velocity profiles especially for the plain and the

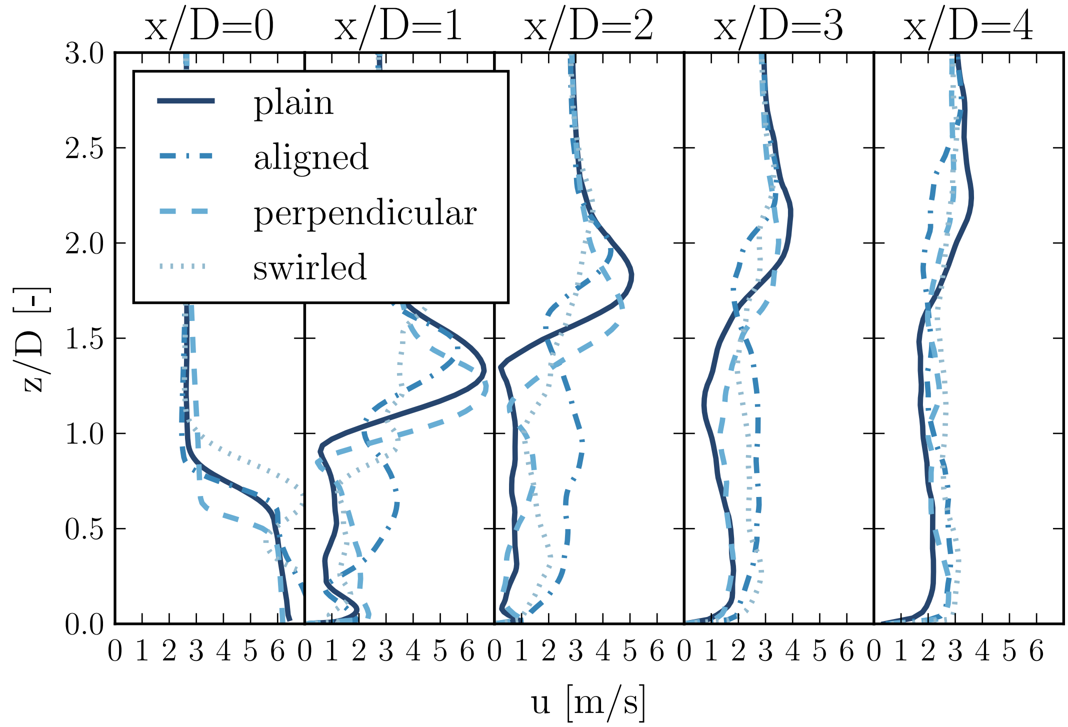

Figure 5.9: Velocity profile of different jet geometries in the symmetry plane on different x/D positions.

perpendicular jet geometry. In figure 5.9 the mean velocity magnitudes at $y/D = 0$ are displayed for all four geometries at different x/D positions. It can be recognized that the velocities from plain and perpendicular jet are very similar while the perpendicular jet penetrates less. The deepest penetration is reached by the aligned jet while retaining a higher velocity all over the intersection region of jet and crossflow. Finally, the velocities from the swirled jet are also displayed. As the swirled jet does not show any symmetry the values in the $y/D = 0$ plane are not as characteristic as they are for the other geometries. Nevertheless, the velocity values from the swirled geometry mostly exceed the velocities from the plain configuration. Therefore an additional factor for mixing speed can be identified in the absolute velocity. From a comparison of the SMD values from figure 5.7 with the velocities from figure 5.9 it can be concluded, that a higher mean velocity magnitude in the jet and crossflow intersection region indicates faster mixing.

For the more detailed investigation of mixing several inlet positions of the plain and aligned jet inlet are seeded with argon. The positions where argon is injected are shown in figure 5.10, where the entrance plane of the jet boundary condition at $z/D = -1$ is displayed. The seeding points can be figured out by their red color representing an argon mass fraction of $Y_{Ar} = 0.01$. The seeding points in the plain and the aligned geometry have the same minimum distance to the wall. This distance is chosen to exclude any influence of the boundary layer on the distribution of the tracer. In the remaining area no argon is introduced. To identify the individual seeding points later on, characteristic labels are assigned. These labels represent the position viewing against the z-direction on the jet exit and are also shown in figure 5.10. Again a momentum ratio of $J = 6$ is considered. Jet as well as crossflow consist of air. The jet air is seeded with the argon pattern shown in figure 5.10 on the left for the plain geometry. Additionally, the crossflow temperature is set to 293 K while the jet temperature is elevated to 393 K (configuration 5, see table D in the Appendix). Configuration 6 is

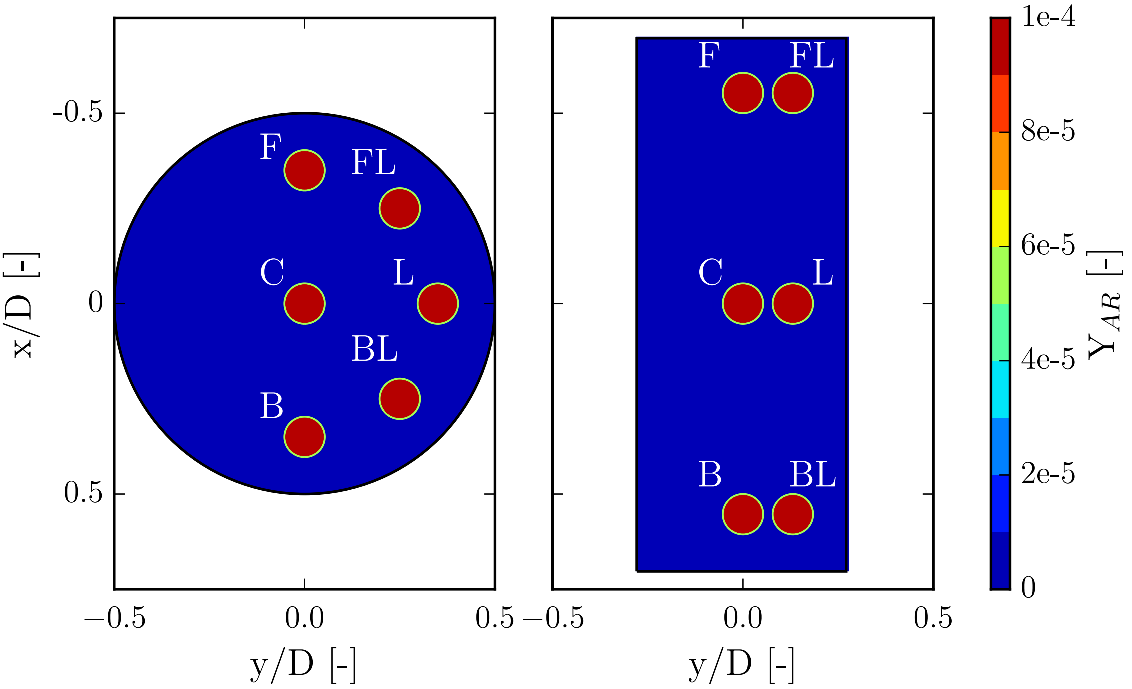

Figure 5.10: Different positions of argon at the jet entrance plane.

the aligned rectangle of 141 mm times 56.2 mm with the same boundary conditions. The seeding postitions are depicted in figure 5.10 on the right. The mean argon concentrations discussed in the following are computed from 5 hydraulic residence times.

For evaluation the plane at $x/D = 4$ is selected. In this plane the results from the different seeding points are shown in figure 5.11 for configuration 5 and in figure 5.12 for configuration 6. First, the results of configuration 5 are discussed. In the first row in figure 5.11 the tracer distribution from the front seeding point (F) is followed by the tracer distribution from the front left seeding point (FL). In the second row results from the center seeding point (C) are shown on the left, the results from the left seeding point (L) on the right. In the last row the back seeding point (B) is displayed on the left and on the right the back left seeding point (BL) is presented. For an easier orientation, the entrance plane including the seeding positions are additionally plotted in the upper left corner. In addition to the argon concentration field an iso contour is displayed in each plot representing the normalized temperature at $\Theta = 0.2$.

To determine the mixing quality of different seeding positions the information from the argon distribution and the isocontour of the normalized temperature are used. The width of the area with argon and the maximum argon concentration in the plane at $x/D = 4$ are two measures for the mixing intensity. The Ar mass fraction can further be assigned to a position in the jet by the iso curve of Θ.

From figure 5.11 it can be clearly seen, that different tracer positions lead to different maximum tracer concentrations. The position F results in the highest maximum concentration whereas the position B leads to the lowest concentration in configuration 5. At the same time, the Ar mass fraction resulting from position F and B are located closely to each other at $x/D = 4$ whereas they differ significantly in their injection position. Ar from position F is exposed soon to the shear layer between jet and cross flow. Ar injected at F interacts with the crossflow, but is not diluted as much as from the other tracer positions. The front shear layer vortices can not spread the tracer. Further the turbulence intensity on the windward side is smaller than on the lee side. The shortest residence time of Ar from position F within the

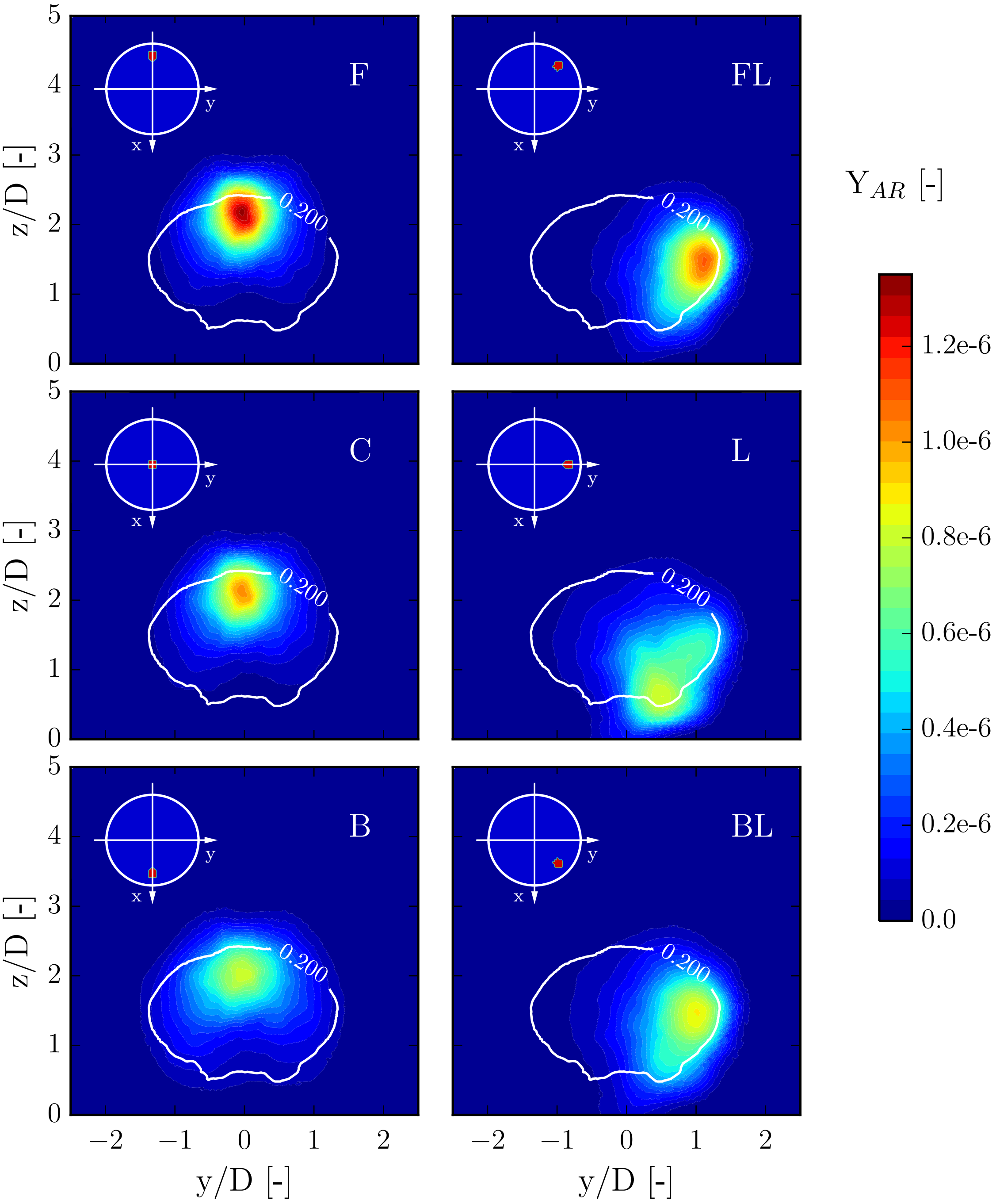

Figure 5.11: Mixing of different positions of the plain jet geometry at $x/D = 4$.

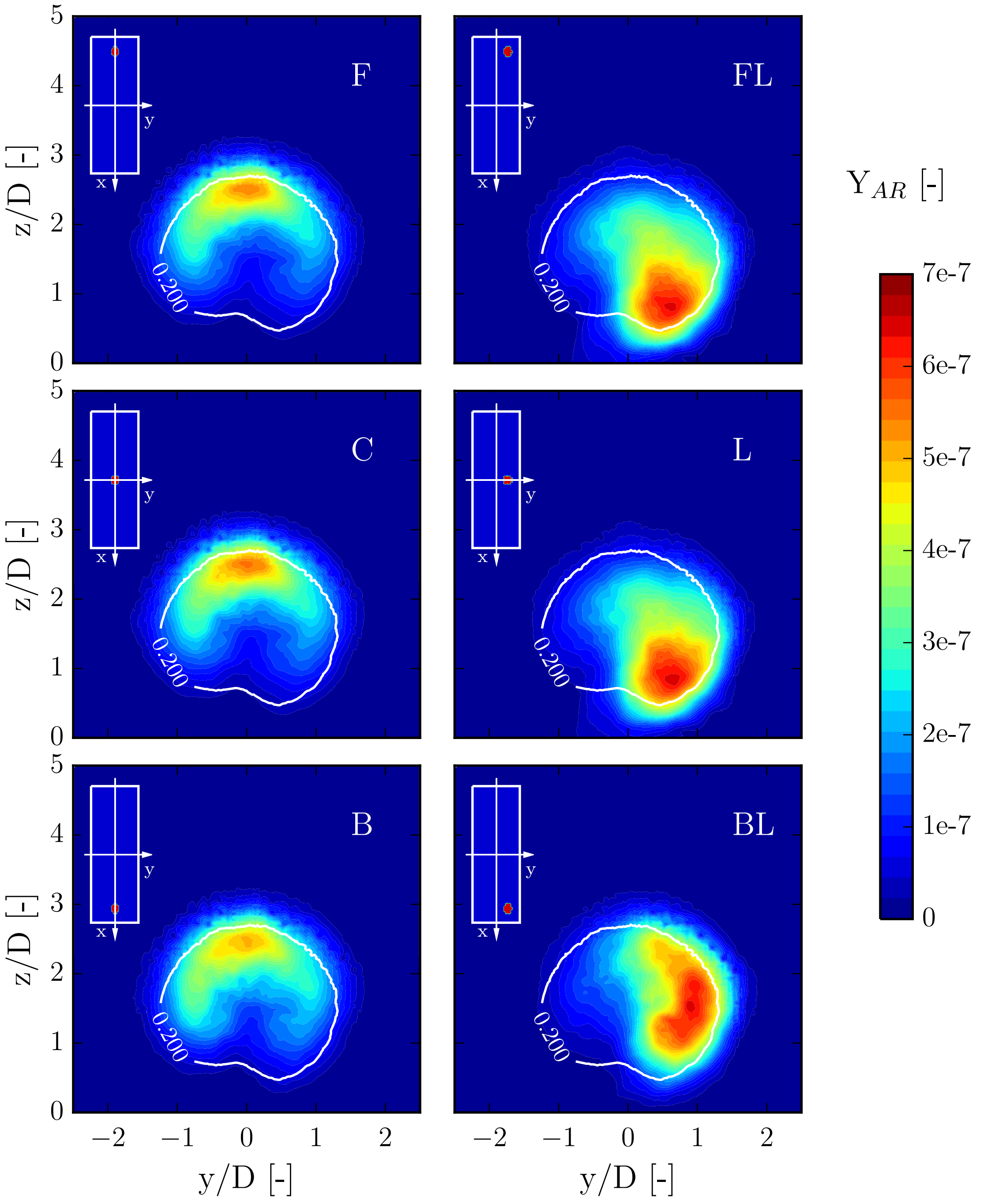

Figure 5.12: Mixing of different positions of the aligned jet geometry at $x/D = 4$.

domain influences the mixing quality also negatively. In contrast, Ar injected at B does not have much contact to crossflow material, but interacts with the large scale counter rotating vortex pair. Further, the momentum in z-direction is preserved for a longer time period, so Ar injected at position B penetrates deeper in z direction than from F or C. These two mechanisms transport Ar injected at B near the windward side of the jet. Simultaneously, the turbulence intensity on the lee side is higher while the residence time is longest. In between is the Ar mass fraction distribution originating from C. The large counter rotating vortex pair and the initial z-momentum move the tracer next to the windward position. At the same time, tracer from position C is exposed in average to a lower turbulence intensity than B while the residence time is longer. This is visible by the maximum Ar mass fraction, which is in between F and B. The results for position FL resemble those from F. Hence, they differ as the results for FL show a lower maximum value but still the second highest within configuration 5. This is mainly caused by the second shortest residence time. The counter rotating vortex pair shifts the concentration field to the outer left edge. Similarily, the results for position L are also shifted clockwise by 45°. But as the residence times grow towards the lee side of the jet, the Ar injected at L is mixed better than from FL, which is enhanced by the higher turbulent intensities. Investigating the path lines for Ar injected at BL, a deeper penetration in z direction can be stated, because the z-momentum is retained for a longer time period than for L or FL. Furthermore, the counter rotating vortex pair interacts only downstream of $x/D = 3$ with Ar injected at BL. The maximum Ar mass fraction is comparable to those of B and L, where turbulence and residence time are comparable to those for position L.

The findings from configuration 5 can not be transferred directly to configuration 6. Comparing figure 5.12 to figure 5.11 it becomes visible that the results differ significantly. Most obvious is that the maximum tracer concentration for the aligned case reaches only 60 % of the plain case. This is in accordance with the mixing quality presented in figure 5.7. The differences in maximum concentration values over all six positions are smaller than for the plain jet. Similar to the smoother concentration distribution a lower scattering of the mean residence time is observed in the aligned case. The residence time variance of all six position in configuration 5 is calculated to $\sigma^2 = 1.89e^{-4}$. For configuration 6, the residence time variance is $\sigma^2 = 2.36e^{-5}$. The residence time in configuration 6 for the positions C and L is comparable to each other and a little smaller than for the other four configurations which have a comparable residence time. The smaller variance within configuration 6 explains the smaller difference between the maximum mass fraction values for the 6 position. But the smaller variance does not explain the absolute lower values. The overall better mixing of the aligned jet in comparison to the plain jet has been stated in figure 5.7 and is explained by the differing vortices (see figure 5.8). In configuration 6, vortex shedding is important right from the beginning of the jet and crossflow interaction on the windward side of the jet. Comparable vortex shedding can also be observed in the plain geometry but not until $x/D = 2$. These vortices enhance the tracer distribution within the flow. Because the mixing enhancement by vorticies occurs earlier in the aligned case the observed concentrations in figure 5.12 are smaller than in figure 5.11. Still the positions FL, L and BL show slightly higher maximum values than the positions F, C and B.

The difference in the mixing history between tracer positions in and away from the symmetry plane can be explained by their penetration depth into the crossflow. The reason is that the initial z-momentum from the injection point displayed in figure 5.10 last for different time periods. Positions on the symmetry plane preserve their z-momentum for a longer time than the other positions. Assuming that mixing improves with increasing residence time and increasing velocity the evaluation of these values explain the different tracer distribution. While the residence times at least for the positions C, B, L and BL are similar, the path length for tracers correlated to the positions C and B is longer. This results in a higher mean velocity for C and B which enhance the mixing. The transport velocity of the tracer can also be derived by imposing mass conservation. The combination of a smaller area with a lower maximum tracer concentration results in a higher transport velocity of the tracer and vice versa. Applying this on figure 5.12 smaller maximum value for the positions F, C and B simultaneously represents a higher mean velocity. Similarly a larger tracered area with higher maximum values indicates a lower mean velocity for the positions FL, L and BL. The transport velocity in the symmetry plane (where F, B and C are located) is higher meanwhile the residence time is almost equal among all positions. This is correlated to a smaller tracer area with a smaller maximum concentration. Vice versa the tracers from positions FL, L and BL are exposed to a smaller transport velocity and exhibits a larger with tracer captured area with higher maximum tracer concentrations.

The location of the tracered area within the jet at $x/D = 4$ in figure 5.12 of position F, C and B almost collapse to the same location. A tendency towards a wider distribution along the counter rotating vortex pair can be seen from position F over C to B. The counter rotating vortex pair interacts more with the tracer from position C and B. The tracer distribution at at $x/D = 4$ from position FL and L collapses also. Even the tracers are located next to the boarder of the jet, an analysis of the mean tracer pathways does not reveal a significant influence of the counter rotating vortex pair on the tracer pathways. Only the Ar mass fraction injected at position BL is influenced by this vortex structure. The counter rotating vortex bend the tracer pathway and distribute Ar over a wider area.

5.3 Reacting Jet in Crossflow

The main objective of this work is to predict reacting jets in crossflow. In section 3.4 an overview of combustion models has been presented including their strengths and weaknesses. From this variety of models the Partially Stirred Reactor (PaSR) model and the Thickened Flame Model (TFM) has been chosen for both practical and theoretical reasons. From a practical point of view, OpenFOAM already provides an implementation of the PaSR model including a solver for finite rate chemistry. From the theoretical point of view, the PaSR model is based on the idea of an imperfect mixture where turbulent mixing on the micro scale is dominant but chemistry is also taken into account. [25]. The result is a micro scale mixing dominated combustion model, where first the mixing criteria must be fulfilled before reaction can take place. The corresponding flame regime can be located in figure 2.3 in the distributed flame zones. But under certain conditions, the Karlowitz numbers for the reacting JIC decrease below one. Where $Ka < 1$, the requirements for the thickened flame regime are fulfilled. Already mentioned by Collin et al. [12], the theoretical derivation of the TFM is based on a artificial thickening of the flame front. Therefore it is expected to outperform the PaSR model in configurations where $Ka < 1$. In the subsequent sections, the validation with experimental velocity measurements is discussed followed by a comparison of the two combustion models.

5.3.1 Velocity Fields

To evaluate the quality of the reacting jet in crossflow simulations, the simulated velocity fields in the symmetry plane are compared with experimental data from PIV measurements. In figure 5.13 the mean velocity contour is displayed. It is calculated from u_x and u_z of configuration 7, which includes the PaSR model, a jet diameter of 100 mm, a momentum ratio of $J = 6$ and $\Phi = 0.66$ of the jet. The mean computed velocity is illustrated on the left whereas on the right the mean velocity measurements are shown. Additionally, streamlines calculated from the mean velocity field are plotted in white to visualize the flow direction. From figure 5.13 good agreement between simulation and experiment can be concluded. The location of the recirculation zone is almost identical for simulation and experiment, but the simulated recirculation zone is shifted by a small amount in positive z-direction. Differences appear in the velocity magnitude. The measurement gives a region of significant low mean velocity magnitude at the windward side of the jet at $0 < z/D < 1.5$. Consequently, close to this low velocity region the velocities within the jet show higher values. The simulation reveals small values at the windward side of the jet only near the jet orifice next to $0 < z/D < 0.25$ forming a stagnation zone. The simulated velocity elsewhere on the windward side is higher, the velocity within the jet is lower than in the experiment. Most obvious is the higher velocity in the jet region from $z/D > 1$ downstream. Also the penetration of the jet into the crossflow is different. The simulation calculates a lower penetration depth than in the experiment. The experimental velocity values next to $z/D = 0.1$ should not be considered because they are distorted by measurement errors due to laser reflection at the bottom metal plate.

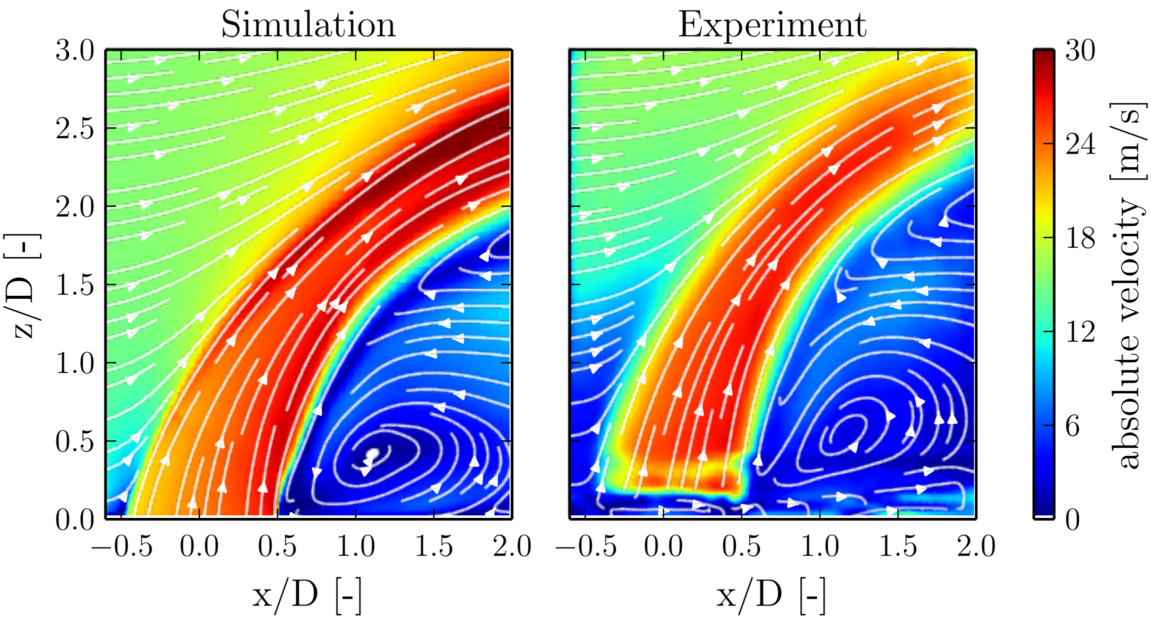

Figure 5.13: Mean velocity magnitude in the symmetry plane $y/D = 0$. On the left simulated values using the PaSR model, on the right experimental data.

In figure 5.14 the configuration is the same as in figure 5.13 but the velocities were computed with the TFM (configuration 8). The agreement between experiment and simulation is better than for the PaSR model. The recirculation zone on the lee side of the jet is computed correctly. Also the velocity magnitude in the jet region from experiment and simulation fits well. The persisting difference between measurement and LES is the less deep penetration of the jet, represented by the trajectory of the maximum mean velocity in z-direction.

Evaluating figure 5.13 and 5.14 in more detail, a line plot showing the velocity magnitude in the symmetry plane over the z-direction on different x/D values is shown in figure 5.15. In addition to figure 5.14 the line plot clearly shows the better agreement of the TFM model with experimental data. The maximum mean velocity magnitude from TFM and experiment is almost identical whereas the results from the PaSR model shows slightly

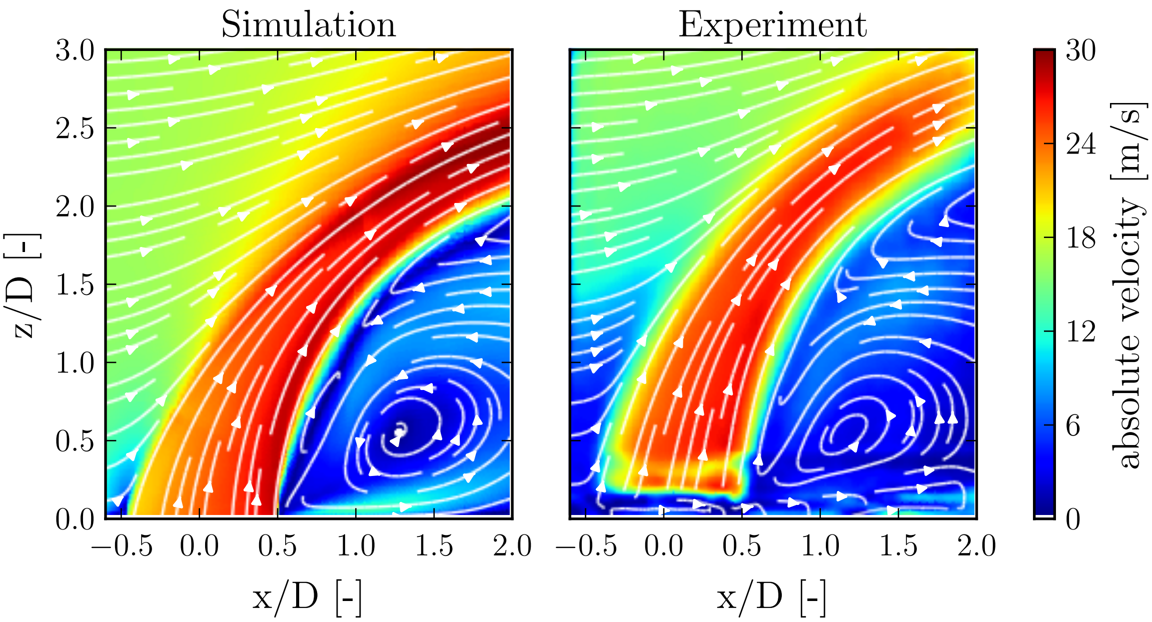

Figure 5.14: Mean velocity magnitude in the symmetry plane $y/D = 0$. On the left simulation values using the TFM model, on the right experimental data.

higher maximum values. The shape of the velocity profiles for the TFM is also closer to the experiment than for the PaSR model. Especially at $x/D = 0$ and $x/D = 0.5$ the PaSR model delivers a velocity peak, which can not be found in the experimental data. Not visible in the experimental data but calculated by both combustion models is a double velocity peak. This double peak is the consequence of the large coherent structures in the shear layer, also known as shear layer vortices [20]. The velocity trajectory, defined by the maximum velocity magnitude in x- and z-direction is underestimated by both combustion models. Whereas the velocities based on the TFM display the lowest penetration depth, the velocities based on the PaSR model show a deeper penetration but do not reach the experimental values. The initial velocities at the simulation boundary for crossflow and jet cannot be made responsible for the different velocity trajectories, as they are identical for simulation and experiment. The initial crossflow

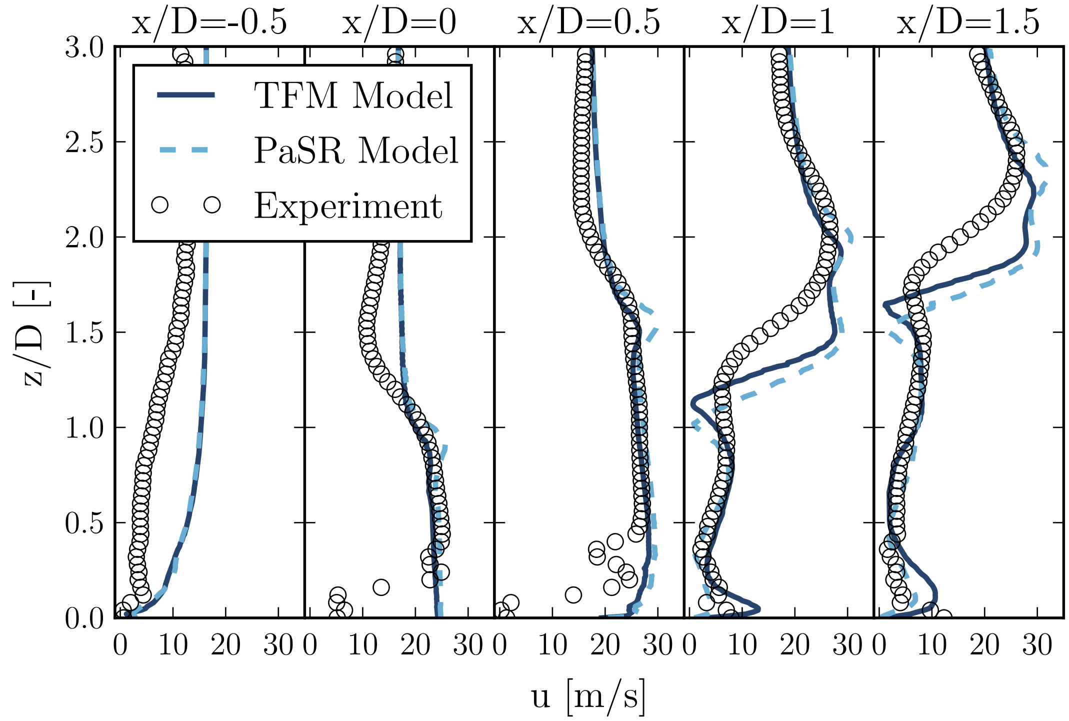

Figure 5.15: Mean velocity magnitude in the symmetry plane $y/D = 0$ at different x/D positions for TFM, PaSR model and experiment.

velocities can be taken from figure 5.16 showing only the x-component from the velocity in figure 5.15. To validate the crossflow velocity, only regions with undisturbed crossflow must be considered. In figure 5.16 simulation and experiment agree very well in the undisturbed region for $z/D > 2.5$. Because no velocity measurements within the jet pipe are available, the location close to the jet exit is chosen for the comparison of the jet velocity where the jet is influenced less by the crossflow. Figure 5.17 displays the z-velocity. As the velocity measurement is distorted next to $z/D = 0$ the agreement can only be estimated by an extension of the reliable data point at $x/D = 0$ until $z/D = 0$. Of course, this method is not very robust, but indicates that the error is small.

Even though the initial crossflow velocity for experiment and simulation agree, the velocity in x-direction at $x/D = -0.5$ differs. Taken from figure 5.16, the x-velocity in the experiment for $0 < z/D < 1.5$ is much lower

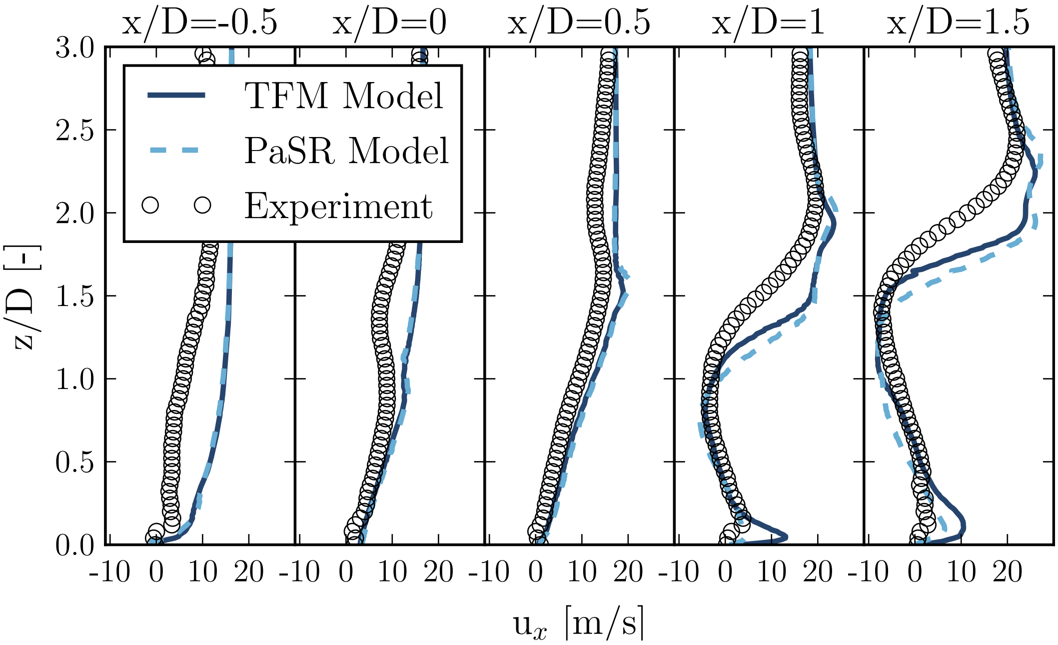

Figure 5.16: Mean x-velocity in the symmetry plane $y/D = 0$ at different x/D positions for reacting JIC at different x/D positions for TFM, PaSR model and experiment.

than in the simulation. The resulting momentum in x-direction differs. The smaller x-momentum results in a slower decay of the z-momentum of the jet, although the initial jet velocity is almost identical. The slower decay of the z-velocity is seen in figure 5.17 at $x/D = 0$ where the experimental velocity for $z/D < 1.25$ is larger than the simulated values. The reason for the lower x-velocity was not found. The cold velocity measurements did not show a similar behavior.

5.3.2 Temperature Fields

The validation so far only considered the velocity data from experiment and simulation. But as chemical reaction is involved, the velocity is not only influenced by fluid dynamic conditions but also by chemical reaction. The heat release during combustion results in a higher temperature which accelerates the flow due a change in density. First the temperature and its distribution is considered.

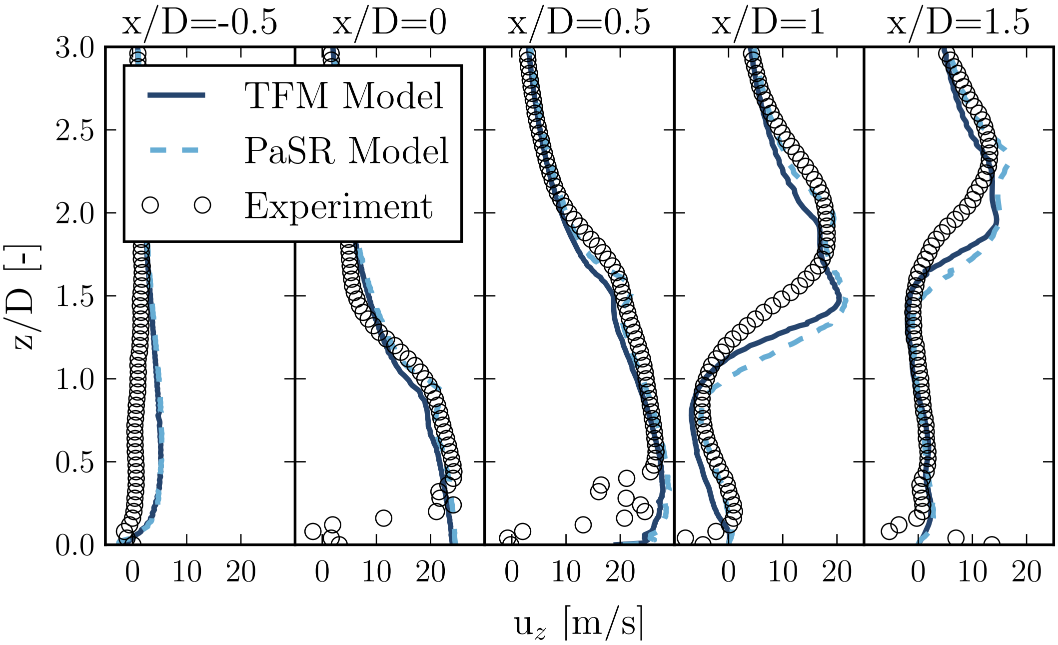

Figure 5.17: Mean z-velocity in the symmetry plane $y/D = 0$ at different x/D positions for reacting JIC at different x/D positions for TFM, PaSR model and experiment.

The temperature field corresponding to configuration 7 is plotted in figure 5.18. Most obvious is the high reaction temperature which exceeds the corresponding adiabatic flame temperature by more than 100 K. Considering different equivalence ratios, an overprediction of temperature is also observed for $\Phi = 0.59$ and for $\Phi = 0.5$. A comparable overprediction of temperature is found for the PaSR model under the same conditions. As already mentioned in section 2.3, the adiabatic flame temperatures from one step chemistry may exceed the actual temperature if the dissociation process of mainly CO_2 plays a role. The adiabatic flame temperature of the displayed configuration of $\Phi = 0.66$ and an initial temperature of $T = 636$ K differs between $T_{ad} = 2044$ K for one step chemistry and $T_{ad} = 2017$ K for the reference mechanism. This is accepted because of the much lower computational time needed to solve the chemistry equations and because the contribution to the temperature excess shown in figure 5.18 is small. The more relevant contribution to this unphysical behavior was identified as a unphysical high source term caused by an inappropriate computational time

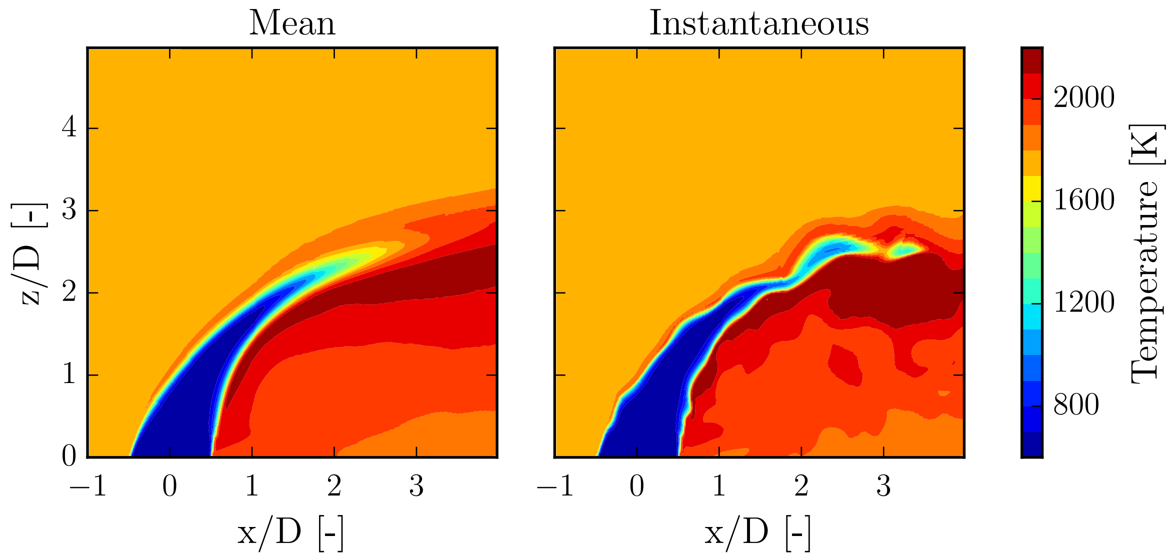

Figure 5.18: Mean (left) and instantaneous (right) temperature in the symmetry plane $y/D = 0$ of configuration 7.

step. Calculations involving chemical reaction shown so far were performed at a local maximum Courant-Friedrich-Levy number of $CFL = 0.25$. This constraint results in a time step of 2.010^{-6} s which is large compared to the chemical time step. Because the source term for each species is fixed during one computational time step, the computed concentration after the regarded time step can be over- or under-estimated. As also the enthalpy equation is directly coupled to the reaction source term, the enthalpy of the mixture can also be over or under estimated. In figure 5.19 an excess of combustion products can be identified. As nitrogen is the species of excess, an over prediction of any other species is compensated by a correction of the nitrogen mass fraction due to the constraint of $\sum_i^N Y_i = 1$. Theoretically, Y_{N_2} is constant over the flame front. But a clear decrease of almost 0.5 percentage points can be noticed. This 0.5 % mass fraction is the amount of products, which are wrongly produced because of the too large time step. A mixture of methane and air containing $Y_{N_2} = 0.7342$ leads to $\Phi = 0.76$ and $T_{ad} = 2181$ K. Moving in x-direction, the combustion products mass fraction decrease due to mixing. At the same time the nitrogen mass fraction increases to the crossflow value, which is larger than in the unburned jet.

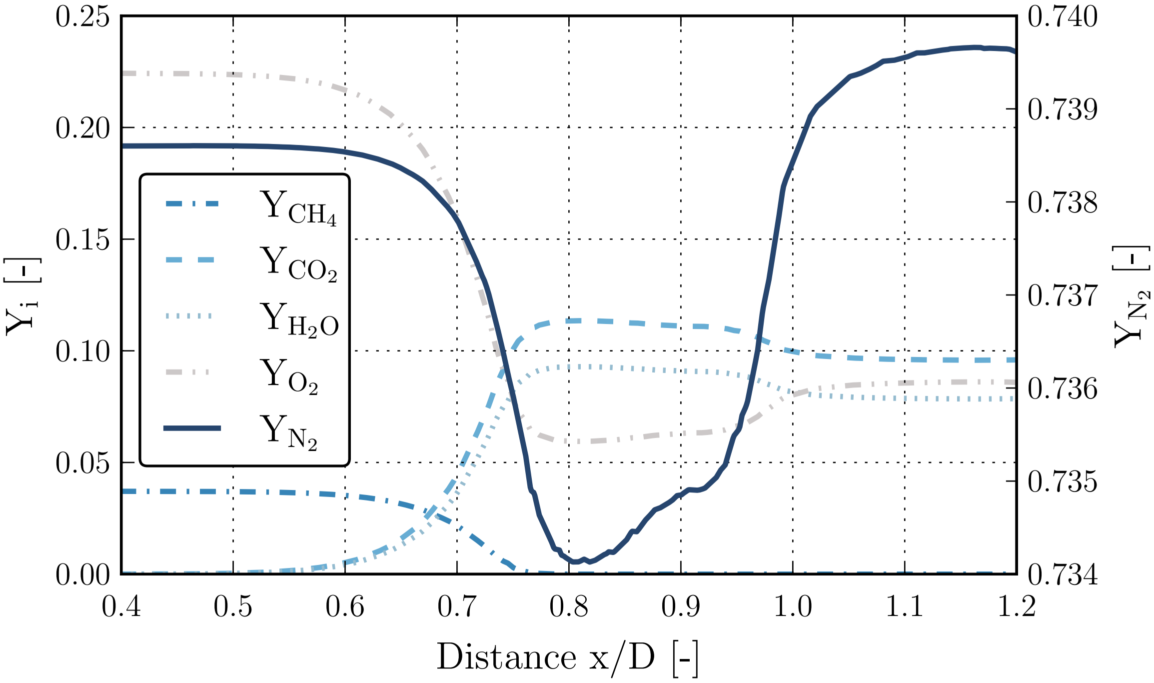

Figure 5.19: Plot over the flame front of figure 5.18 at $z/D = 1$. Mass fraction of species i Y_i on the left y-axis, mass fraction Y_{N_2} on the right y-axis.

In the configuration presented in figure 5.18 especially the back side of the jet is affected because a small cell size coincides with a high velocity and results in a too large time step of 2.010^{-6} s.

The high temperatures at the lee side explains also the higher velocities of the simulation which were already shown in figure 5.14. The higher velocities cause a lower density. The reduced density must be compensated by a higher velocity, as the continuity must be preserved. To overcome the temperature problem, the Courant number was limited to $CFL = 0.1$. At the same time the cell size distribution in the mesh was changed from the adapted mesh in figure 5.1 to a region refined mesh in figure 5.2. Comparing both pictures, it becomes visible that the jet diameter was reduced from 100 mm to 50 mm. The change in jet diameter was first done for conceptional reason in the experiment and afterwards adopted by the simulation to be able to compare experiment and simulation. Unfortunately, velocity measurements

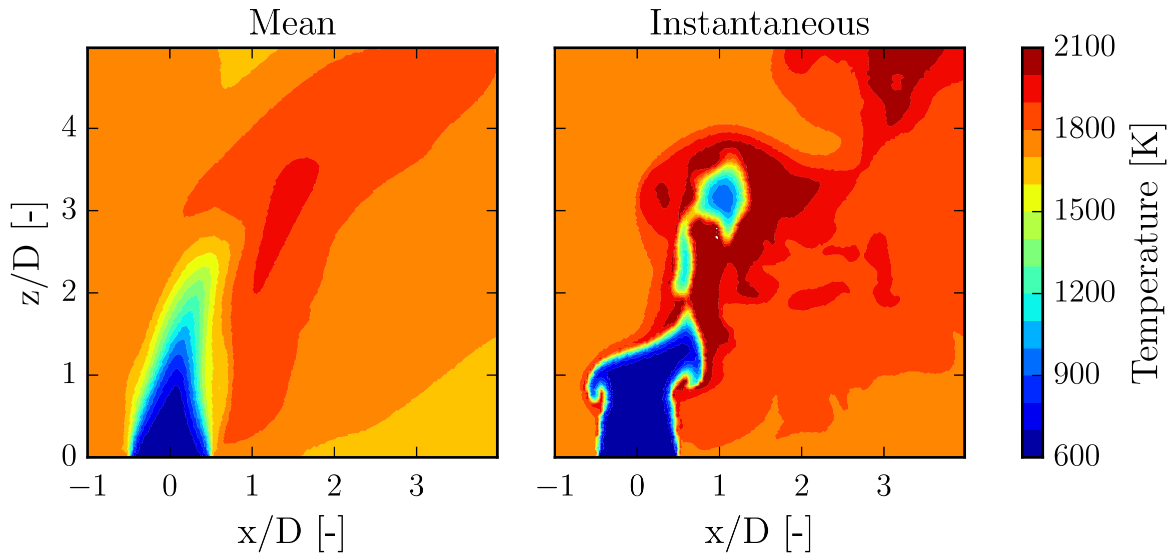

Figure 5.20: Mean (left) and instantaneous (right)temperature in the symmetry plane $y/D = 0$ of configuration 9.

are only available for $D_{jet} = 100$ mm whereas temperature measurements were only performed for $D_{jet} = 50$ mm. Because the LES for one reacting jet in crossflow configuration at $CFL = 0.25$ takes for 20 days of computational time and even more if CFL number is decreased, no calculations for $D_{jet} = 100$ mm and $CFL = 0.1$ were performed. Instead the configuration $D_{jet} = 50$ mm at $CFL = 0.1$ and $J = 15$ were chosen for further code validation.

In figure 5.20 the temperature contour is displayed in the symmetry plane for configuration 9 with $\Phi = 0.66$, $J = 15$ and $D = 50$ mm using the PaSR model and $CFL = 0.1$. The temperature is now in a good agreement with theory as the mean temperatures does not exceed 2000 K. The maximum instantaneous temperatures agree with the theoretical limit of $T_{ad} = 2044$ K.

Resolving the flame front to verify the improvement in chemistry, figure 5.21 displays the instantaneous species mass fraction Y_i at $z/D = 0.4$ (compare figure 5.20). Because the air-methane mixture introduced by the jet contains also $Y_{Ar} = 0.01$ whereas the crossflow does not, the nitrogen mass fraction Y_{N_2} in the unburned jet is lower than in pure crossflow. The formed

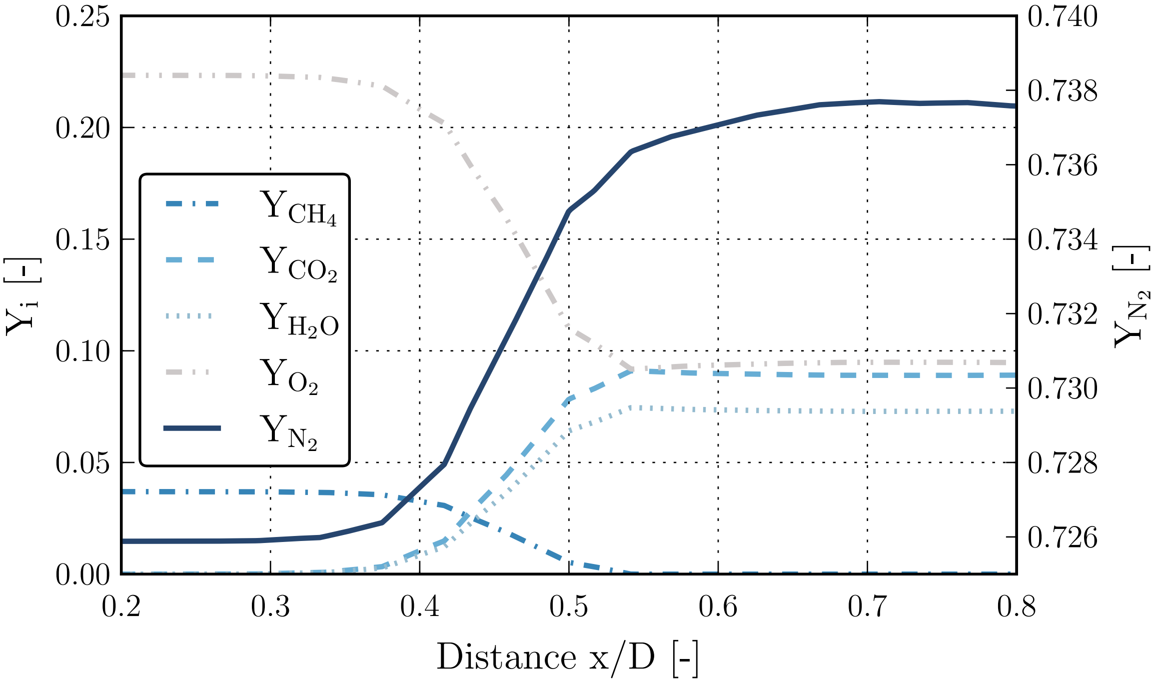

Figure 5.21: Plot over the flame front of figure 5.20 at $z/D = 1$. Mass fraction of species i Y_i on the left y-axis, mass fraction Y_{N_2} on the right y-axis.

combustion products are immediately diluted by crossflow material. Therefore the combustion process can not be separated from the mixing process. Nevertheless it can be clearly stated that no correction due to an excess of combustion products is required any more and the combustion model works correctly. The drawback of the smaller time steps is an almost linear increase of computational cost while the CFL-number is decreased.

A comparison of the mean temperature from simulation and measurements is displayed in figure 5.22. Again, configuration 9 is considered where the PaSR model was used to calculate the reaction progress. The experimental temperature values are computed from CO measurements, which are only available at discrete points. This is possible because CO is in equilibrium at $x/D = 8$. The cold spot in the experiment origins from leakage, leading to intrusion of cold air of ambient temperature. Because of the coarse distribution of measurement points small scale pattern are not captured. In

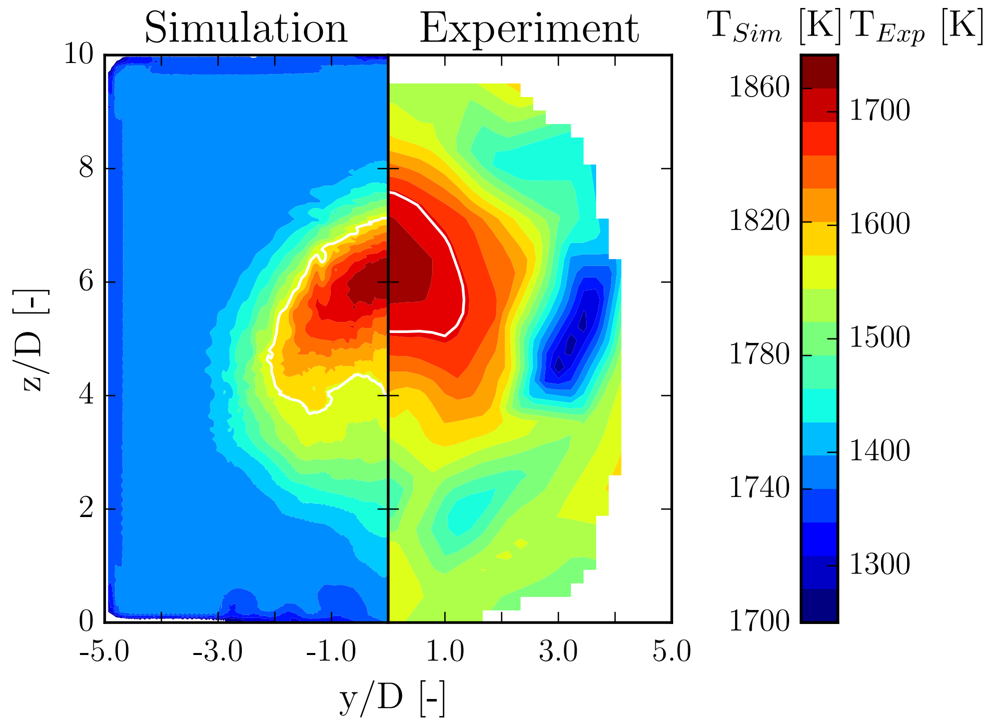

Figure 5.22: Mean temperatures are displayed at $x/D = 8$ one the left from simulation with PaSR model and on the right from experiment.

the regions displayed in white no measurement data is available. Different temperature scales are used because the temperature ranges differs significantly for simulation and experiment. The reason is the heat losses in the experiment. To represent an ideal behavior the simulation is adiabatic with no heat transferred through the walls. Therefore the comparison of temperature is more qualitative and the simulated temperature is difficult to verify. The core region, represented by the maximum temperatures, is located similarly, but still the experiment penetrates slightly deeper into the crossflow. The mixing region, representing the area diluted by the jet, must be judged carefully, as the temperature range in the experiment is different from simulation. Because no uniform experimental crossflow temperature can be identified in figure 5.22, a mixing scalar α can not be computed. To facilitate an orientation despite the different coloring schemes, an isocontour representing a temperature deficit of $\Delta T = 60$ K is defined, which is plotted in white color into figure 5.22. From this isocontour faster mixing is indicated for the simulation, because the area included by the isocontour is larger. Also the shape of the isocontour in the simulation is closer to the kidney shape mentioned in literature [49].

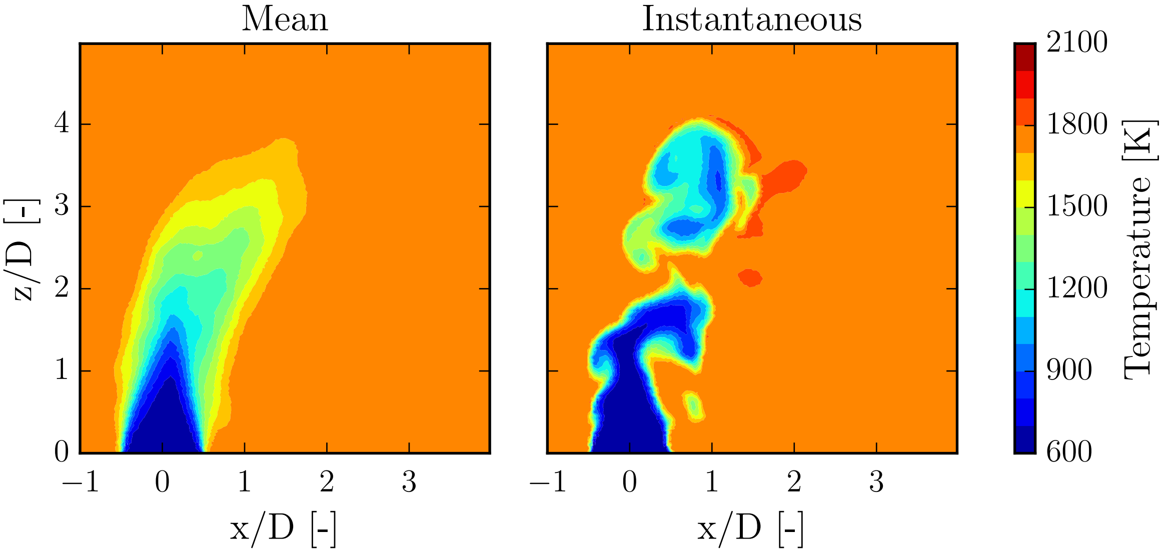

Figure 5.23: Mean (left) and instantaneous (right)temperature in the symmetry plane $y/D = 0$ of configuration 10.

Using the same boundary conditions for configuration 9 but changing the combustion model to TFM leads to configuration 10. The mean and instantaneous temperature of configuration 10 are shown in the symmetry plane in figure 5.23. Comparing both combustion models regarding the mean temperature between figure 5.20 and 5.23, a similar penetration of the undisturbed core of the jet at $T_{jet} = 636K$ can be figured out. But the transition from cold jet to burned products is different, as the mean temperature distributions in the region of combustion and further downstream differ. In figure 5.23 the maximum temperature is 1792 K. In comparison, the PaSR model predicts almost 2000 K for the mean temperature. Also the temperature gradients are larger in the PaSR model than in the TFM. The heat release rate is integrated over the flame surface for both combustion models to check whether the global energy input is correct. The mean heat release rate corresponding to configuration 9 is 71420 Js^{-1} and for configuration 10 71329

Js^{-1}. The theoretical calculation of the heat release rate gives 71389 Js^{-1}. A slight difference can be explained by the turbulence generator applied at the boundary, causing small mass flow fluctuations although they are explicitly treated, as mentioned in section C. The key to explain the different temperature profiles is the different size of the heat release area. Already from the instant temperature distribution in figure 5.20 and figure 5.23 it can be concluded that the combustion process in the PaSR model proceeds faster than in the TFM. This is depicted by the larger areas with temperatures below the crossflow temperature. More information can be gained from figure 5.24 where the instantaneous values from figure 5.20 and 5.23 are displayed with the same color scale. Additionally, a contour symbolizing one tenth of the maximum heat release rate is plotted in black. Interpreting the area surrounded by the black line as flame, the larger heat release area of the TFM is clearly noticeable in figure 5.24. Also the artificially thickened flame front, described in section 3.4, can be observed. Furthermore, different temperatures of the unburnt gas can be distinguished. The sub-

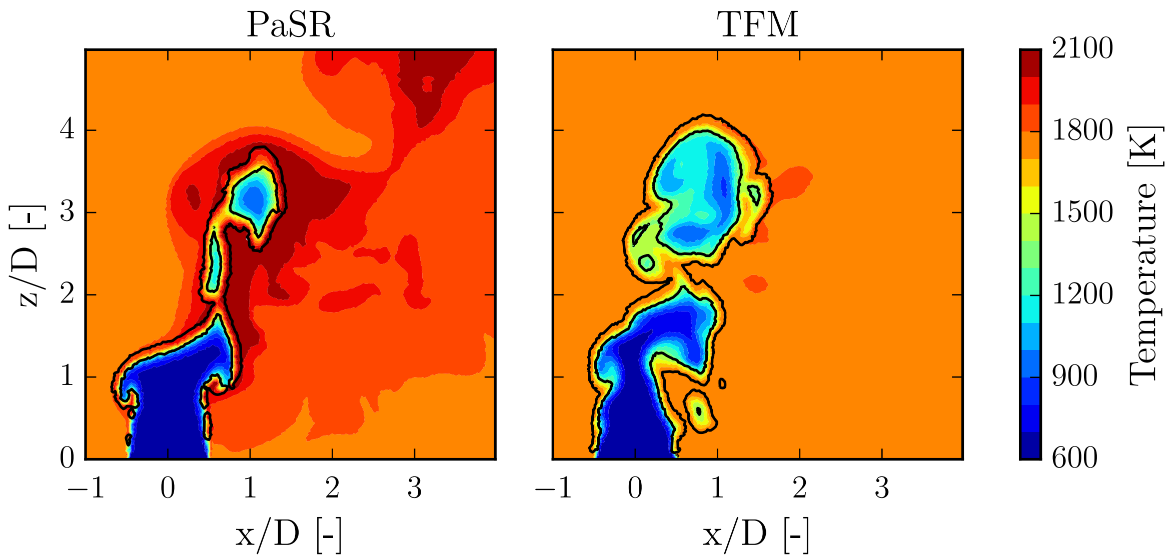

Figure 5.24: Instantaneous temperature in the symmetry plane $y/D = 0$ using PaSR (left) and TFM (right) at $\Phi = 0.66$, $J = 15$ and $D = 50$ mm. In black color a contour is plotted representing 10 % of the maximum heat release rate.

stantial temperature change in the unburned gas is controlled by convection as the diffusion process is comparable slow. Therefore temperature is also a indicator for mixing with crossflow material. Right at the jet exit both combustion models consume unburned gas at the composition and temperature defined at the inlet boundary. Moving downstream on the jet trajectory, the TFM shows an increasing region of rising temperature of the unburned reactants. In the PaSR model, the preheating is way smaller and limited to regions very close to the flame front as long as the flame front is not interrupted. Following the jet trajectory even further downstream, pockets of unburned gas get separated in both combustion models and burn along separated flame fronts. But the temperature of these unburned gas pockets is higher in TFM than in the PaSR model. Moving downstream on the trajectory and leaving the combustion zone, a higher temperature in the PaSR model become visible.

Transferring the insight from the instantaneous values back to the mean values in figure 5.20 and 5.23 the higher mean temperature gradient of the PaSR model reveals a fast combustion process both in time and in space. A thicker flame front for the TFM is expected from theory, but it also shows a slower combustion process in time. These differences in mean consumption speed of the unburned gas has two different effects: First, the heat of combustion in the TFM is distributed over a larger area compared to the PaSR model. This supports the equal distribution of the temperature and reduces the peak temperatures. The result is a lower maximum temperature in the TFM with respect to the PaSR model. Secondly, as the heat release is distributed over a longer distance along the trajectory, the penetration depth in z-direction of the jet in the TFM is lower. In the PaSR model, the fuel consumption is faster and therefore produces a higher momentum in z-direction. As the fuel consumption process in the TFM is slower while starting at the same location, the flame is distributed over a wider area. This results in a lower z-momentum as the orientation of the jet trajectory is already altered in x-direction when combustion still takes place.

That the penetration predicted by the TFM is lower can also be seen in figure 5.25. The mean temperature distribution from configuration 10 is plotted on the left whereas on the right the measurements are displayed. The

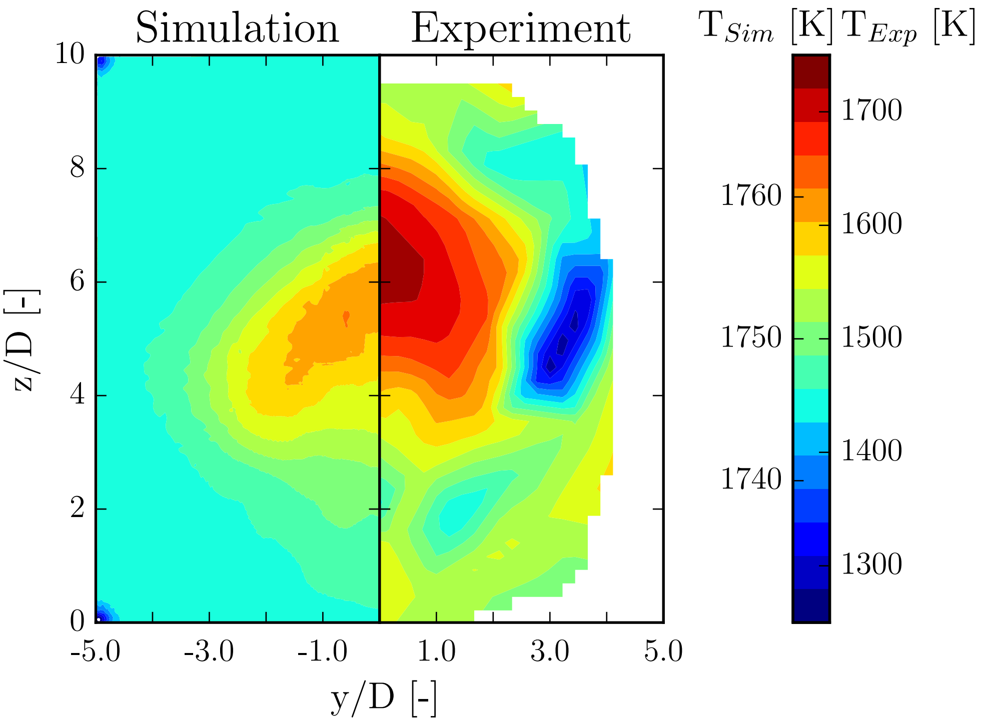

Figure 5.25: Mean temperatures are displayed at $x/D = 8$ one the left from simulation with TFM model and on the right from experiment.

lower maximum values already discussed are clearly visible. The maximum difference between maximum temperature and crossflow temperature is reduced in comparison with figure 5.22 by 20 K. The simulated temperature of the jet core with TFM is much closer to the experimental values. However, the different thermal boundary conditions of simulation and experiment make direct comparison difficult, as already mentioned in the analyses of figure 5.22. But as the temperature in the core differs only slightly within a range of 10 K to 30 K the simulated NO_x concentrations from configuration 10 presented later should be closer to experimental values than those from configuration 9.

5.3.3 Heat Release

After the temperature distributions have been discussed in the last section, the computed heat release will be presented in the following.

To explain the different temperature distributions the distribution of fuel is investigated below. In figure 5.26 the mass fraction of methane Y_{CH_4} in the symmetry plane for the configuration 9 (left) and 10 (right) is displayed. In addition a contour representing the location of 10 % of the maximum heat release rate is added to figure 5.26. The CH_4 mass fraction of the unburned gas is closely related to the temperature distribution in the same region. A lower temperature relates to a higher CH_4 concentration and vice versa. The temperature rise of the unburned region is not caused by the combustion process but by mixing with the crossflow. This is also visible in figure 5.27, where the argon mass fractions from configuration 9 and 10 are shown. Only the jet is homogeneously seeded with $X_{Ar} = 0.01$. The dilution of argon is only possible due to crossflow material which contains no argon. The combustion process of the PaSR model differs from the TFM

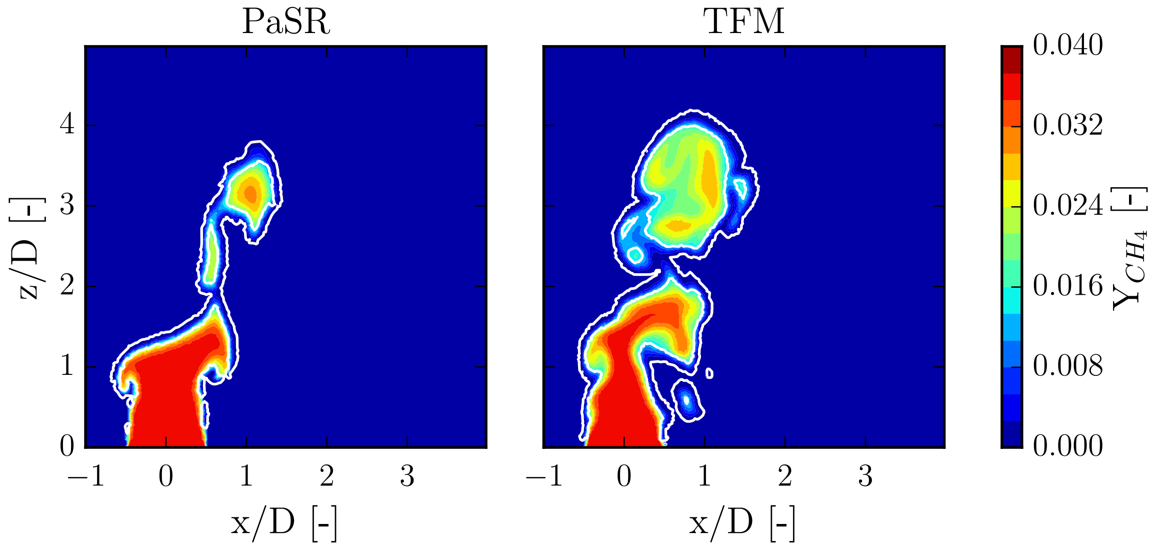

Figure 5.26: Instantaneous Y_{CH_4} in the symmetry plane $y/D = 0$ using PaSR (left) and TFM (right) at $\Phi = 0.66$, $J = 15$ and $D = 50$ mm. A contour is plotted in white color representing 10 % of the maximum heat release rate.

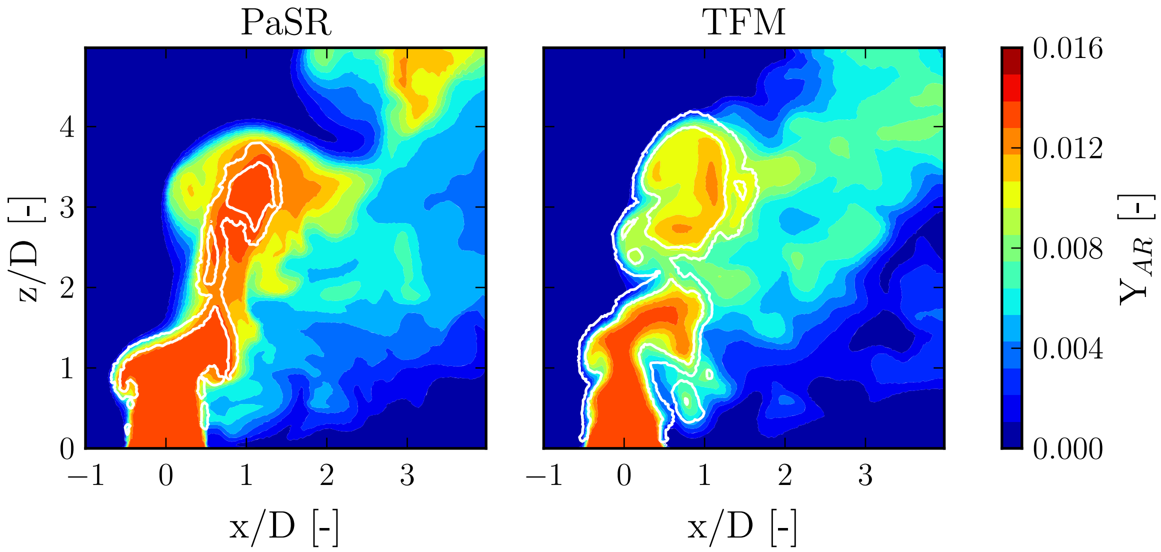

Figure 5.27: Instantaneous Y_{Ar} in the symmetry plane $y/D = 0$ using PaSR (left) and TFM (right) at $\Phi = 0.66$, $J = 15$ and $D = 50$ mm. A contour is plotted in white representing 10 % of the maximum heat release rate.

because a different reactants composition is consumed by the flame. This is indicated by the temperature distribution and verified by the Y_{Ar} and Y_{CH_4} distributions. The combustion process of the PaSR model proceeds quickly enough, so that the flame front has almost no contact with the crossflow. The flame gets separated from the crossflow by its own combustion products. Therefore in the PaSR model the reactants are not diluted or only diluted to a small extend by the crossflow material. This results in higher peak temperatures. However, the TFM allows mixing of unburned jet and crossflow material because the combustion process is slower. At least the flame front of the TFM on the windward side of the jet is always in direct contact with pure crossflow material. Therefore the flame can be directly influenced by crossflow material, which interacts with the flame front.

OH$*$ measurements are available from experimental investigations for the flame of configuration 9 and 10. Although the OH$*$ signal can not be directly substituted by heat release, it is an useful indicator for the flame position. In the simulation, flame position is correlated to the heat release

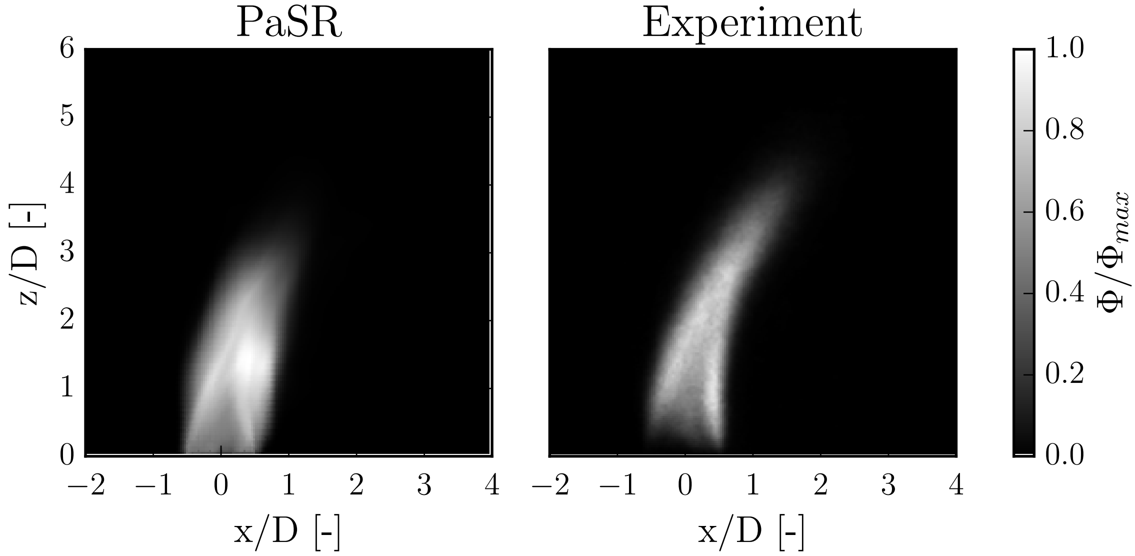

Figure 5.28: Line of sight integrated mean heat release rate of configuration 9 on the left and OH∗ measurements on the right.

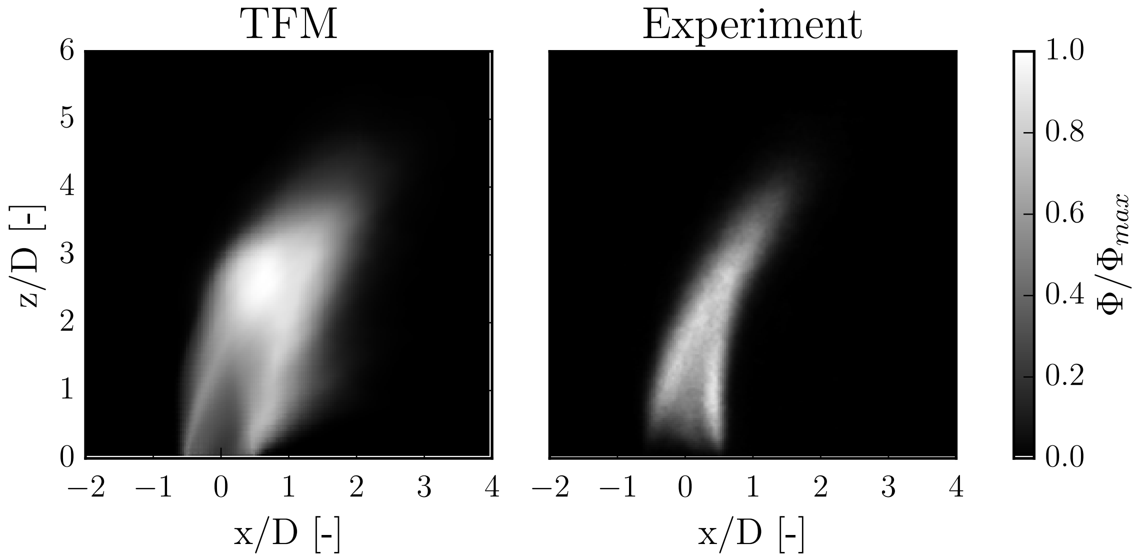

Figure 5.29: Line of sight integrated mean heat release rate of configuration 10 on the left and OH∗ measurements on the right.

rate. Because the OH∗ signal is integrated over line of sight, a comparable signal must be generated for the simulation. To achieve this, the heat release rate is sampled for a series of planes which are orientated normaly to the y-direction at a distance of 1 mm. Afterwards, each node value is integrated along line of sight. The result of this procedure is a plane containing the line of sight integrated value at each node. The integrated heat release rates are normalized by their maximum values. In figure 5.28, the line of sight integrated mean heat release rate of configuration 9 is displayed on the left whereas corresponding OH$*$ signals from experiment are displayed on the right. Φ represent either the heat release rate $\dot{Q}$ or the OH$*$ intensity, respectively. Only the PaSR model predicts a flame shape similar to the flame shape of the experiment. Both mean flame positions resemble a triangle which is slightly bend in x-direction. But the experimental flame tip is at higher z/D than the simulated flame tip. Also the motion of the flame front in x-direction changes with time. The simulation shows a wider distribution of the flame front location than the experiment.

The comparison of the line of sight integrated mean heat release rate of configuration 10 with OH$*$ measurements is shown in figure 5.29. The flame length in z-direction of the TFM is the same as for the experiment. But the simulated flame is wider than the flame in the experiment. The mean values do not show a clear flame front but a blurred area covered by the flame. Therefore, the flame does not exhibit the triangular shape. The simulated flame covers more than twice the area than the experimental flame. The TFM differs in the location of the highest heat release rate: The most reactive region is located at the windward side at $z/D = 2.5$ whereas the experimental flame and the flame computed with the PaSR model have the most reactive region on the lee side of the jet at $z/D = 1$ and $z/D = 1.5$, respectively. This is in accordance with the findings from the temperature profile. Consequently, the combustion process computed with the PaSR model is faster than the experimental and the TFM predicts the slower combustion. Furthermore, the flame attachment on the orifice of the jet exit is different. In the experiment the flame is attached to the jet orifice at the lee side and it is increasingly lifted towards the windward side. In contrast to the experiment, the mean computed flames are always attached to the whole circumference of the jet exit and do not show any lift off. However, there is a stochastic detachment of the flame as shown in figure 5.26, but it reattaches in between these events.

5.4 Nitrogen Oxide Formation

When developing a design tool for a jet in crossflow combustion process, not only the consumption of fuel must be calculated but also the formation of NO_x must be predicted correctly. Therefore, a NO_x model has been developed which is described in section 3.5. This model is combined with the TFM and PaSR model. In the following, the results are presented and validated with measurements. Afterwards the NO_x formation process is discussed in greater detail.

5.4.1 Model Validation

Simulated values are compared to measurements in order to validate the quality of the NO_x model. The NO_x values of configuration 9 and the experiment are shown in figure 5.30. Because the mean peak temperature of the simulation with the PaSR model exceeds the measured temperature by 160 K the NO_x concentrations differs significantly. In order to directly compare the NO_x concentrations a scaling of the NO_x values is done based on the maximum mean temperature and residence time. The scaling factor is calculated from a free flame simulation using Cantera. Therein, the adiabatic flame temperature is adjusted to the maximum mean temperature from simulation and experiment. This is achieved by adjusting the temperature of the reactants while keeping the equivalence ratio of $\Phi = 0.66$ fixed. The NO_x concentration from the free flame at the residence time of 15 ms is extracted. The scaling factor is calculated by dividing the NO_x concentration of the experiment by the NO_x concentration of simulation. The scaling factor is only applied to the products of the jet. The cross flow does not contain NO_x from the beginning to be able to focus on the mechanisms which are assigned to the combustion of the jet. Figure 5.30 (left) shows the result of the scaling procedure for the simulation using the PaSR model, the measurements are shown on the right. The NO_x values are normalized to 15 % oxygen. The experimental values are taken from the same measurement series as the temperature values which are shown in figures 5.20 and

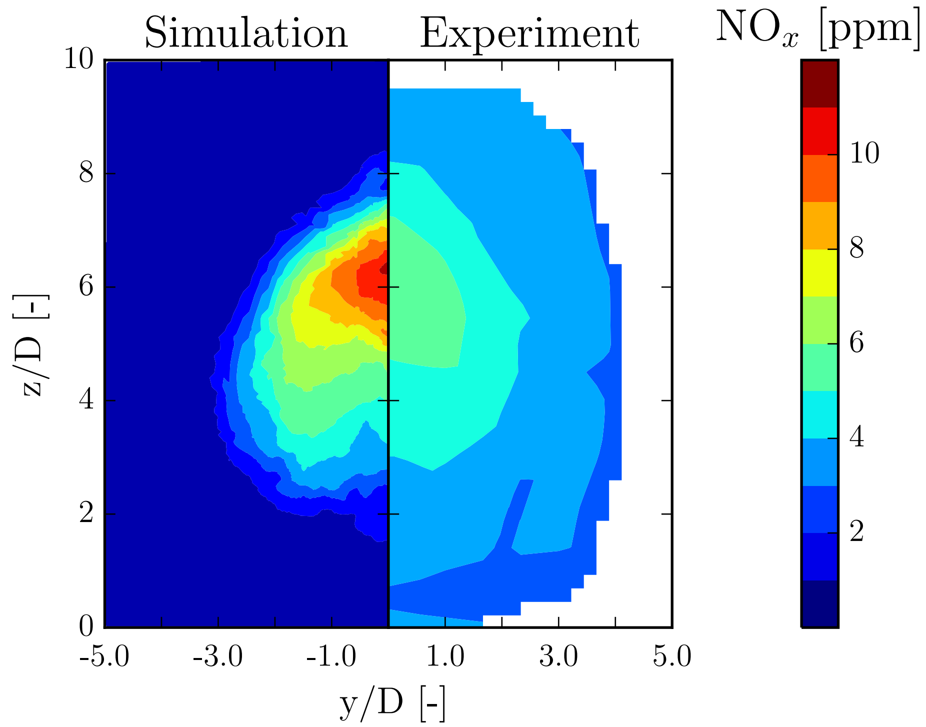

Figure 5.30: NO$_x$ concentration of simulation of configuration 9 (left) and experiment (right) are displayed in ppm and normalized to 15 %.

5.23.

Although scaling was applied, the simulated maximum concentrations still exceeds the experimental values. At the same time, the experiment shows an increasing NO$_x$ concentration in that region, where no jet material is predicted by the simulation. Probably, the leakage air, visible in figure 5.22, is responsible for the wider distribution of the elevated NO$_x$ concentration in these regions where no jet material is predicted by the simulation. Simultaneously, this process reduces the maximum concentration of NO$_x$ within the jet by convective transport into outer regions. A different NO$_x$ distribution is shown in figure 5.31, which is calculated from configuration 10. In contrast to figure 5.30 no scaling was applied as the temperatures between configuration 10 and experiment differ only by 20 K (see section 5.3.2). Additionally, y- and z-velocity streamlines are included in white color. The location of the highest simulated NO$_x$ concentration is shifted to smaller

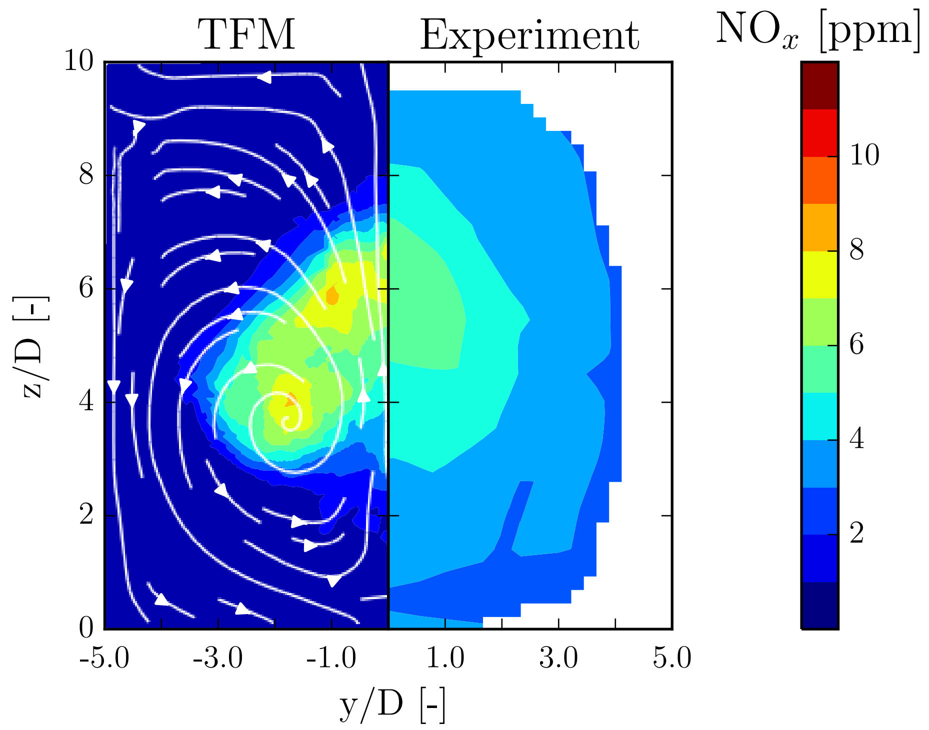

Figure 5.31: NO_x concentration of simulation of configuration 10 (left) and experiment (right) are displayed in ppm and normalized to 15 % oxygen.

z-values because the jet does not penetrate as deep as in the experiment. At the same time, the NO_x concentration from configuration 10 spreads more in y direction than the NO_x concentration from configuration 9. The maximum NO_x concentration is no longer located near the symmetry plane but in the center of the counter rotating vortex pair. A second NO_x peak is located close to the symmetry plane next to the front shear layer. A direct comparison of the absolute computed values from figure 5.31 and figure 5.30 results in lower maximum values for the TFM model. But still the values based on the TFM slightly exceed the experimental data.

5.4.2 Analysis of NO_x formation

At first, NO_x formation in the simulation with the PaSR model is discussed. In the second part of this section the differences between NO_x calculated with the TFM and the PaSR model are analyzed. The NO_x formation path is investigated from downstream to upstream starting with the results at the measurement plane.

The mean temperatures of configuration 9 in the measurement plane $x/D = 8$ are displayed in the left part of figure 5.32. The white colored iso-curves for 6, 8 and 10 ppm NO_x show a gradient towards the jet center. On the right of figure 5.32 the residence times are displayed which are calculated from tracers following the mean velocity field. The starting point of the tracer in the crossflow is the crossflow inlet at $x/D = -2$, the starting point within the jet is at $z/D = 0$.

From the iso-curves for NO_x concentration and temperature it can be concluded that a higher temperature results in higher NO_x concentration. This had to be expected since NO_x formation shows an exponential dependency on temperature. But comparing residence time and NO_x concentration, the lowest residence time of about 15 ms coincides with 6 to 8 ppm NO_x. Similarly, the region of the residence time of 45 ms does not show higher NO_x concentrations. These observations suggest that the influence of residence time on the NO_x concentration is not the dominant factor.

The theoretical formation of NO_x in a one dimensional flame can be separated into two steps which have already been discussed in section 3.5. The first step occuring within the flame front is dominant at the given temperature, pressure and equivalence ratio. The second step, consisting of the Zeldovich mechanism, plays also an important role, but finally adds less than 50 % to the total NO_x concentration. The same conclusion can be derived from figure 5.33, where mean values for $\dot{\omega}_{NO}$ of configuration 9 are displayed on the left and an instantaneous contour on the right. The instantaneous contour shows the largest source term within the flame front, whereas downstream of the flame only intermittent regions reach significant values for $\dot{\omega}_{NO}$. These intermittent regions show higher temperatures than the environment and are formed by the coherent structures generated in the front shear layer. In the mean contour, the NO_x source term is higher where the mean flame is located. Afterwards, the source term decreases in downstream direction. This decrease is due to the mixing process of jet and crossflow which reduces the temperature. The resulting mean NO_x mass

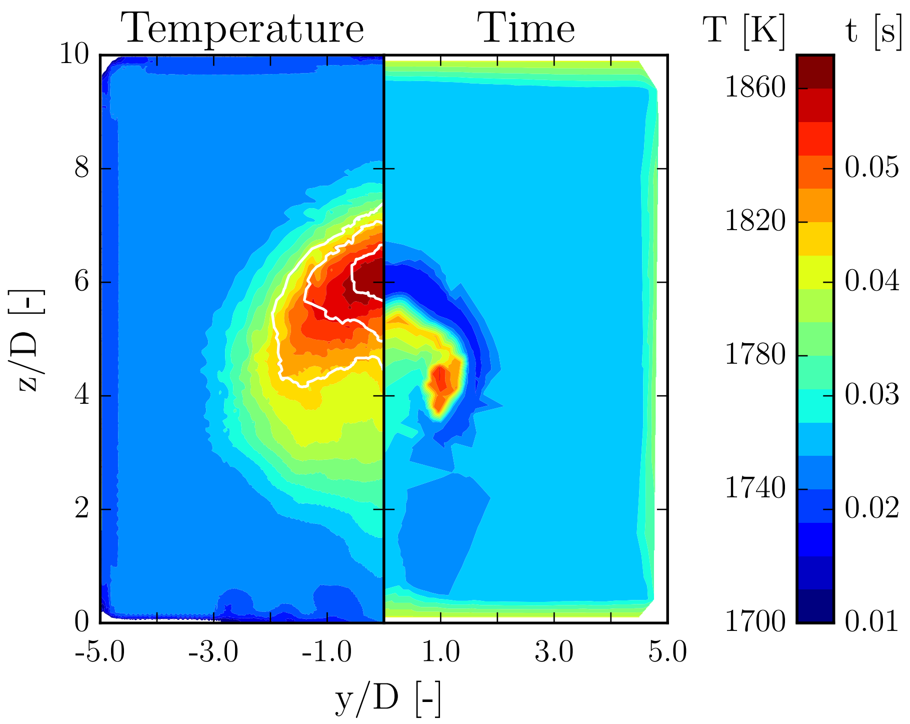

Figure 5.32: Mean temperature and residence time of PaSR combustion model at a plane normal to the x-direction at $x/D = 8$.

fraction is plotted in the left part of figure 5.34, $Y_{\mathrm{NO_x}}$ of the instantaneous state of figure 5.33 on the right. The source terms in the post flame region only add small amounts of $Y_{\mathrm{NO_x}}$ because the maximum instantaneous $\mathrm{NO_x}$ mass fraction is present in the flame tip. The same result is found within one dimensional laminar flames. Thus, results from one dimensional flame configurations can be compared to the time mean reacting jet in crossflow. But different to the one dimensional flame, the process is not continuous in space, because of the intermittent temperature distribution. Unfortunately the intermittent temperature distribution complicates the exact specification of representative one dimensional flames.

In figure 5.35 the mean contour of $\dot{\omega}_{NO}$ of configuration 9 is plotted in the left column and instantaneous values in the right column. The values are shown at planes normal to the z-axis. In the first row, the plane is located at $z/D = 1$, in the second row at $z/D = 2$ and in the third row at $z/D = 3$. Similar to figure 5.33, the largest source term is located at the

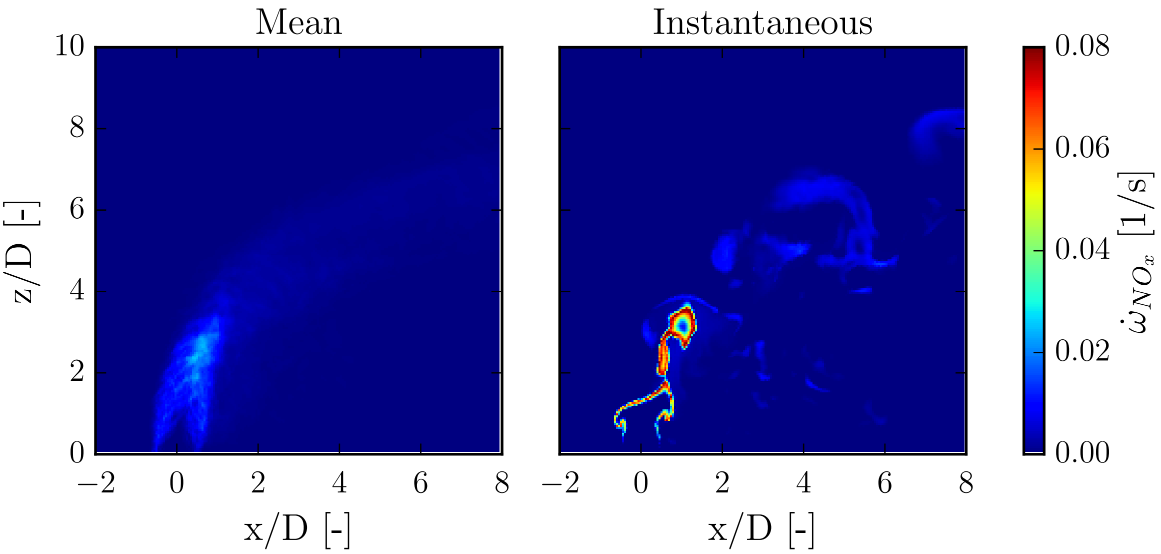

Figure 5.33: Mean (left) and instantaneous (right) reaction rates $\dot{\omega}_{NO}$ on the symmetry plane of configuration 9.

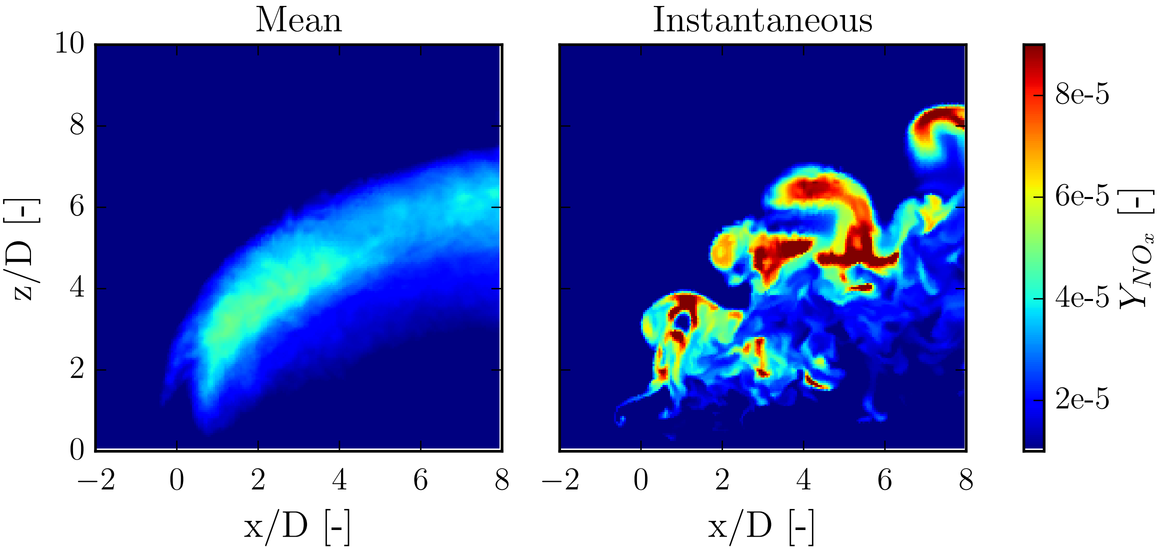

Figure 5.34: Mean (left) and instantaneous (right) NO_x mass fraction on the symmetry plane for configuration 9.

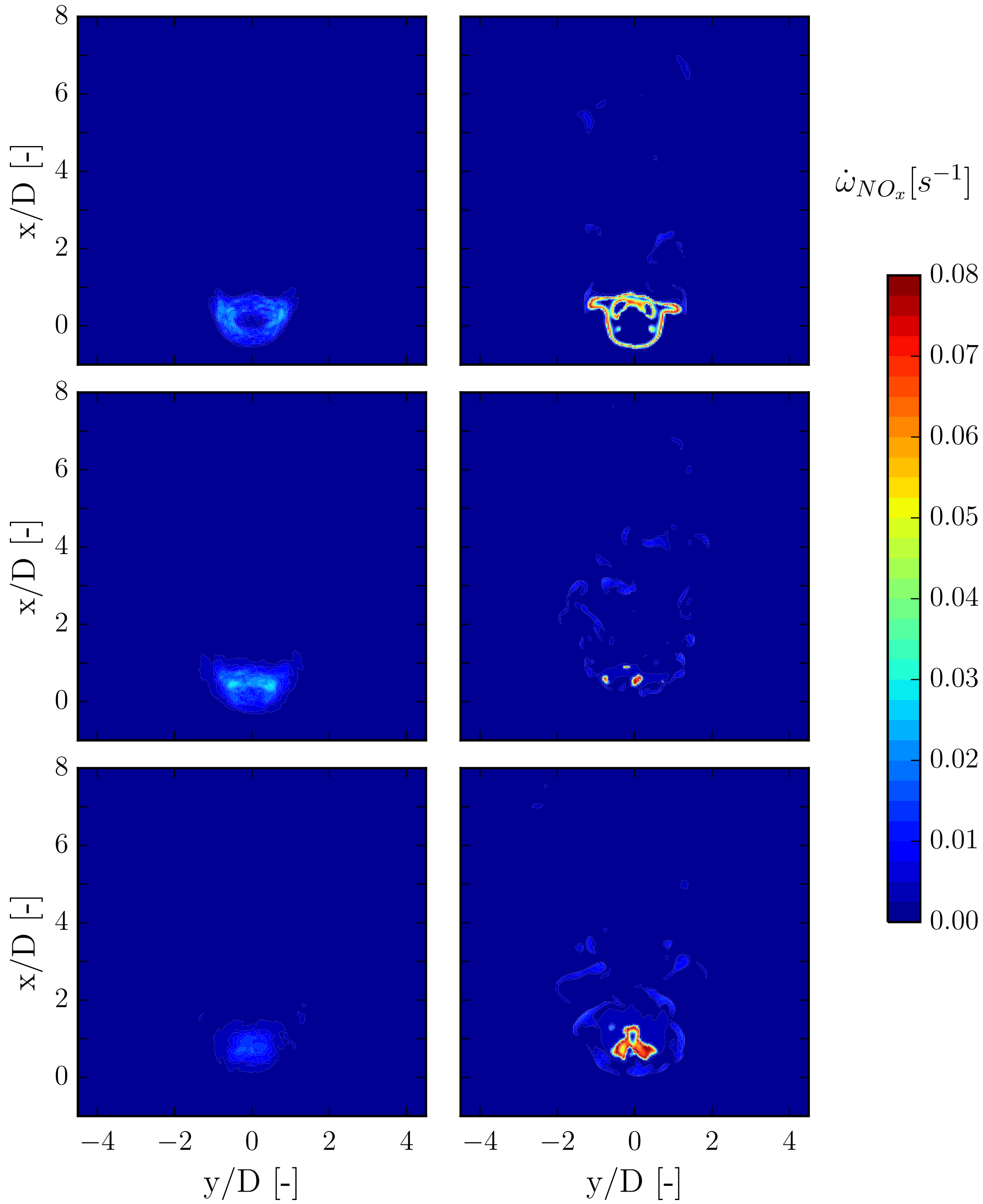

Figure 5.35: Mean (left) and instantaneous (right) reaction rates $\dot{\omega}_{NO}$ at $z/D = 1$ (first row), $z/D = 2$ (second row) and $z/D = 3$ (third row) for configuration 9.

position where combustion takes place. For $z/D = 1$, the distribution of the reaction rate for the instantaneous values is almost symmetric, at least close to the flame. The symmetrical behavior is visible in 80 % of the computed time while the geometrical shape is varying.

A higher value of mean and instant $\dot{\omega}_{NO}$ is present at $x/D = 0.5$ and $y/D = \pm 0.5$. At $z/D = 2$ the irregular structure dominates the instantaneous contour and symmetry can not be identified. However, the mean values still contain two symmetric peak values. The plane at $z/D = 3$ displays an unsymmetrical $\dot{\omega}_{NO}$ contour while the mean values contain one peak instead of two. The absolute mean values of $\dot{\omega}_{NO}$ at $z/D = 3$ decrease compared to the upstream planes because the combustion process is mostly completed below $z/D = 3$. The remaining flame has a very small flame surface and only that region produces significant $\dot{\omega}_{NO}$ values.

The mass fraction Y_{NO_x} resulting from $\dot{\omega}_{NO_x}$ is shown in figure 5.36. The contours of Y_{NO_x} are displayed at the identical positions and time as in figure 5.35. At $z/D = 1$ a small amount of Y_{NO_x} is present and the two peaks of $\dot{\omega}_{NO}$ at $\mathrm{x}/D = 0.5$ and $y/D = \pm 0.5$ are visible in the mean and in the instantaneous plot. Y_{NO_x} increases while moving downstream along the jet trajectory to $z/D = 2$. Still two maxima are present at the lee side of the jet at two symmetric, but separated locations of $x/D = 0.5$ and $y/D = \pm 1$. When moving to $x/D = 3$, the Y_{NO_x} mean increases further. However, at $z/D = 4$ to $z/D = 6$, displayed in figure 5.36, the mean values of Y_{NO_x} do not increase anymore. The intermittent and unsymmetrical distribution caused by the turbulent structures is visible from the instantaneous plots from $z/D = 2$ to $z/D = 6$ in figures 5.36 and 5.37. The mean and instantaneous $Y_{\mathrm{NO_x}}$ show no increase in figure 5.37.

The distribution of $Y_{\mathrm{NO_x}}$ in figure 5.30 is governed by a high combustion temperature and slow dilution by the crossflow. The combustion process is the most important source for $\dot{\omega}_{NO_x}$. It takes place separated from the crossflow which is shielded by the combustion products. The reaction temperature and therefore $\dot{\omega}_{NO}$ can not be significantly reduced. $Y_{\mathrm{NO_x}}$ formed in the flame can only be diluted by a following mixing process. $\mathrm{NO_x}$ is generated in the jet near the location where heat is released. Because $\dot{\omega}_{NO_x}$ depends on temperature, the highest temperature as well as the maximum

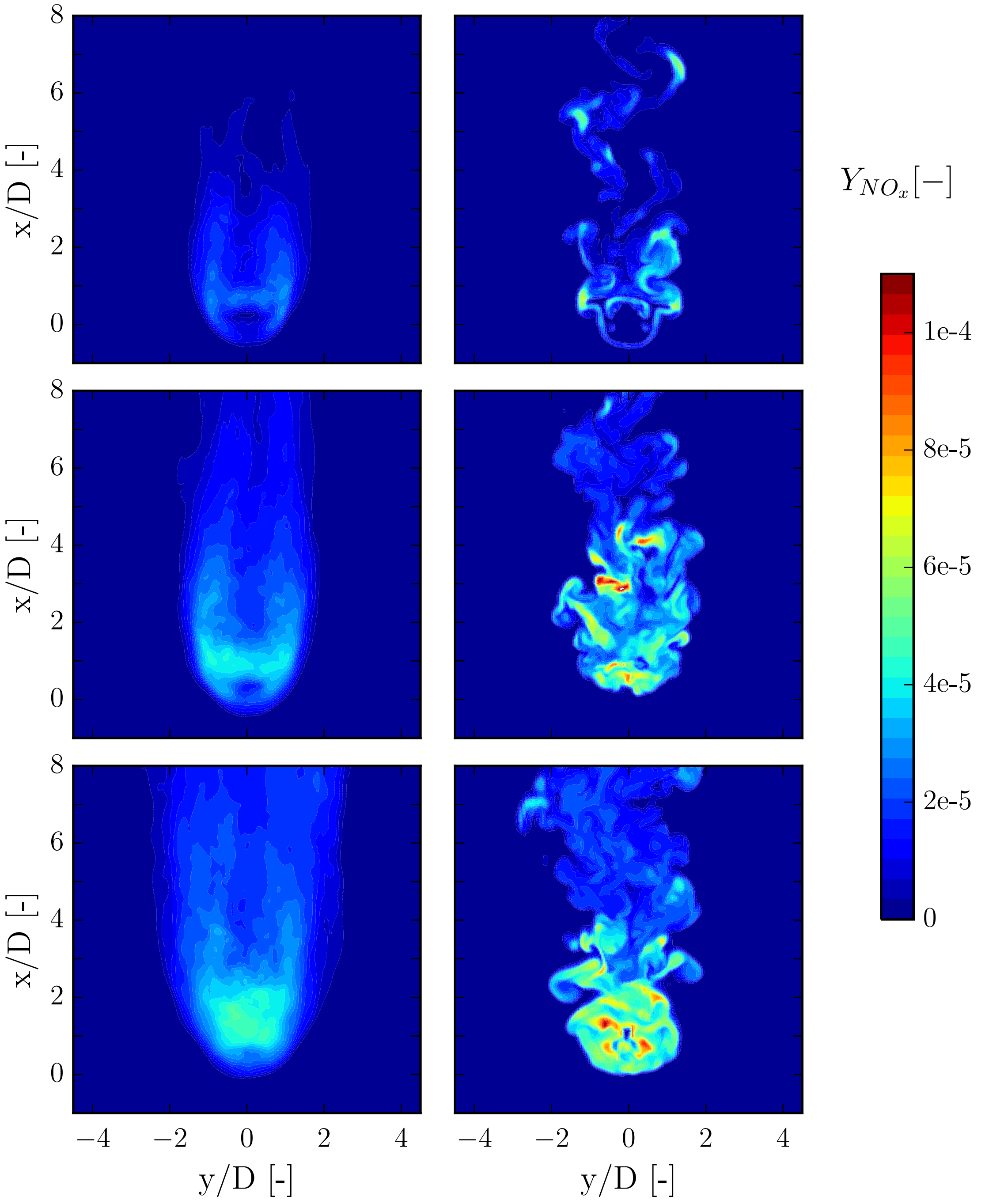

Figure 5.36: Mean (left) and instantaneous (right) $\mathrm{NO_x}$ mass fraction at $z/D = 1$ (first row), $z/D = 2$ (second row) and $z/D = 3$ (third row) for configuration 9.

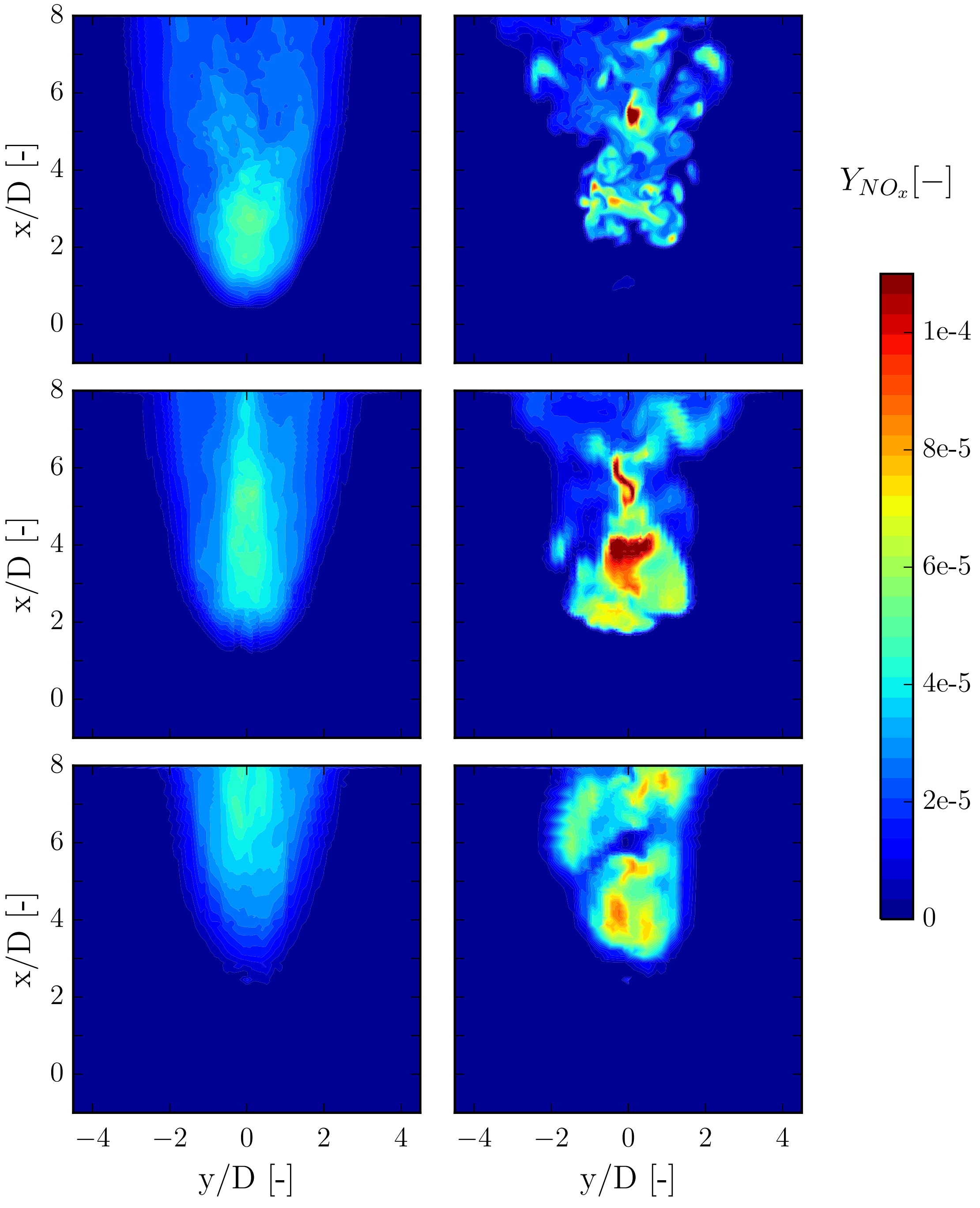

Figure 5.37: Mean (left) and instantaneous (right) NO_x mass fraction at $z/D = 4$ (first row), $z/D = 5$ (second row) and $z/D = 6$ (third row) for configuration 9.

Y_{NO_x} concentration are convected through the domain. The thermal NO_x path further increases Y_{NO_x}. Due to the dominating Zeldovich mechanism, both, temperature and residence time play a role. Temperature is the crucial factor. To reduce Y_{NO_x} $\dot{\omega}_{NO_x}$ must be decreased. This is feasible by lowering the temperature through mixing with colder crossflow. Mixing simultaneously dilutes existing Y_{NO_x}. Mixing takes place because Y_{NO_x} is decreased towards $x/D = 8$ as shown in figure 5.34.

The exponential dependency between Y_{NO_x} and T is not considered by an arithmetical mean of Y_{NO_x} and T. Therefore, computing Y_{NO_x} by a one dimensional reactor simulation and taking the adiabatic flame temperature and residence time of figure 5.32 will not reproduce the values of figure 5.30.

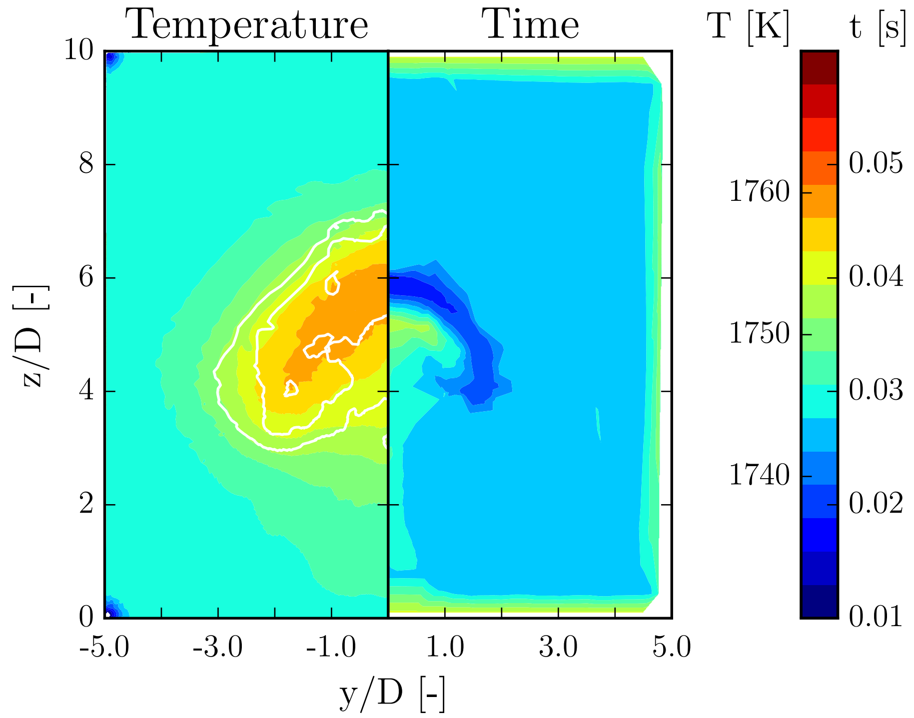

Figure 5.38: Mean temperature and residence time of configuration 10 in a plane normal to the x-direction at $x/D = 8$.

The results of the NO_x model in combination with the TFM differ from those computed with the PaSR model. Configuration 10 predicts a lower NO_x concentration (figure 5.31) than configuration 9 (figure 5.30) with its wider distribution. In analogy to figure 5.32 the distribution of temperature and residence time of configuration 10 is shown in figure 5.38. The isocontours in white color represent NO_x concentrations of 4, 6 and 8 ppm, increasing towards the center of the jet. The difference between the maximum simulated temperature and the measured temperature is below 20 K. This affects $\dot{\omega}_{NO_x}$ which is reduced in comparison to configuration 9. Consequently, the deviation between simulated and measured NO_x concentration is reduced. Further, the two concentration maxima are not at the maximum mean temperature of 1760 K. They are found at slightly lower temperatures of 1755 K. The maximum values are additionally reduced by better mixing, indicated by a more evenly NO_x distribution in figure 5.31 than in figure 5.30.

The spread of the mean residence times of configuration 10 is smaller than in configuration 9. The residence times are mainly influenced by the velocity field. The small temperature difference has negligible effect and does not alter the residence time. The short residence times on the windward side are above a layer of long residence time which represents the lee side of the jet. The influence of the residence time on the mean NO_x mass fraction is visible in figure 5.38. Regions at a residence time of 15 ms and 40 ms result in a NO_x concentration of 7 ppm and 6 ppm respectively. This is contrary to the expectations, where shorter residence times results in lower NO_x concentration. The reason is the combination of higher temperature with shorter residence time. Finally, temperature dominates the NO_x formation.

In figure 5.39, the time mean $\dot{\omega}_{NO_x}$ distribution in the symmetry plane is shown on the left whereas instantaneous $\dot{\omega}_{NO_x}$ is displayed on the right. The zone with peak values in the mean $\dot{\omega}_{NO_x}$ distribution is wider than in configuration 9. At the same time, the zone with high source term is shifted downstream along the jet trajectory. This can also be seen in the plots of the instantaneous values. The source term within a radius of 2 D of the jet exit shows the same maximum values as in configuration 9 but only in thin broken fronts. Moving downstream, similar values of $\dot{\omega}_{NO_x}$ are present, but in a large area formed by the thickened flame front. Similar to configuration 9, the regions of high $\dot{\omega}_{NO_x}$ values are closely related to the flame front. After the combustion process, the source term is reduced by 1/4 to 1/3 of the values within the flame. The instantaneous contours reveal that the source

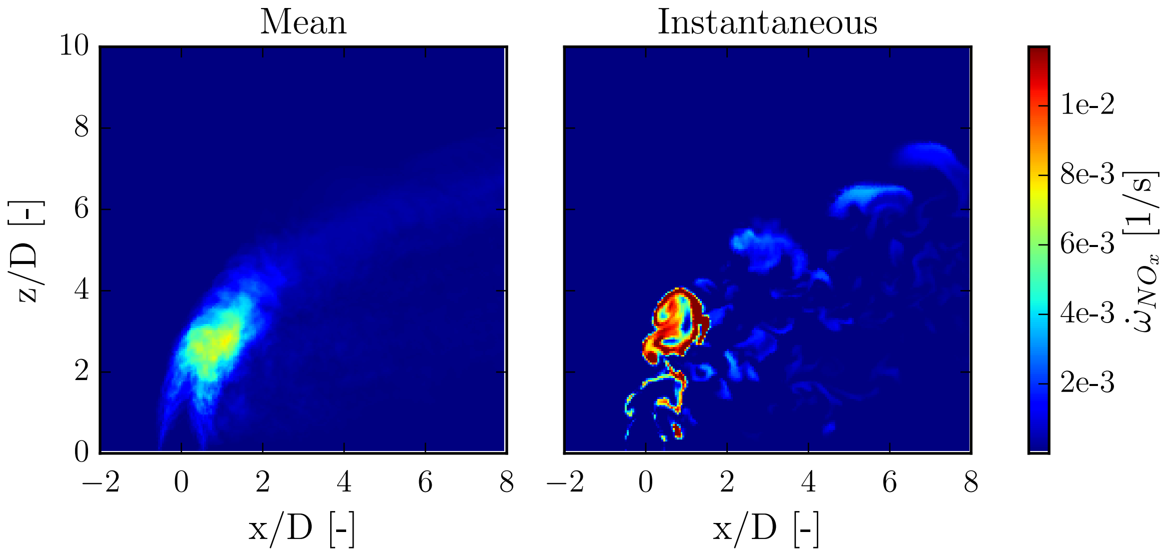

Figure 5.39: Mean (left) and instantaneous (right) reaction rates $\dot{\omega}_{NO_x}$ on the symmetry plane of configuration 10.

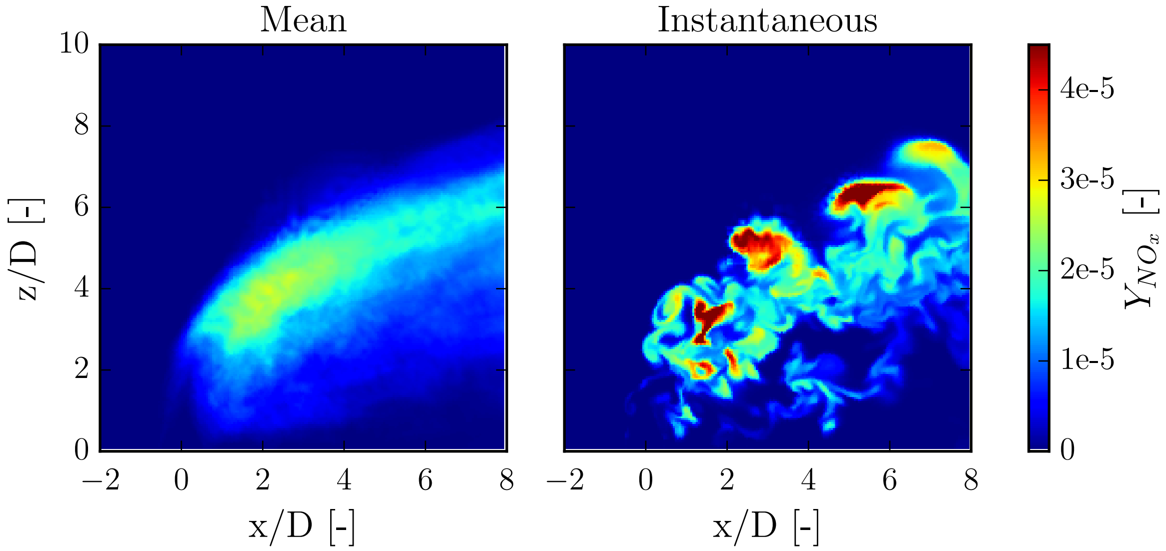

Figure 5.40: Mean (left) and instantaneous (right) NO_x mass fraction on the symmetry plane for configuration 10.

term is continuous in time and the regions with high $\dot{\omega}_{NO_x}$ are convected through the domain. This behavior results in oscillations of high and low $\dot{\omega}_{NO_x}$ values and NO_x concentrations. The contours of Y_{NO_x} are plotted in figure 5.40. The instantaneous values show the intermittent character of the Y_{NO_x} distribution. As the maximum values are present close to the flame front, the source terms in the post flame zone do not increase Y_{NO_x}. In parallel dilution takes place and Y_{NO_x} is decreased in downstream direction as can be clearly seen in the plots of the mean values. The formation of $\mathrm{NO_x}$ takes place within the shear layer and not within the jet. Thus, the large scale coherent structures lead to wide zones with $\mathrm{NO_x}$. As a result, at the lee side of the jet a larger area is covered by $\mathrm{NO_x}$ in configuration 9 than in configuration 10 (see figure 5.40 and figure 5.35).

Switching from the symmetry plane to a view along the z-axis, figure 5.41 displays the mean values $\dot{\omega}_{NO_x}$ on the left and the instantaneous values on the right. The instantaneous values in figure 5.41 are generated from the identical time step than figures 5.39 and 5.40. Therefore, conclusions drawn from one of these figures are also valid for the others. The first row is located at $z/D = 1$, the second at $z/D = 2$ and the third at $z/D = 3$. At $z/D = 1$ the mean values have the same behavior than those of configuration 9, predicting two symmetrical peaks at $x/D = 0.5$ and $y/D = \pm 0.5$. But the instantaneous state does not show this symmetry, although the maximum values coincide with the location of the maximum mean values. At $z/D = 1$ $\dot{\omega}_{NO_x}$ forms an almost closed reaction front characterized by $\dot{\omega}_{NO_x} > 0.011/s$ which is comparable to configuration 9. But when moving downstream to $z/D = 2$ and further, the reaction front is fragmented into separate zones. The zones spread over a larger region than in configuration 9. This is also true for the corresponding mean contour. The separated and distributed zones with high $\dot{\omega}_{NO_x}$ are explained by a different behavior of the heat release, which has been analyzed in section 5.3.3. Similar to $z/D = 2$, at $z/D = 3$, the mean values are almost identical to the values from configuration 9 at the same position. The two zones where maximum values are found merge to one peak value zone. But both configurations differ in their geometrical extension. Configuration 10 predicts a larger area of $\dot{\omega}_{NO_x}$ than configuration 9.

The resulting distribution of Y_{NO_x} is displayed in figure 5.42. Mean value of Y_{NO_x} is displayed in the left column and instantaneous Y_{NO_x} in the right. Mean and instantaneous Y_{NO_x} in the first row are from $z/D = 1$, in the

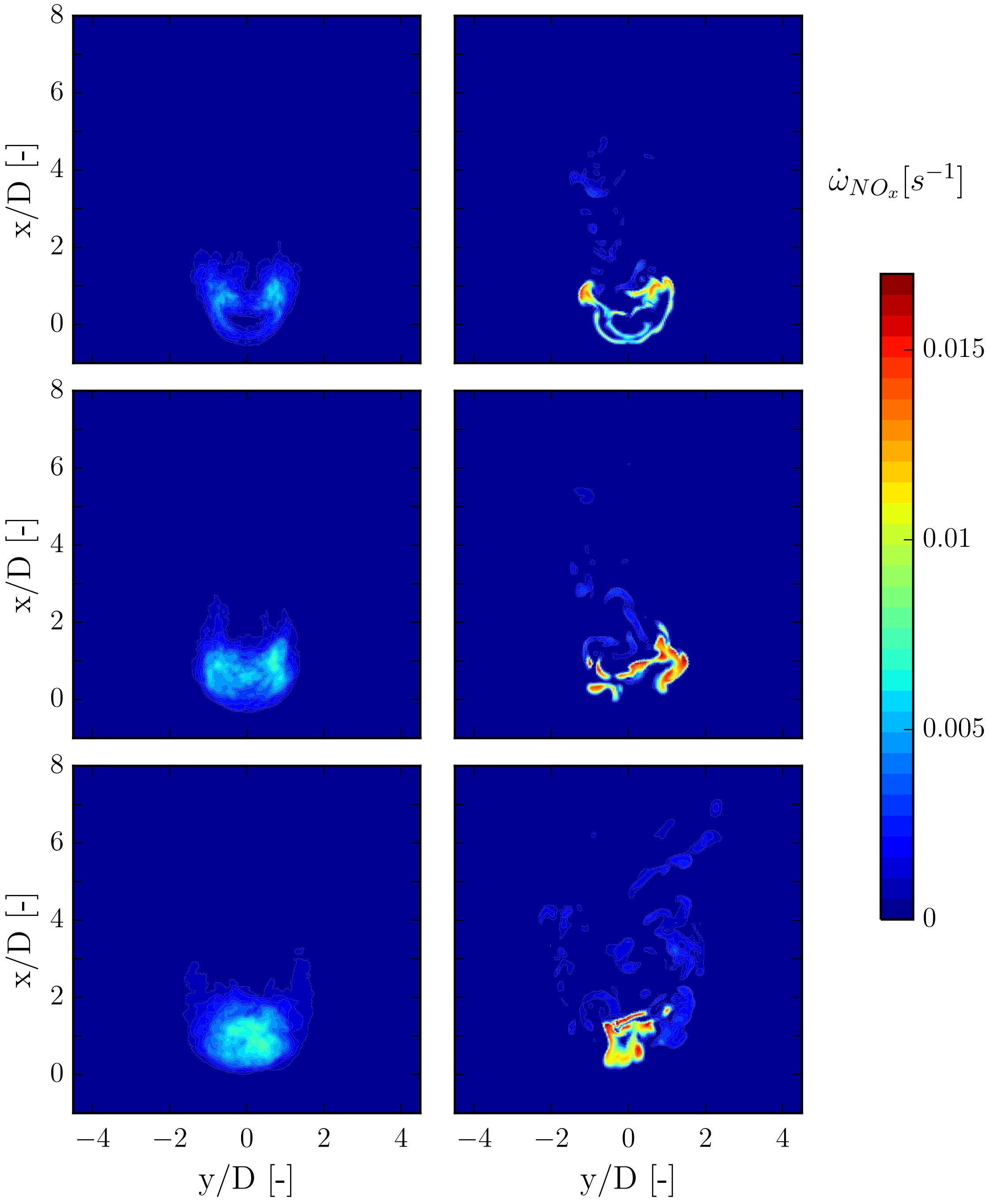

Figure 5.41: Mean (left) and instantaneous (right) reaction rates $\dot{\omega}_{NO}$ at $z/D = 1$ (first row), $z/D = 2$ (second row) and $z/D = 3$ (third row) for configuration 10.

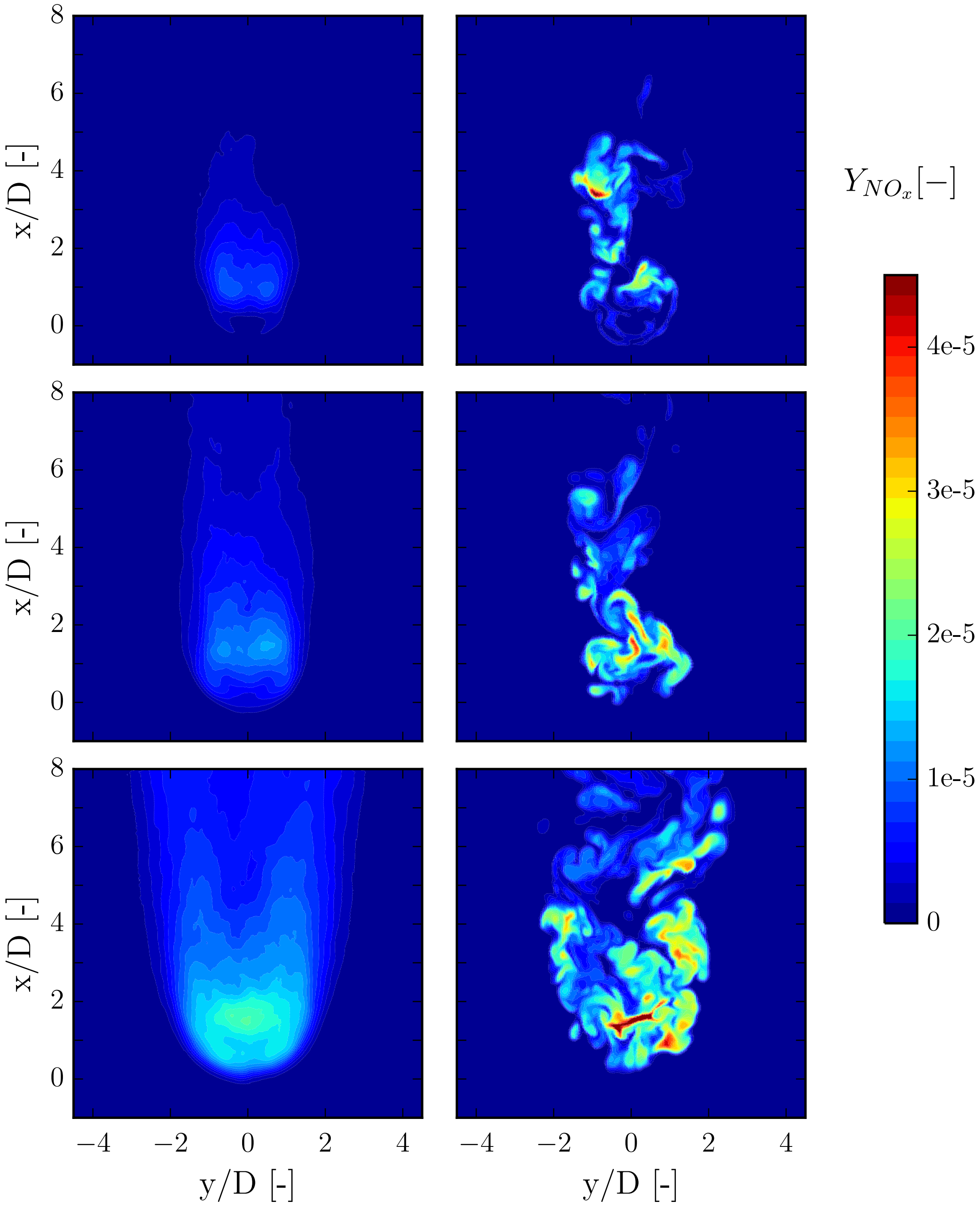

Figure 5.42: Mean (left) and instantaneous (right) NO_x mass fraction at $z/D = 1$ (first row), $z/D = 2$ (second row) and $z/D = 3$ (third row) for configuration 10.

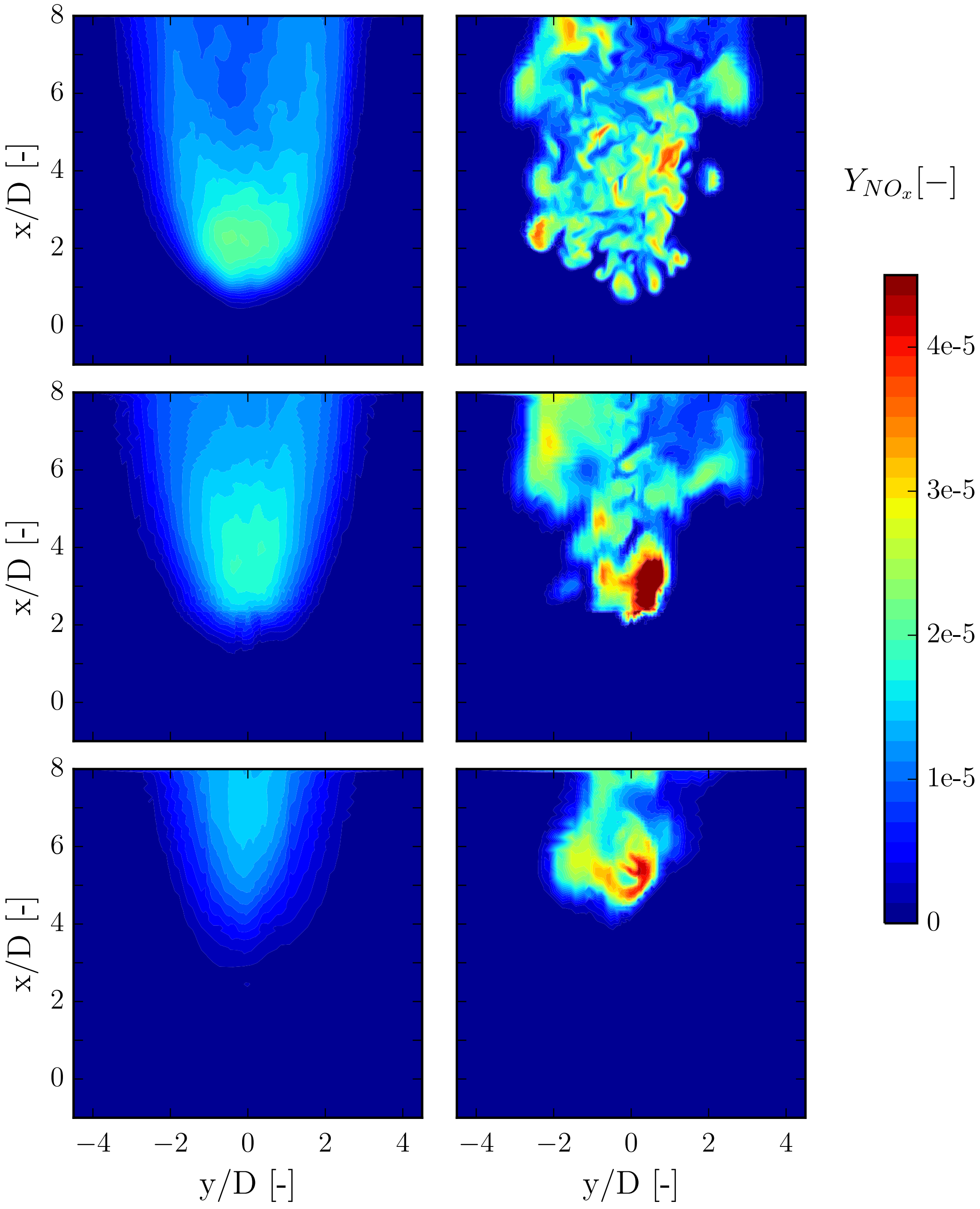

Figure 5.43: Mean (left) and instantaneous (right) NO_x mass fraction at $z/D = 4$ (first row), $z/D = 5$ (second row) and $z/D = 6$ (third row) for configuration 10.

second row from $z/D = 2$ and in the third row from $z/D = 3$. The plots reveal the same differences of $\dot{\omega}_{NO_x}$ as visible in figure 5.41. Additionally, mean Y_{NO_x} is lower than mean Y_{NO_x} of configuration 9. Moving along the z-axis, figure 5.43 shows mean and instantaneous Y_{NO_x} values at $z/D = 4$ in the first row, at $z/D = 5$ in the second row and at $z/D = 6$ in the third row. Further differences can be identified when comparing the mean values of figure 5.37 to configuration 9. Mean Y_{NO_x} at $z/D = 6$ of configuration 10 extends from $x/D = 3$ to $x/D = 8$ whereas zones with $\mathrm{NO_x}$ of configuration 9 starts at $x/D = 2$. A similar tendency is observed for the contours at $z/D = 5$. This is the result of the lower penetration depth of the jet of configuration 10 as Y_{NO_x} is only present in the jet. In contrast to configuration 9 where Y_{NO_x} concentrates next to the symmetry plane at $x/D = 0$ in the center of the jet, Y_{NO_x} is diluted in downstream direction in configuration 10. The dilution process is slowest within the center of the counter rotating vortex pair, because a smaller amount of crossflow material is introduced. This explains the high peak values seen in figure 5.31.

In summary, $\mathrm{NO_x}$ is more evenly distributed in configuration 10. Still, a higher Y_{NO_x} concentration is present in the center of the jet. The TFM predicts lower temperatures which result in an overall lower $\mathrm{NO_x}$ generation. Furthermore, the location of the zones with high $\dot{\omega}_{NO_x}$ in space is important. Because the formation of $\mathrm{NO_x}$ is not spatially concentrated as much as the formation of $\mathrm{NO_x}$ in configuration 9 and takes place within the shear layer, the mixing process is stronger in comparison with configuration 9.

5.5 Scaling to Engine Conditions

All results presented so far were for atmospheric pressure, although the final goal is the development of an LES which can be applied for engine conditions, which are not accessible in the experiment. The reason for the focus of the code development at ambient pressure was the availability of validation data.

As presented in section 4, geometrical dimension and mean velocity of the validation experiment were scaled to generate a representative combustion regime at atmospheric conditions. The data for the engine conditions at

$p = 20$ bar are listed in table 5.1. The dimension of the computational domain under engine conditions is scaled to a side length of 125 mm according the scaling of the jet diameter. The momentum ratio can be calculated from table 5.1 and results in $J = 6$. Because of limited computational capacity available only the PaSR model is chosen to compute the combustion process. The TFM would also be feasible, but as shown in the results from configuration 9 and 10, the PaSR model delivers more conservative results. The results concerning NO$_\mathrm{x}$ concentrations resulting from the PaSR model therefore deliver a better basis for a detailed investigation. The mean values presented hereafter are extracted from computations over 13 residence times, calculated from u_{cross} and the length of the domain of 5 D.

Variable	Φ	D	p	T	u
Jet	0.66	$0.0254\,m$	$20\,bar$	$670\,K$	$145\,m/s$
Crossflow	0.5	–	$20\,bar$	$1746\,K$	$98\,m/s$

Table 5.1: Boundary values of the engine configuration.

The mean and instant velocity plots in figure 5.44 are generated to evaluate the simulation performed at engine conditions. The presented velocity magnitude is computed from the x- and z-component. These components are also used to compute the streamlines printed in white in the plots of mean and instantaneous fields. The mean values are very similar to configuration 9 at atmospheric pressure, disregarding the absolute velocity magnitude. A difference is the expansion of the jet, displayed in figure 5.44 by the larger velocity of the jet close to the jet exit. The jet expansion into the crossflow is caused by the shear layer vortices which have their origin at the same location. The presence of the shear layer vortices can be seen in the instantaneous velocity field. On the windward side of the jet three vortices are computed. They are marked by white arrows on the streamlines pointing perpendicular to the jet. These vortices entrain crossflow material into the jet and transport jet material into the crossflow. During this process a momentum exchange takes place and accelerates the crossflow material, while the jet material is slowed down. The size of the expansion of the jet

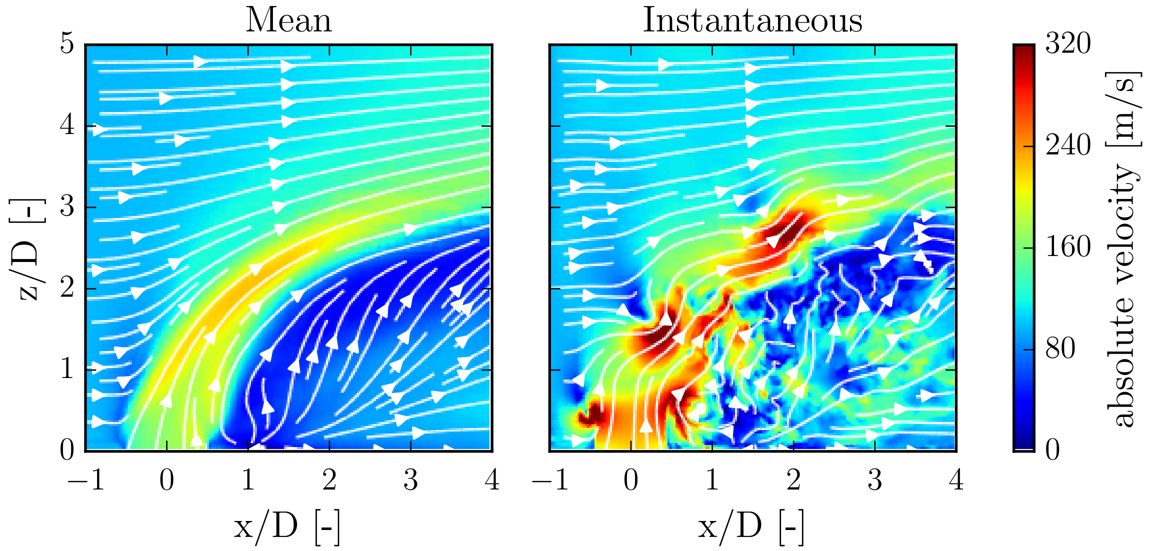

Figure 5.44: Mean (left) and instantaneous (right) velocity magnitude from engine configuration at $y/D = 0$. In white stream lines computed from the displayed velocity.

is controlled by the vortex size. This size is much larger than observed in configuration 9 or 10 leading to more intense exchange between jet and crossflow.

The corresponding temperature distribution generated by the PaSR model is shown by figure 5.45. The thin zone of higher temperature of the mean values indicates that the combustion process in this configuration is much faster than mixing of jet and crossflow. This is confirmed by the instantaneous temperature on the right of figure 5.45. The location of the flame is visualized by two black contours, representing 10 % of $\dot{\omega}_{NO}$. The onset of reaction is located in between these two lines. The jet material consumed by the flame is not diluted by crossflow material because the reactants have a uniform temperature. The combustion temperature is close to the adiabatic flame temperature but never exceeds it.

5.5.1 Analysis of NO_x Formation

In figure 5.46, the mean and instantaneous NO_x values are displayed at the exit of the domain at $x/D = 4$. The plot of the mean values reveals a kidney

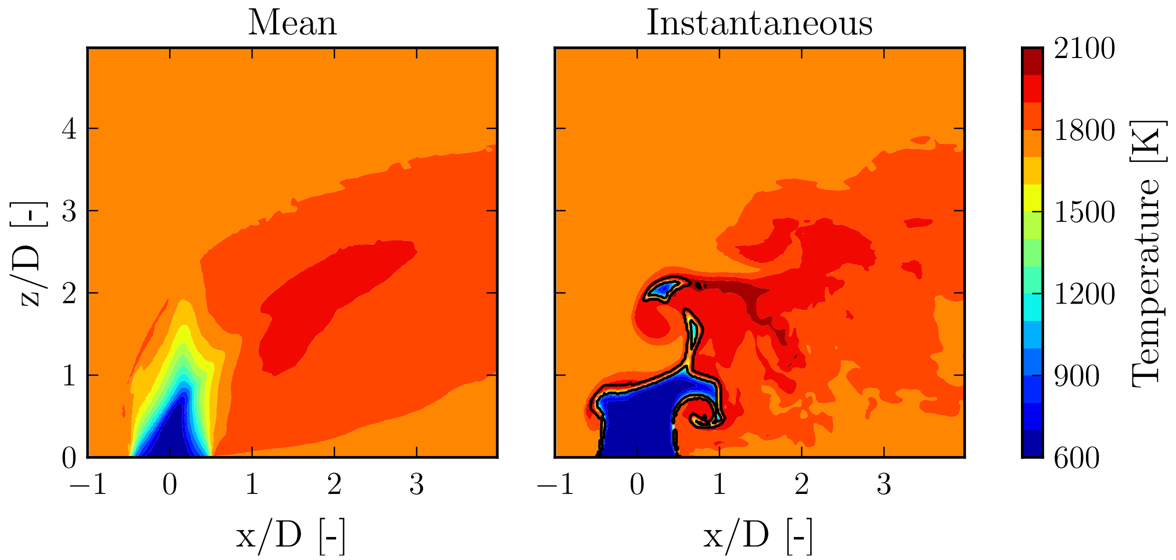

Figure 5.45: Mean (left) and instantaneous (right) temperature from engine configuration at $y/D = 0$. In black, an iso-contour representing 1/10 of the maximum heat release rate.

shaped distribution of NO_x. A NO_x concentration of 12 ppm is predicted at a comparable residence time from a 1-D simulation using GRI3.0 and the gas composition of the jet. This theoretical value is larger than any concentration shown in figure 5.46. This is because of the fast mixing process of jet and crossflow. Both peak values in the mean field are not located within the symmetry plane at $y/D = 0$, but are found in the centers of the counter rotating vortex pair. The instantaneous field also shows a higher concentration within the counter rotating vortex pair, and even higher concentrations on the lee side of the jet.

The reaction source term $\dot{\omega}_{NO}$ in the symmetry plane is displayed in figure 5.47. From the mean values can be concluded that the flame root is not stationary and always closely located next to the jet exit. The instantaneous values give more insight: The regions of highest source terms show the flame front, which is corrugated by the vortices. At the lee side of the jet, the flame follows the vortex against the main flow direction. When viewing along the x-axis as displayed in figure 5.49, a second flame front can be observed. At $x/D = 0.5$ and $z/D = 2$ a completely separated pocket of

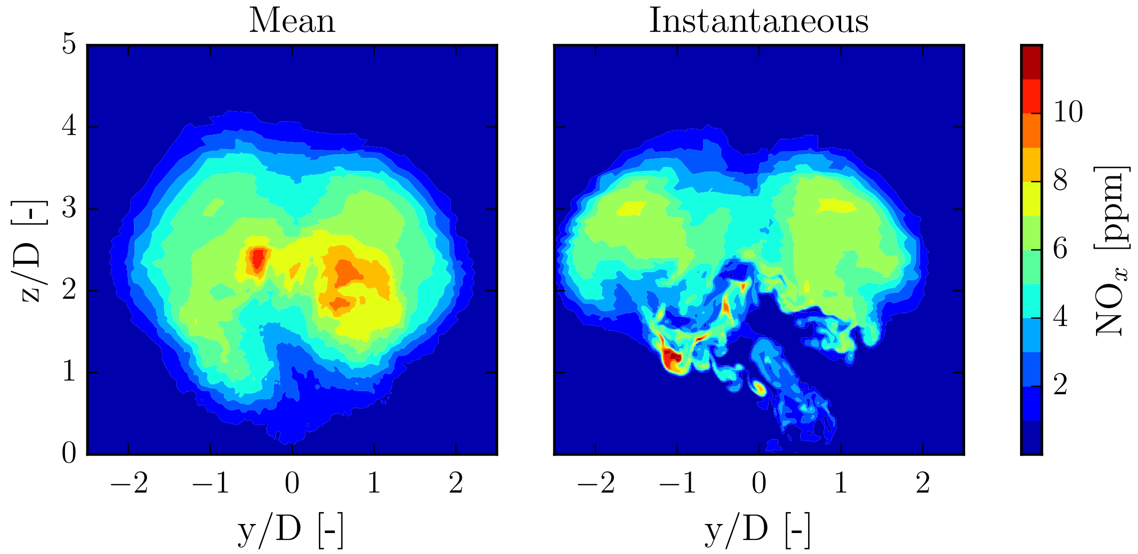

Figure 5.46: Mean (left) and instantaneous (right) $\mathrm{NO_x}$ distribution at $x/D = 4$ for engine conditions.

unburned gas is surrounded by a flame. Following the jet downstream, the source term, based on the Zeldovich mechanism, can be directly connected to the temperature field from figure 5.45. In the instantaneous temperature distribution in figure 5.45 a decrease of temperature in downstream direction is observed. Therefore $\dot{\omega}_{NO}$ also drops, because it is exponentially dependent on temperature. It can be concluded, that due to mixing not only produced $\mathrm{NO_x}$ is diluted but also the generation itself is reduced.

The Y_{NO_x} plots which correspond to figure 5.47 are displayed in figure 5.48. The mean Y_{NO_x} values seem to significantly increase along the jet, but that does not directly imply that the $\mathrm{NO_x}$ is formed in the symmetry plane: $\mathrm{NO_x}$ is transported by the counter rotating vortex pair into the symmetry plane after it has been generated in other areas. From the development of Y_{NO_x} in figure 5.46 can be concluded that a even higher mean Y_{NO_x} can be found in the counter rotating vortices.

In figure 5.49 and figure 5.50 mean and instantaneous contours of $\dot{\omega}_{NO_x}$ are shown at $z/D = [0.5, 1.0, 1.5, 2.0, 2.5, 3.0]$ to complete the picture of the formation process of $\mathrm{NO_x}$. In figure 5.47, high instantaneous $\dot{\omega}_{NO_x}$ values indicate the flame position. At $z/D = 0.5$ two flame fronts seem to exist. But

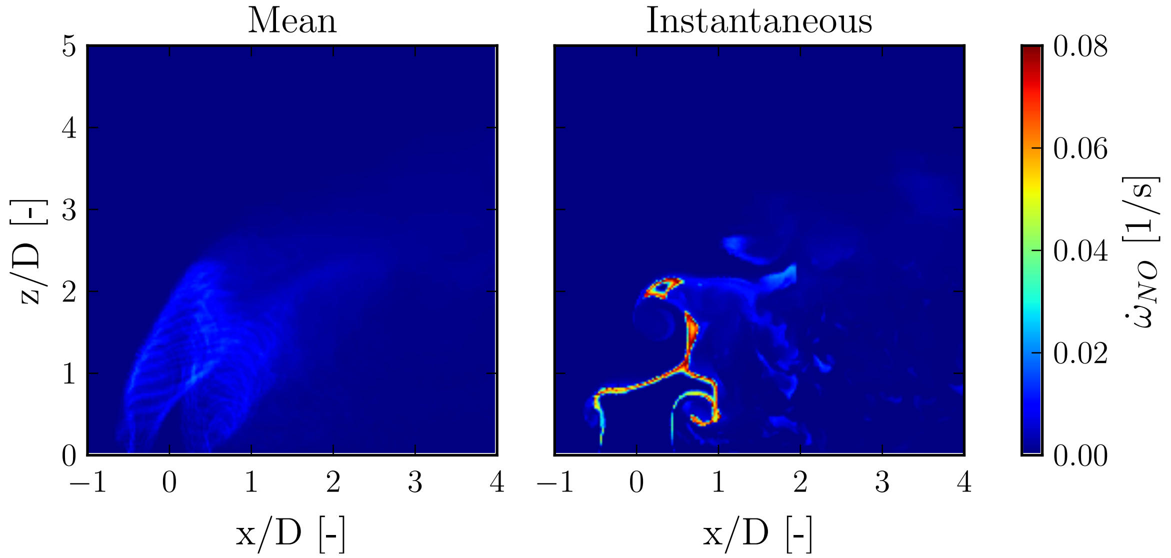

Figure 5.47: Mean (left) and instantaneous (right) reaction rates $\dot{\omega}_{NO}$ at $y/D = 0$ for engine conditions.

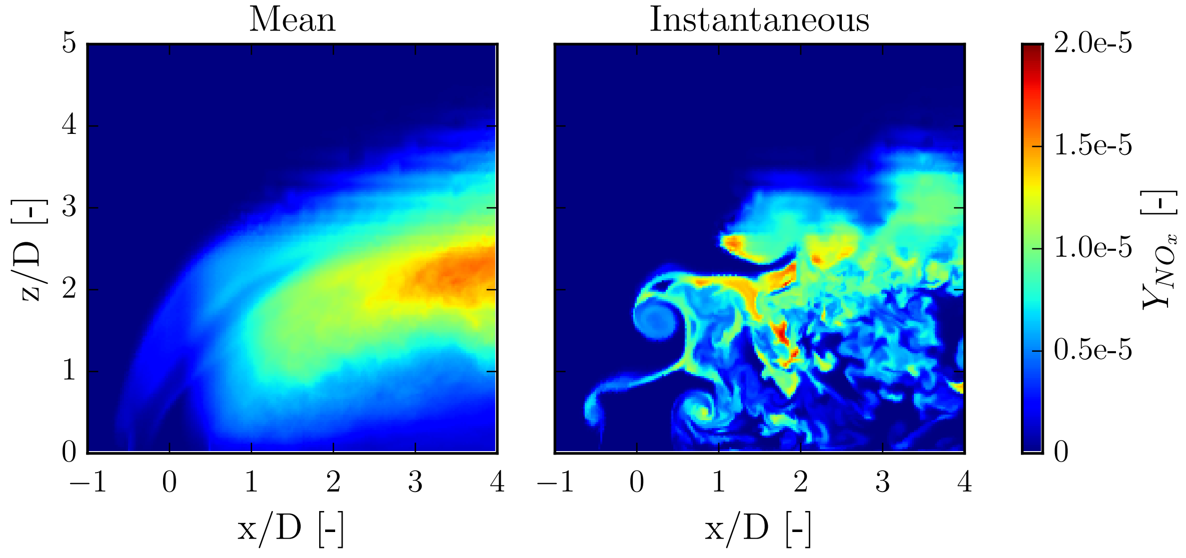

Figure 5.48: Mean (left) and instantaneous (right) NO_x mass fraction at $y/D = 0$ for engine conditions.

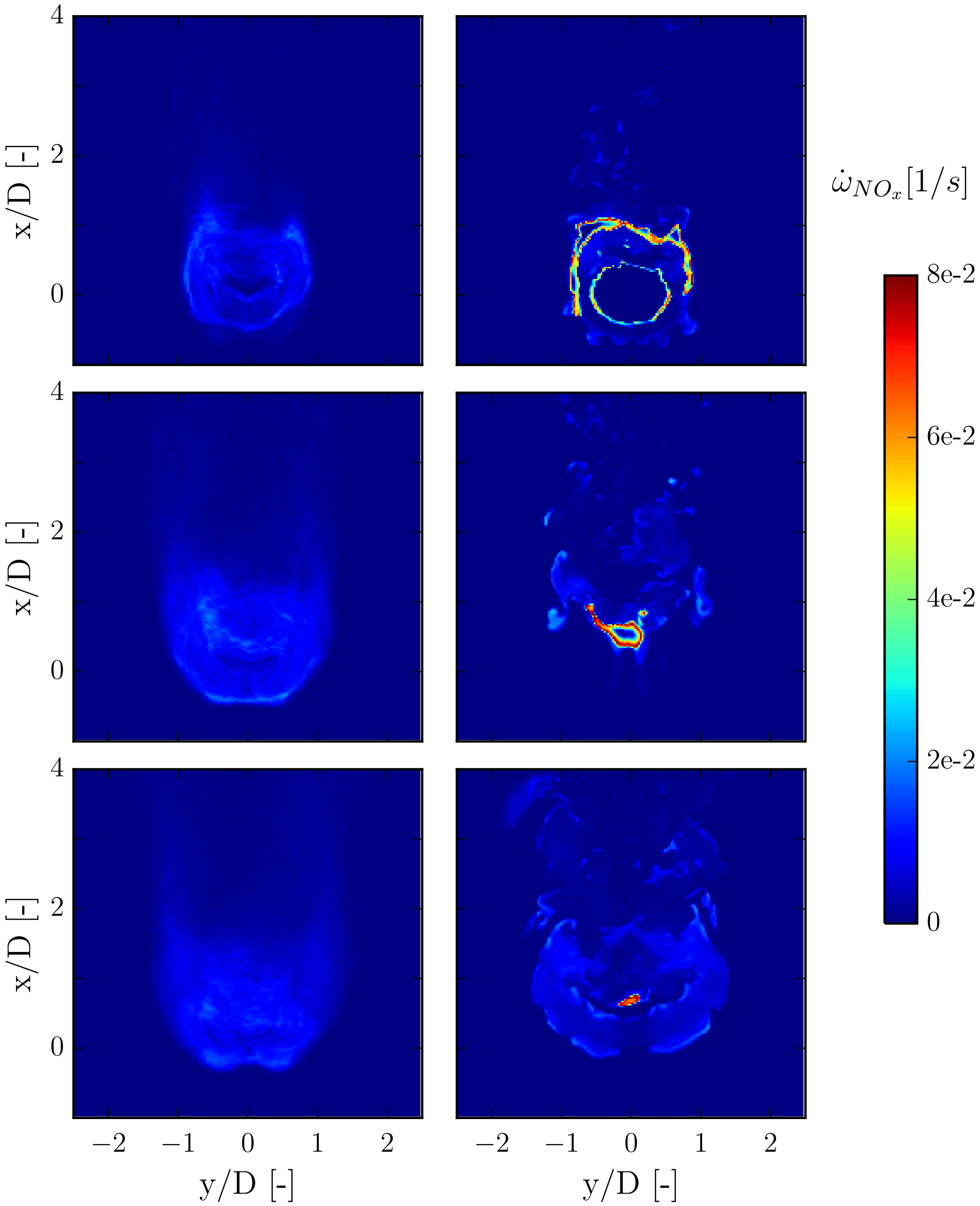

Figure 5.49: Mean (left) and instantaneous (right) reaction rates $\dot{\omega}_{NO}$ at $z/D = 0.5$ (first row), $z/D = 1$ (second row) and $z/D = 1.5$ (third row) for engine conditions.

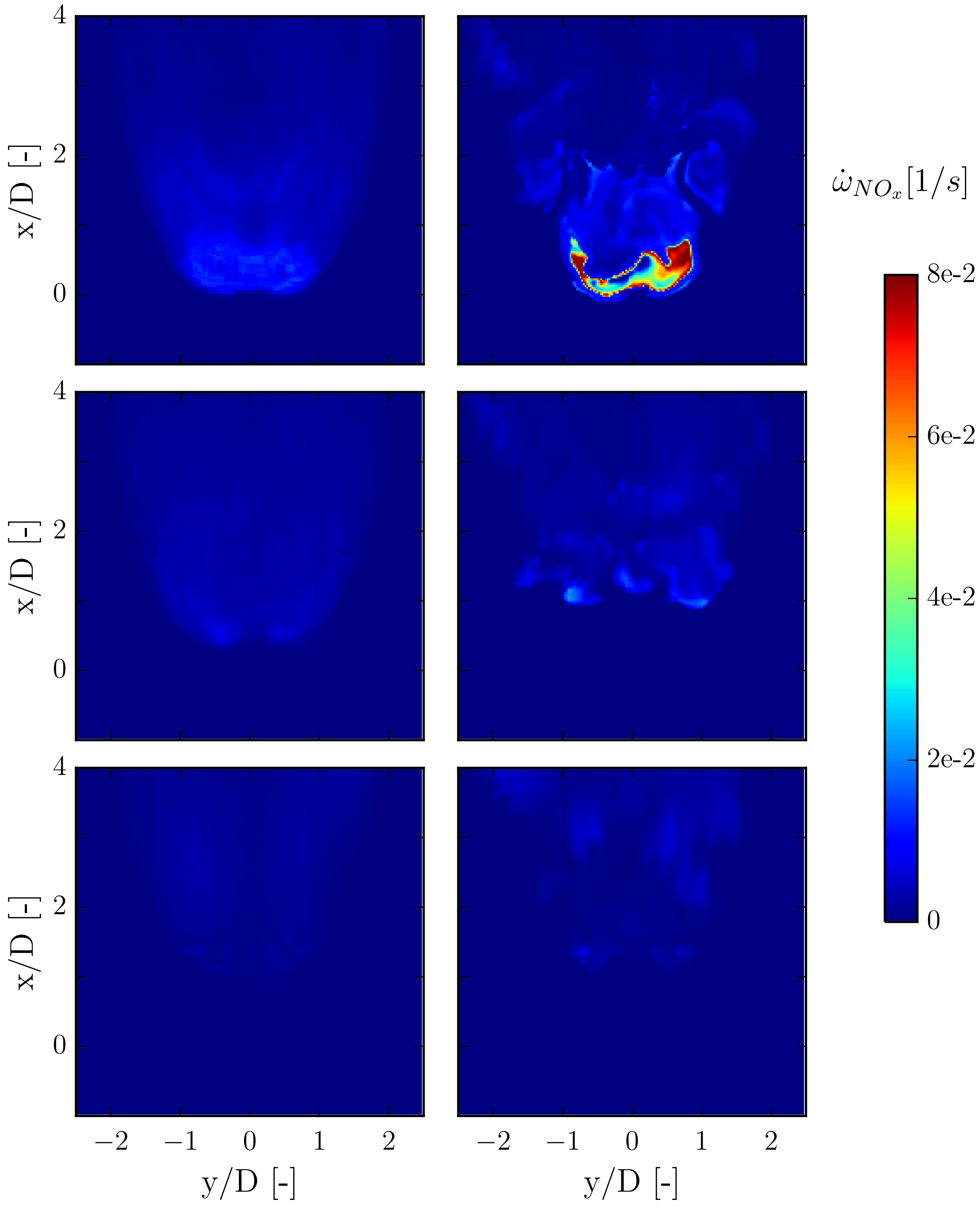

Figure 5.50: Mean (left) and instantaneous (right) reaction rates $\dot{\omega}_{NO}$ at $z/D = 2$ (first row), $z/D = 2.5$ (second row) and $z/D = 3$ (third row) for engine conditions.

they are connected to each other as can be concluded from figure 5.47. The flame front follows the ring like vortex, similar to a torus, which surrounds the jet completely. Because the plane $z/D = 0.5$ is not perpendicular to the torus axis, only a segment is captured. The instantaneous values at $z/D = 1$, $z/D = 1.5$ and $z/D = 2$ show only one closed flame front. Although $\dot{\omega}_{NO_x}$ is largest within the flame front, the source term reaches more than 1/4 of the maximum value in the subsequent regions which, therefore, must not be neglected. The mean $\dot{\omega}_{NO_x}$ fields at $z/D = 1$, $z/D = 1.5$ and $z/D = 2$ support the observations from the instantaneous fields. The mean values show elevated $\dot{\omega}_{NO_x}$ values at the same place where the counter rotating vortices are located.

The distribution of Y_{NO_x} on planes perpendicular to the z-axis at the positions $z/D = [0.5, 1.0, 1.5, 2.0, 2.5, 3.0]$ is displayed in figures 5.51 and 5.52 for mean and instantaneous values. The mean contours in figure 5.51 show the highest concentration of Y_{NO_x} within the centers of the vortex pair, reflecting $\dot{\omega}_{NO_x}$ from figure 5.49. For $z/D = 2$ and $z/D = 3$ the maximum values are no longer found in two symmetrical zones. Still, the influence of the counter rotating vortex pair is visible but on the windward side of the jet. Altogether, the mean values from $z/D = 0.5$ to $z/D = 3$ show a remarkably low Y_{NO_x} concentrations on the windward side of the jet. This is not observed in configuration 9 and 10, still showing larger values on the lee side of the jet. Looking on the instantaneous values, for example at $z/D = 1.5$ it can be observed, that on the windward side of the jet the instantaneously formed Y_{NO_x} immediately leaves the symmetry plane. A similar observation can be made for all positions. The shear stress generated between the jet and the crossflow immediately pushes NO_x sidewards. Therefore, the transport in direction of the jet trajectory is low and Y_{NO} can not accumulate due to the sidewards motion and the transport to the lee side of the jet.

Furthermore, a fragmented Y_{NO} distribution is observed for the instantaneous values in figures 5.51 and 5.52, where hardly any coherent structure can be identified.

When comparing the absolute NO_x concentration for the atmospheric and the pressurized configuration significant lower NO_x values are computed for the engine conditions than for configuration 9. Comparing figure 5.48 and

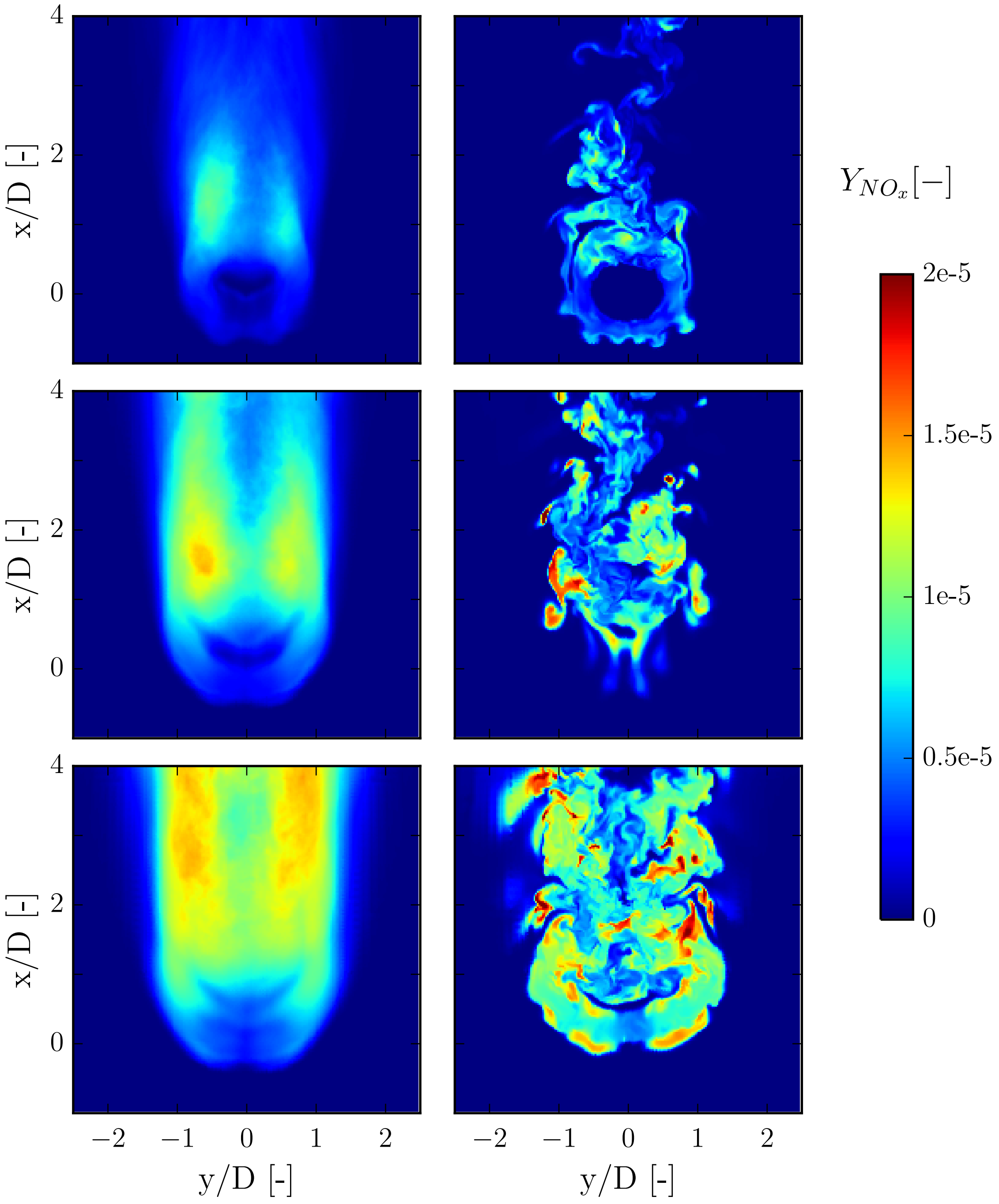

Figure 5.51: Mean (left) and instantaneous (right) NO_x mass fraction at $z/D = 0.5$ (first row), $z/D = 1.0$ (second row) and $z/D = 1.5$ (third row) for engine conditions.

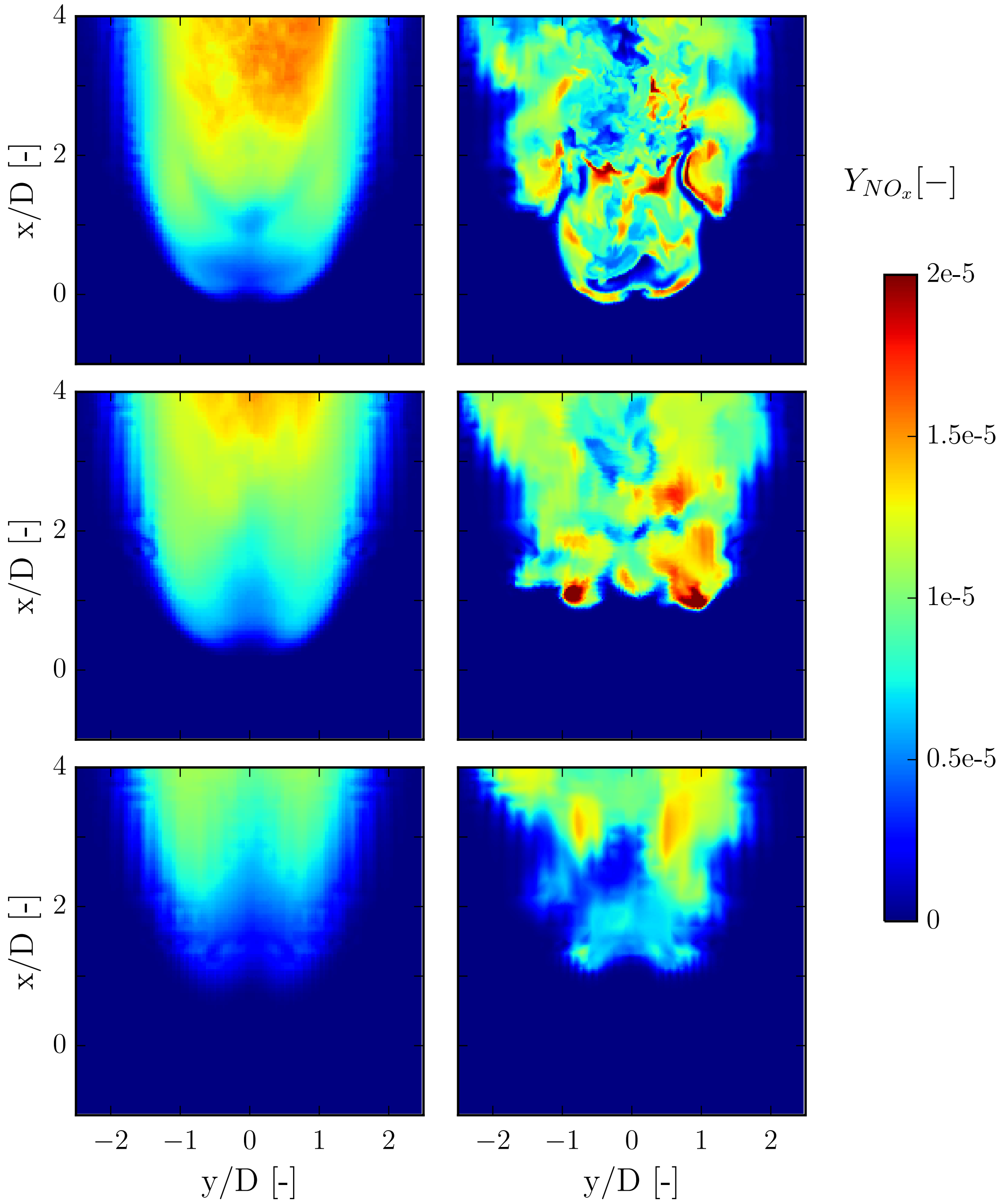

Figure 5.52: Mean (left) and instantaneous (right) NO_x mass fraction at $z/D = 2$ (first row), $z/D = 2.5$ (second row) and $z/D = 3$ (third row) for engine conditions.

figure 5.34 a decrease of the peak value from $Y_{NO} = 4.3 \times 10^{-5}$ by a factor of 2.7 to $Y_{NO} = 1.6 \times 10^{-5}$ is visible for the engine configuration. Not visible from these plots is the mean residence time, which decreases one order of magnitude from 0.02 s to 0.002 s. Assuming a mean temperature of 1900 K in both configurations the shorter residence time can drop by a factor of 2 of the $\mathrm{NO_x}$ concentration. The scaling based on the Da_{τ} therefore is not fully sufficient for an appropriate scaling. The obvious reason for this failure can be found in the temperature fluctuations in the jet in crossflow, which makes it difficult to assume the correct temperature for the scaling calculation.

In summary, it can be concluded that after validation at atmospheric conditions, the pressurized case at engine conditions is successfully computed. The predicted temperatures are in good agreement with theory, as the adiabatic flame temperature is correctly calculated and not exceeded. The calculated Y_{NO} is in accordance with theory and does not exceed the theoretical limit. Some differences of the test cases have been figured out: The higher the velocities the larger are the coherent structures which significantly alter the flame front. These coherent structures extend the jet width and simultaneously the reaction zone area right at the jet exit. On the windward side of the jet, the high stress within the shear layer continuously generates vortices, which fragments the front of the jet. The continuous transport towards the lee side of the jet and the intermittent flame front inhibit an accumulation of products along the front within the symmetry plane. This results in a region of lower Y_{NO} in the jet in crossflow configuration at the windward side of the jet. The mixing decreases the temperature and therefore $\dot{\omega}_{NO}$ in these regions. Y_{NO} is not only diluted by jet material but also the formation process is weaker due to a reduction of $\dot{\omega}_{NO}$.

5.5.2 Influence of Flame Lift-off on $\mathrm{NO_x}$ Formation

Atmospheric experiments performed by Kolb et al. [40], [41] indicate that flame lift-off must be expected at engine conditions. The finite rate chemistry models PaSR and TFM both use reduced chemistry. As described in section 2.3 reduced chemistry fails when predicting the ignition delay time because they do not account for all intermediate species. Generally, reduced chemistry underestimates the ignition delay time. Therefore no significant flame lift is observed under engine conditions in the simulation. Using a more detailed chemistry scheme to overcome the wrong ignition delay times is not applicable because of prohibitive computational costs. However, to investigate the influence of flame lift-off on $\mathrm{NO_x}$ concentrations, the lift-off correlation found by Kolb [40] is combined with the source term in the species and energy conservation equation. The combustion process can only take place, if the lift-off criteria

$$LO = 9.7\left(Ka_{mix}/Da_t\right)^{0.61} = 9.7\frac{u'^{2.5}a(f)^{0.5}\tau_{ign}}{D^{1.5}s_l(f)^2} \tag{5.2}$$

is fulfilled. To achieve this, the reaction source term is multiplied by a lift-off variable. This variable is equal to zero as long as the lift-off height (LO) is not reached. When the distance to the jet exit (origin of the coordinate system) exceeds the lift-off height, the lift-off variable switches to one and reaction can take place. The lift-off variable has a smooth gradient between 0 for the non reacting zone and 1 for the zone, were reaction is possible. This is necessary because of stability of the computational code. Using equation 5.2 the expected lift-off is calculated to 0.66 D, when the ignition delay τ_{ign} is calculated using GRI3.0 for the most reactive mixture fraction between jet and crossflow and $a(f)$ is the thermal diffusivity as proposed by Kolb [40].

The engine configuration (section 5.5.1) is recomputed using the PaSR model in combination with the lift-off criteria. The resulting mean and instantaneous velocity fields at the symmetry plane are shown in figure 5.53. The instantaneous velocity shows a similar behavior as in figure 5.44 without flame lift-off. On the lee side of the jet, irregular turbulent structures are present whereas on the windward side the shear layer vortices are revealed. Small differences are observed comparing the mean velocities. The penetration depth is lower and the maximum velocities are smaller if lift-off takes place. For the explanation of this behavior figure 5.54 is employed, where the mean and instantaneous temperatures are shown at the symmetry plane. The combustion process is shifted downstream for flame lift-off. Therefore, less momentum in z-direction is generated and the penetration depth is reduced. At the same time, the velocity maxima are reduced. The velocity decrease due to momentum exchange has already progressed when

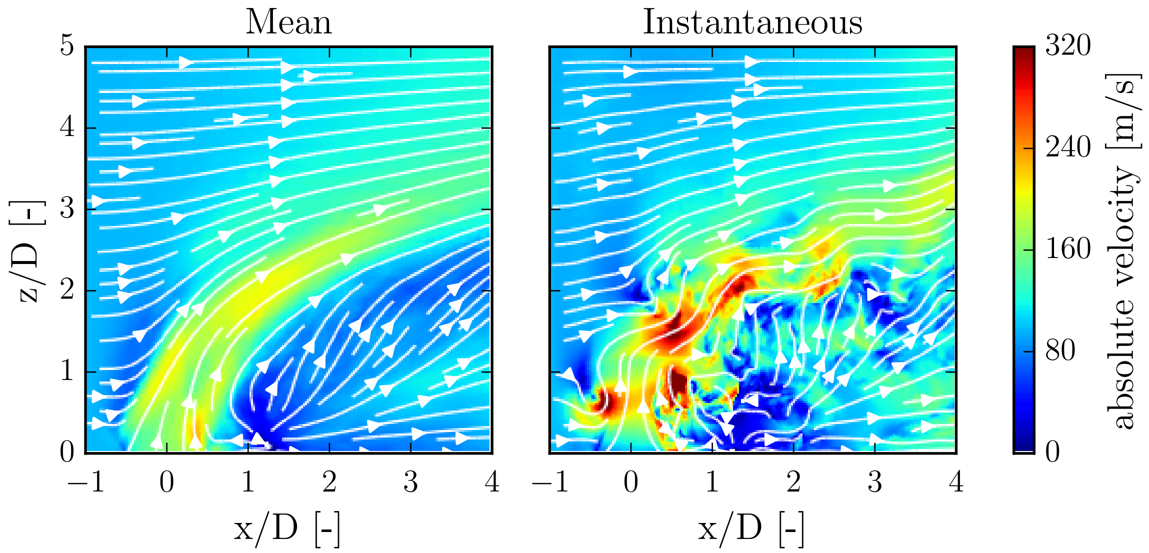

Figure 5.53: Mean (left) and instantaneous (right) velocity magnitude from engine configuration including flame lift-off at $y/D = 0$. In white stream lines computed from the displayed velocity.

combustion takes place.

The flame lift-off in figure 5.54 can clearly be seen by the iso-contour of the heat release rate on the right in the instantaneous temperature field. Comparing the instantaneous temperatures in figure 5.54 to those without lift-off in figure 5.45, the smaller maximum temperature is remarkable. This is important, since the NO_x values presented in the following are smaller than without lift-off. The reason for the temperature decrease, while keeping the equivalent ratio unchanged, is the mixing of jet and crossflow before combustion takes place. The mean and instantaneous temperature in figure 5.54 reveals significant pre-flame mixing, as the temperature increases although combustion has not yet taken place. The maximum mean temperature is reduced from 1950 K to 1910 K when the lift-off criteria is included.

In figure 5.55 the resulting NO_x concentrations are displayed in PPM at $x/D = 4$ normal to the x-direction. Both, the mean distribution and the mean values have changed in comparison to figure 5.46. When lift-off is included via the LO correlation, the maximum NO_x value is halved to 5 ppm. Simultaneously, as the penetration depth is reduced, the location of

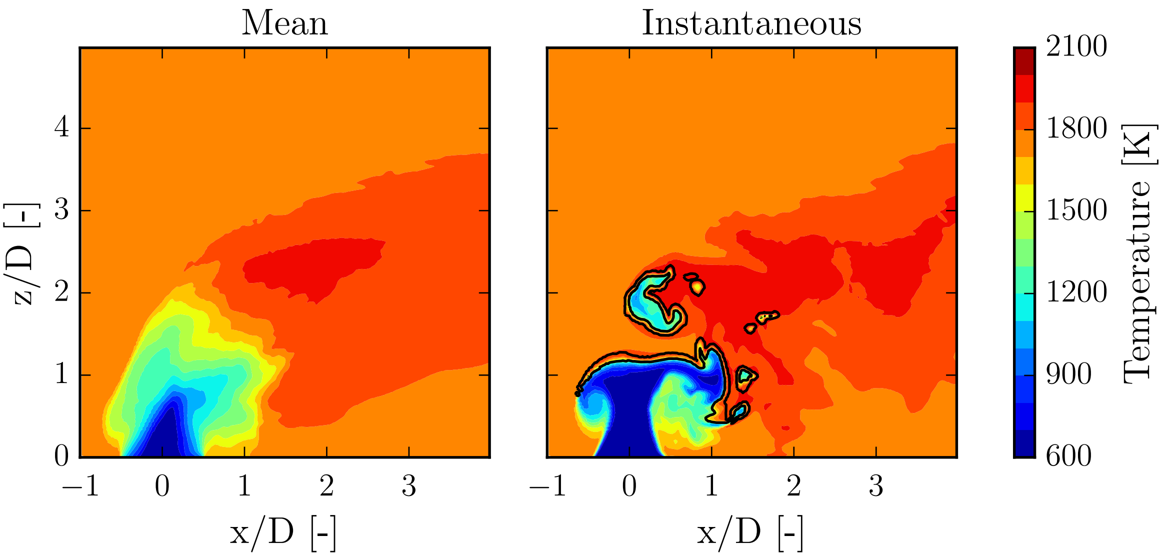

Figure 5.54: Mean (left) and instantaneous (right) temperature from engine configuration including flame lift-off at $y/D = 0$. In black, an iso-contour representing $1/10$ of the maximum heat release rate.

the highest concentrations is shifted in x-direction by 0.25 D. The location of the highest concentration is now found in a single area in the center of the jet. The field with the instantaneous values has a more circular shape in comparison with figure 5.46, which shows two symmetrical zones corresponding to the counter rotating vortex pair.

The source term for the $\mathrm{NO_x}$ formation at the symmetry plane, shown in figure 5.56, reveals the differences in emission formation between the standard PaSR model and PaSR model extended by lift-off. As figure 5.56 and 5.47 are of same scale, a direct comparison is possible. The flame lift-off is clearly visible in the field of the instantaneous values in figure 5.56, as below $x/D = 0.6$ no $\mathrm{NO_x}$ source term is present. The $\mathrm{NO_x}$ source term within the flame is significantly lower when lift-off is included. The smaller $\mathrm{NO_x}$ source term is caused by the lower combustion temperature due to dilution of the jet with cross flow material before combustion takes place. The lower combustion temperature also reduces the source term of the post flame $\mathrm{NO_x}$. The mean values on the left reveal that the flame lift-off shifts

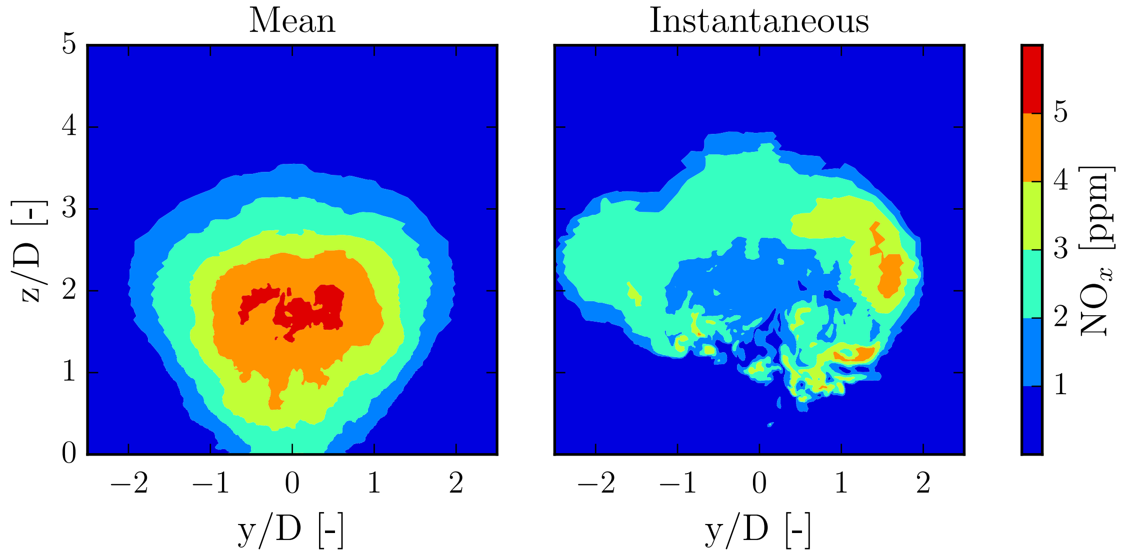

Figure 5.55: Mean (left) and instantaneous (right) NO_x distribution at $x/D = 4$ for engine conditions including flame lift-off.

the center of the NO_x formation downstream.

The NO_x concentration in the symmetry plane is displayed in figure 5.57. Here, the scale differs from figure 5.48. Beside the smaller concentrations and the lower penetration depth of the jet, the distribution for the mean values is quite similar. The increase of the mean NO_x concentrations towards $x/D = 4$ is again not only due to NO_x formation which is comparably low, as figure 5.56 reveals. The increasing NO_x concentrations are partly caused by the transport of the counter rotating vortex pair into the center of the jet.

Mean and instantaneous values of $\dot{\omega}_{NO_x}$ for the lifted case are shown in figure 5.58 and 5.59. The absolute values of the NO_x source term are lower than without lift-off. Generally, the mean values show a similar distribution of the NO_x source term than without lift-off which is shown in figures 5.49 and 5.50. At $z/D = 0.5$, which is below the lift-off height, zones with NO_x formation are visible. The flame is present because it can move below the lift-off height within the region, where the lift-off variable has a smooth gradient. The mean results in the following planes in figures 5.58 and 5.59 reveal a downstream shift of the flame, as the main NO_x formation is also

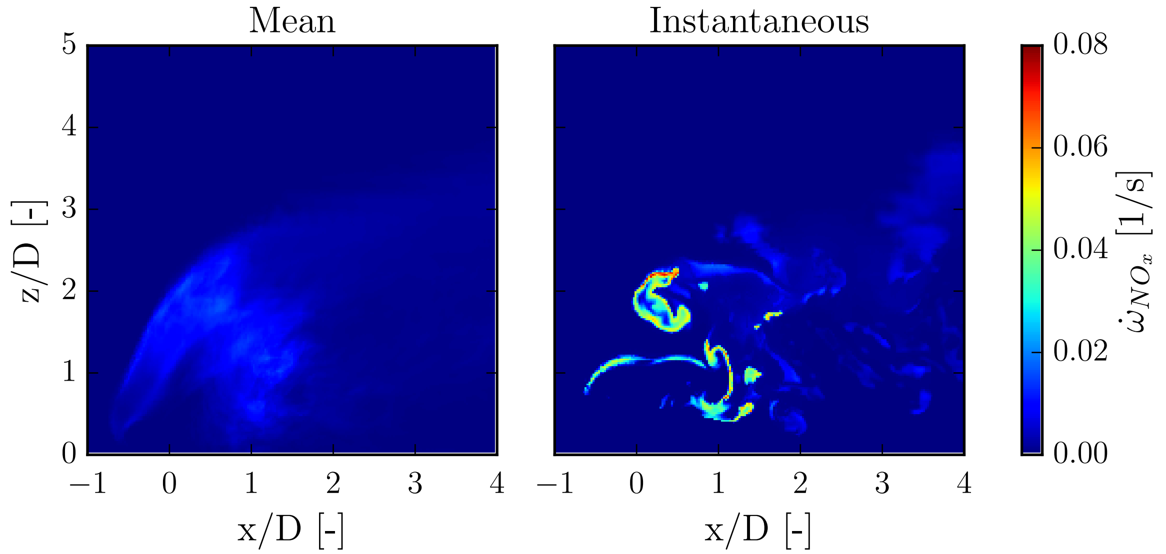

Figure 5.56: Mean (left) and instantaneous (right) reaction rates $\dot{\omega}_{NO}$ at $y/D = 0$ for engine conditions including flame lift-off.

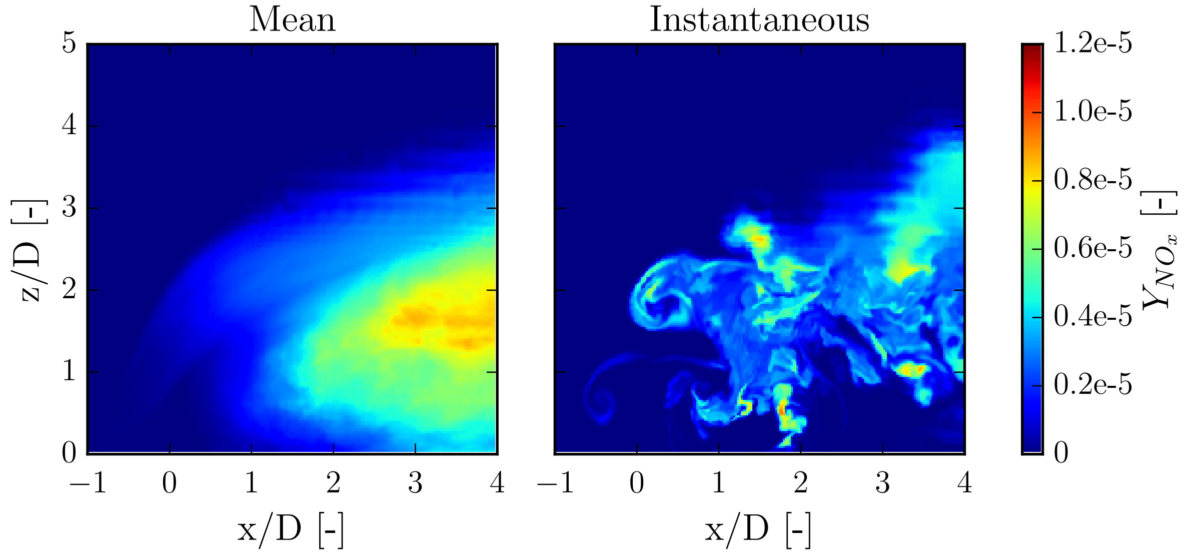

Figure 5.57: Mean (left) and instantaneous (right) NO_x mass fraction at $y/D = 0$ for engine conditions including flame lift-off.

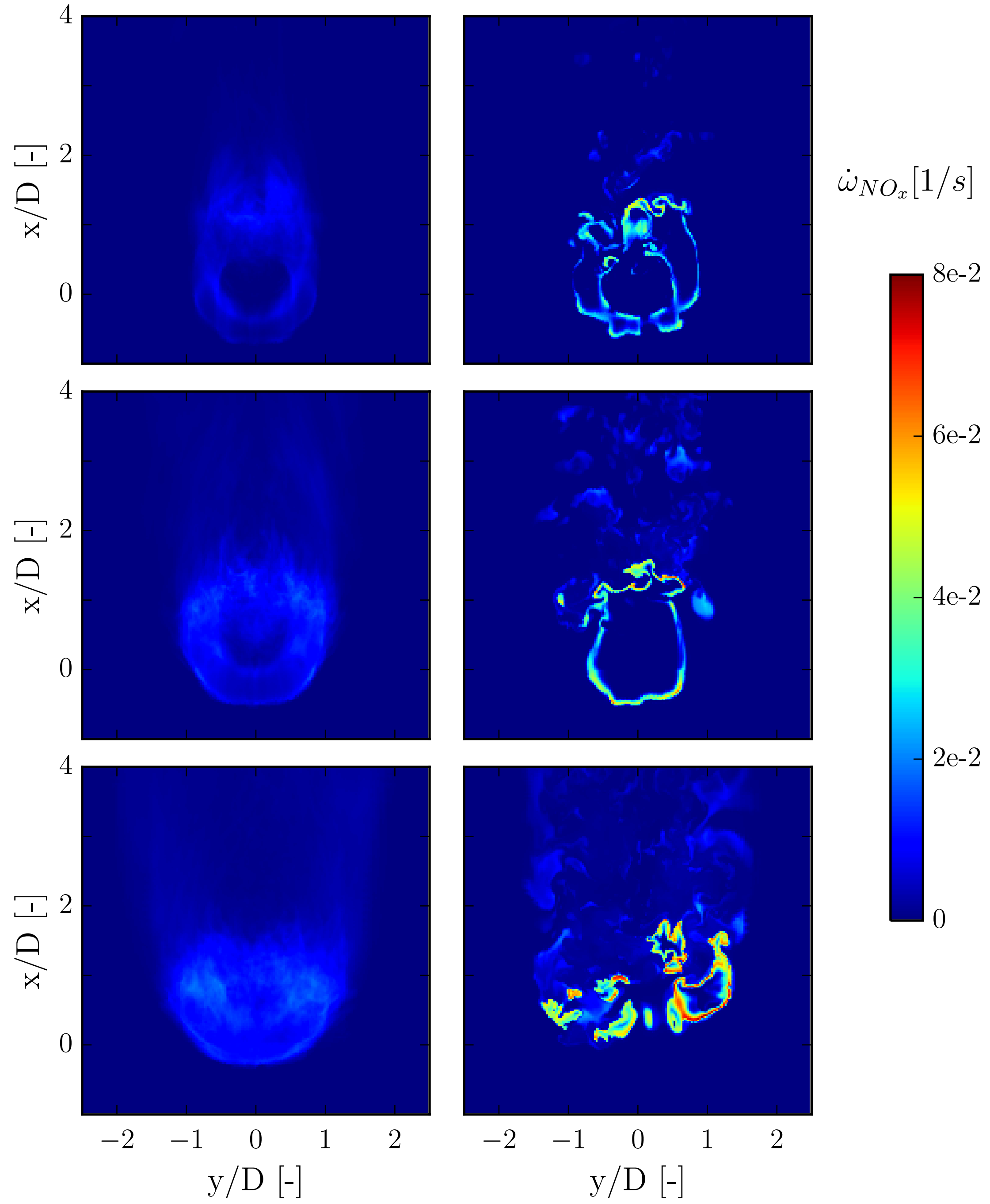

Figure 5.58: Mean (left) and instantaneous (right) reaction rates $\dot{\omega}_{NO}$ at $z/D = 0.5$ (first row), $z/D = 1$ (second row) and $z/D = 1.5$ (third row) for engine conditions including flame lift-off.

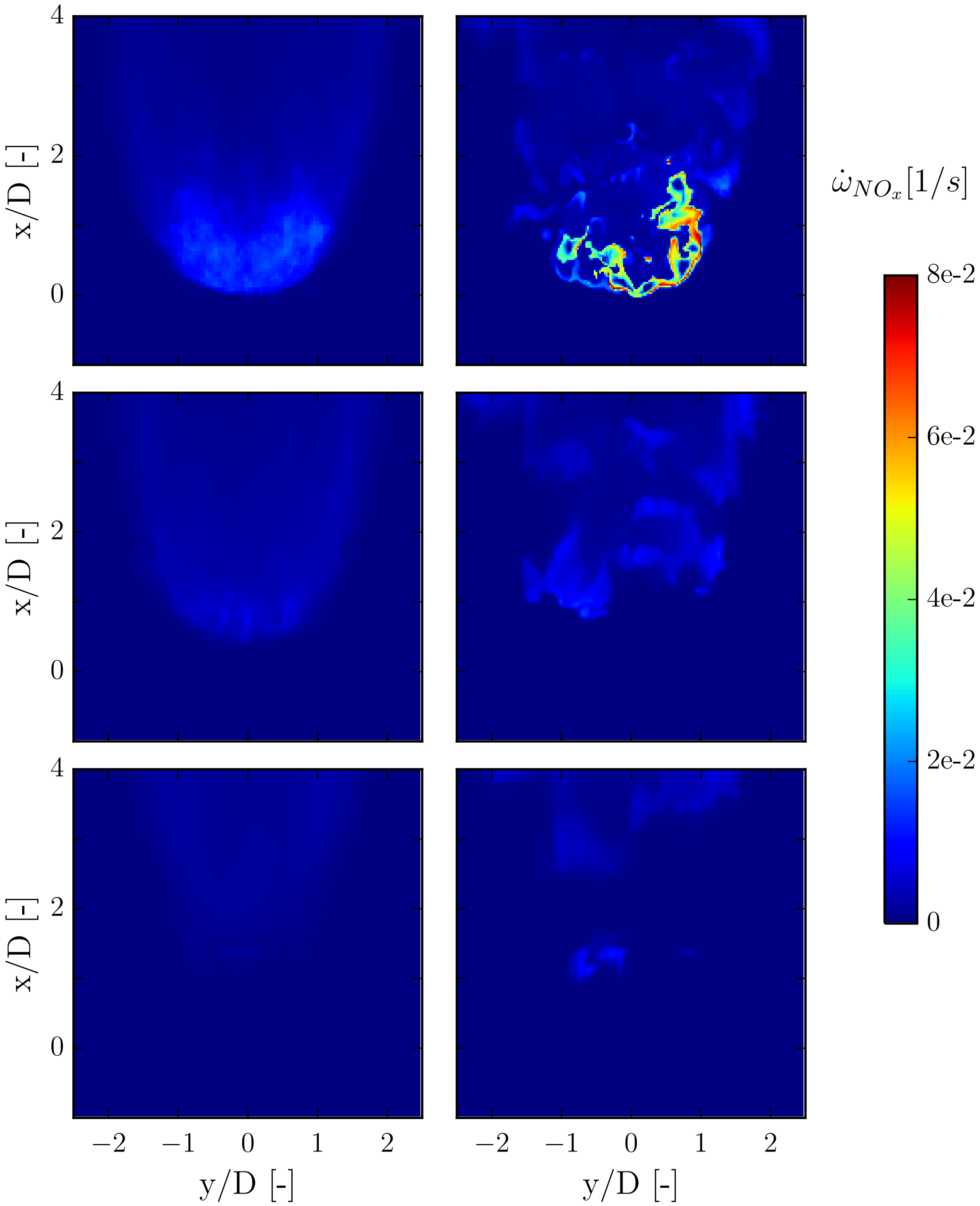

Figure 5.59: Mean (left) and instantaneous (right) reaction rates $\dot{\omega}_{NO}$ at $z/D = 2$ (first row), $z/D = 2.5$ (second row) and $z/D = 3$ (third row) for engine conditions including flame lift-off.

shifted downstream. At $z/D = 1$ the mean source term is significant lower while at $z/D = 1.5$ and $z/D = 2$ the source term almost reach the values without lift-off. Furthermore, the lower penetration depth is seen when lift-off is taken into account. In figure 5.59 the mean values at $z/D = 2.5$ are located more downstream than at the same position in figure 5.50.

The lower penetration depth can even be better identified from the $\mathrm{NO_x}$ concentrations. The mean and instantaneous values for Y_{NO_x} are shown in figures 5.60 and 5.61. The mean $\mathrm{NO_x}$ concentrations are shifted downstream when comparing lift-off results in figure 5.61 to those without lift-off in figure 5.52, although both figures employ different scales. The mean $\mathrm{NO_x}$ concentrations further show a different pattern at $z/D = 1$ and $z/D = 1.5$. The high concentrations of Y_{NO_x} in the centers of the counter rotating vortices visible in figure 5.51 do not appear in figure 5.60, where lift-off is taken into account. The instantaneous fields of the $\mathrm{NO_x}$ concentrations show a significantly lower level when comparing lift-off to no lift-off.

Concluding from these results, flame lift-off can reduce the amount of $\mathrm{NO_x}$ produced in the jet in crossflow configuration. In the presented case, the lift-off allows pre-flame mixing between jet and crossflow and thereby reduces the mean peak combustion temperature by 40 K. The resulting $\mathrm{NO_x}$ concentrations are reduced accordingly, the peak $\mathrm{NO_x}$ concentration by almost 50 %.

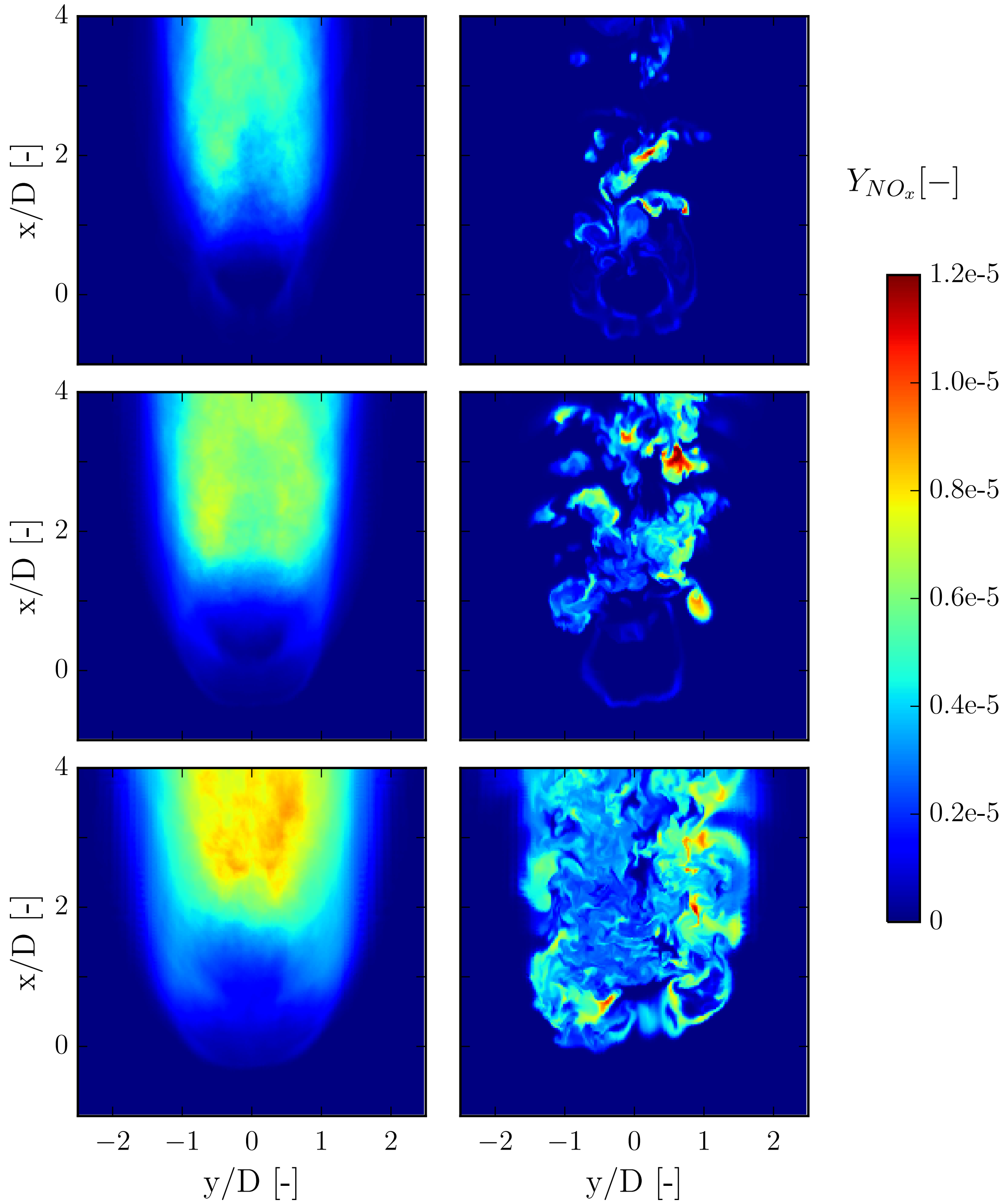

Figure 5.60: Mean (left) and instantaneous (right) $\mathrm{NO_x}$ mass fraction at $z/D = 0.5$ (first row), $z/D = 1$ (second row) and $z/D = 1.5$ (third row) for engine conditions including flame lift-off.

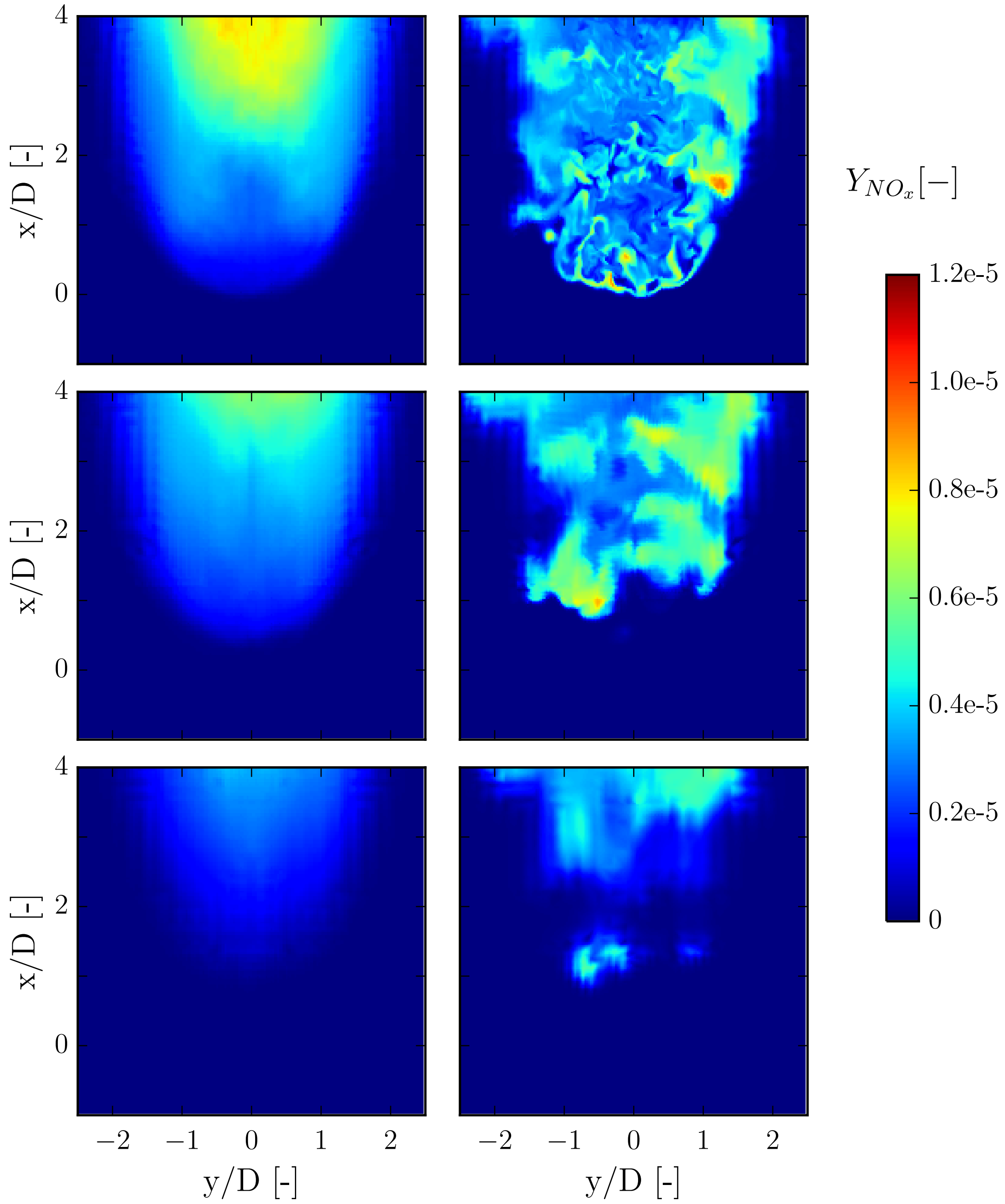

Figure 5.61: Mean (left) and instantaneous (right) $\mathrm{NO_x}$ mass fraction at $z/D = 2$ (first row), $z/D = 2.5$ (second row) and $z/D = 3$ (third row) for engine conditions including flame lift-off.

6 Summary and Conclusions

The current developement of gas turbine combustion systems is driven by the improvement of operational flexibility, the increase of combustion temperature and pressure and the reduction of NO_x emissions. NO_x emissions must be decreased because of continuously stricter emission limits. In parallel, the flexibility of gas turbines need to be improved to compensate fluctuations from renewable sources. Late Lean Injection is supposed to improve both factors. In order to allow its investigation and optimization at moderate costs, a numerical tool has been developed. Two common combustion models have been combined with a newly developed NO_x model forming a numerical setup which has not been presented before.

The combustion process is handled either by the partially stirred reactor (PaSR) model or the thickened flame model (TFM). The temperature distribution resulting from the two combustion models differs but does not exceed the adiabatic flame temperature, which is the physical limit. The PaSR model consumes the jet mixture without a preceding dilution, whereas the TFM consumes a jet mixture which is previously partially diluted by crossflow. Both combustion models use reduced one step finite rate chemistry not taking NO_x into account. In order to calculate NO_x a separated model has been developed. In the model, the NO_x formation is separated in-flame NO_x and post-flame NO_x. The source term of NO_x within the flame is tabulated based on the progress variable. The source term of the post flame NO_x is modeled by a partial equilibrium approach based on the GRI3.0 mechanism. This NO_x model is firstly coupled to a LES approach and can also be combined with any other combustion model as far as species concentration and temperature are available.

Data of an atmospheric test rig are used to validate the numerical results. The test rig is scaled to provide a combustion regime which is comparable to the gas turbine combustion process. The comparison of measurement and simulation without chemical reaction shows an excellent agreement for velocity and temperature. Numerically predicting the velocity measurements including chemical reaction is more challenging. Using the TFM model, the measured velocities are predicted with an error of 10 %. With the PaSR model the error even increases to 20 %. When the simulated flame shapes, defined by the heat release rate, are compared to the experimental OH* signal, the PaSR model agrees better with the experiment. Consequently, the temperature distributions of the two combustion models differ. Based on these temperature fields the NO_x emissions are calculated. When the temperature of simulation and experiment are close to each other, the resulting NO_x emissions differ only by one to two ppm.

The simulation under engine conditions gives detailed insight into the NO_x formation processes for the cases of technical interest. It is shown that mixing reduces the temperature which lowers the total amount of NO_x formed. In addition, an improvement of overall mixing is observed when the absolute velocities are increased.

The mixing process is enforced by flame lift-off, which is observed in experiments and expected under engine conditions. In the PaSR model, lift-off is achieved by including an appropriate lift-off correlation. Results for a lifted flame under engine conditions show a significant reduction of the mean flame temperature and subsequently a reduction of the NO_x emissions.

In order to intensify the mixing between jet and crossflow, different jet geometries are investigated with means of LES. It is found out that a rectangular slot significantly improves the mixing rate in the near field. Furthermore, a positive improvement of mixing quality is found by the generation of additional large scale vortices through the introduction of swirl in the jet.

So far, the combustion and NO_x formation models have been only applied to circular jets. In addition it has been shown that low drag jet injector geometries like slots aligned with the cross flow leads to better jet entrainment. An open issue for future work is the computation of reacting cases with non-circular jet injectors in order to reduce NO_x formation in axially staged combustors to its minimum.

Supervised Theses

Associated with the research under discussion, there are a number of different ”student theses” (Semesterarbeiten, Diplomarbeiten, Bachelor Theses, or Master Theses). This students’ contribution was prepared at the Lehrstuhl für Thermodynamik in the years 2009 through 2015 under the close supervision of the author of this Ph.D. thesis with regard to all academic, professional, and context-related concerns. Various issues were investigated contributing to the simulation of a jet in crossflow simulation and especially to the combustion process modeling under this conditions. The author would like to express his sincere gratitude to all formerly supervised students for their commitment and support of this research project and of the Ph.D. thesis at hand.

Student	Thesis
Andreas Velte	*Numerical Investigation of a Vortex Burner with Focus on Mixing and Flame shape*, Bacherlor’s Thesis, 2011
Tobias Heel	*Numerical Tool for Analysing Different Jet in Crossflow Configurations*, Semesterarbeit, 2012
Nicolai Stadlmair	*Investigation of Boundary Conditions of a Jet in Crossflow Configuration by Large Eddy Smulations*, Diplomarbeit, 2012
Michael Schiffner	*Development of a Nitrogen Oxide Formation Modell for CFD Simulations*, Master’s Thesis, 2014

Bibliography

[1] Annamalai, K., and Puri, I. K., 2006. *Combustion Science and Engineering.* CRC Press.

[2] Berglund, M., Fedina, E., Fureby, C., Tegnér, J., and Sabelnikov, V., 2010. “Finite Rate Chemistry Large-Eddy Simulation of Self-Ignition in a Supersonic Combustion Ramjet”. *AIAA Journal,* ***48***(3), pp. 540–550.

[3] Bibrzycki, J., Poinsot, T., and Zajdel, A., 2010. “Investigation of Laminar Flame Speed of CH4/N2/O2 and CH4/CO2/O2 Mixtures Using Reduced Chemical Kinetic Mechanisms”. *Archivum Combustionis,* ***30***(4), pp. 287 – 296.

[4] Borghi, R., 1985. “On the Structure and Morphology of Turbulent Premixed Flames”. In *Recent Advances in the Aerospace Sciences.* Plenum Publishing Corporation, pp. 117–138.

[5] Boss, J., 1986. “Evaluation of the Homogeneity Degree of a Mixture”. *Bulk solids handling,* ***6***, pp. 1207–1215.

[6] Boudier, G., Staffelbach, G., Gicquel, L. Y. M., and Poinsot, T. J., 2008. “Mesh Dependency of Turbulent Reacting Large-Eddy Simulations of a Gas Turbine Combustion Chamber”. In *Quality and Reliability of Large-Eddy Simulations*, J. Meyers, B. J. Geurts, and P. Sagaut, Eds., Vol. 12 of *Ercoftac Series.* Springer Netherlands, pp. 319–330.

[7] Boyce, M. P., 2012. *Gas Turbine Engeneering Handbook.* Butterworth-Heinemann.

[8] Cannon, S., Smith, C., and Anand, M., 2003. “LES Predictions of Combustor Emissions in a Practical Gas Turbine Combustor”. In 39th

AIAA/ASME/SAE/ASEE Joint Propulsion Conference and Exhibit Joint Propulsion Conferences, no. 4521.

[9] Cárdenas, C., Suntz, R., and Bockhorn, H., 2010. "Experimental Investigation of the Mixing-Process in a Jet-in-Crossflow Arrangement by Simultaneous 2d-LIF and PIV". In *Micro and Macro Mixing*. Springer-Verlag Berlin Heidelberg.

[10] Chapuis, M., Fureby, C., Fedina, E., Alin, N., and Tegnér, J., 2010. "LES Modelling of Combustion Applications Using OpenFOAM". In V European Conference on Computational Fluid Dynamics, J. Pereira and A. Sequeira, Eds.

[11] Clayton, D. J., and Jones, W. P., 2005. "Large Eddy Simulation of Impinging Jets in a Confined Flow". *Engineering Turbulence Modelling and Experiments,* ***6***, pp. 247–256.

[12] Collin, O., Ducros, F., Veynante, D., and Poinsont, T., 2000. "A Thickened Flame Model for Large Eddy Simulations of Turbulent Premixed Combustion". *Physics of Fluids,* ***12***(7), pp. 1843–1863.

[13] Collonval, F., and Polifke, W., 2014. "Modelling the Formation of Oxodes of Nitrogen in Premix Combustion by Extending Tabulated Chemistry with Algebraic Relations". In Proceedings of ASME Turbo Expo 2014: Turbine Technical Conference and Exposition, no. GT2014-27293.

[14] Davidson, L., 2009. An Introduction to Turbulence Models. Department of Thermo and Fluid Dynamics, Chalmers University of Technology, Goeteborg, Sweden, August. Publication 97/2.

[15] Denev, J. A., Fröhlich, J., and Bockhorn, H., 2005. "Evaluation of Mixing and Chemical Reaction within a Jet in Crossflow by Means of LES". In Proceedings of the European Combustion Meeting.

[16] Denev, J. A., Fröhlich, J., and Bockhorn, H., 2006. Direct Numerical Simulation of Mixing and Chemical Reactions in a Round Jet into a Crossflow - a Benchmark. Tech. rep., Trans. of the High Performance Computing Center Stuttgart (HLRS).

[17] Denev, J. A., Fröhlich, J., and Bockhorn, H., 2007. “Direct Numerical Simulation of a Transitional Jet in Crossflow with Mixing and Chemical Reactions”. In Proceedings of the 5th Int. Symp. on Turbulence and Shear Flow Phenomena, R. Friedrich, N. Adams, J. Eaton, J. Humphrey, N. Kasagi, and M. Leschziner, Eds., Vol. 3, pp. 1243–1248.

[18] Denev, J. A., Fröhlich, J., and Bockhorn, H., 2009. “Large Eddy Simulation of a Swirling Transverse Jet into a Crossflow with Investigation of Scalar Transport”. *Physics of Fluids,* ***21***, pp. 1–20.

[19] Denev, J. A., Fröhlich, J., Falconi, C. J., and Bockhorn, H., 2010. “Direct Numerical Simulation, Analysis and Modelling of Mixing Processes in a Round Jet in Crossflow”. In *Micro and Macro Mixing*, H. Bockhorn, D. Mewes, W. Peukert, and H.-J. Warnecke, Eds., Heat and Mass Transfer. Springer Berlin Heidelberg, pp. 143–164.

[20] Fric, T. F., and Roshko, A., 1994. “Vortical Structure in the Wake of a Transverse Jet”. *Journal of Fluid Mechanics,* ***279***, 11, pp. 1–47.

[21] Galeazzo, F. C. C., Donnert, G., Cárdenas, C., Sedlmaier, J., Habisreuther, P., Zarzalis, N., Beck, C., and Krebs, W., 2013. “Computational Modeling of Turbulent Mixing in a Jet in Crossflow”. *International Journal of Heat and Fluid Flow,* ***41***, pp. 55–65.

[22] Galeazzo, F. C. C., Donnert, G., Habisreuther, P., Zarzalis, N., Valdes, R. J., and Krebs, W., 2011. “Measurement and Simulation of Turbulent Mixing in a Jet in Crossflow”. *Journal of Engineering for Gas Turbines and Power,* ***133***, pp. 1–10.

[23] Germano, M., Piomelli, U., Moin, P., and Carbot, W., 1991. “A dynamic subgrid-scale eddy viscosity model”. *Phys. Fluids,* ***7***(A 3), pp. 1760 – 1765.

[24] Glassman, I., and Yetter, R. A., 2008. *Combustion*, 4th ed. Academic Press, Amsterdam.

[25] Golovitchec, V., and Chomiak, J., 2001. “Numerical Modeling of high Temperature Air ”Flameless” Combustion”. In 4th International Symposium on High Temperature Air Combustion and Gasification, Rome, Italy.

[26] Goodwin, D., Moffat, H., and Speth, R., 2012. Cantera: An object-oriented software toolkit for chemical kinetics, thermodynamics, and transport processes. `http://www.cantera.org`. Version 2.0.0.

[27] Grout, R. W., Gruber, A., Yoo, C. S., and Chen, J. H., 2011. “Direct Numerical Simulation of Flame Stabilization Downstream of a Transverse Fuel Jet in Cross-Flow”. *Proceedings of the Combustion Institute,* ***33***, pp. 1629–1637.

[28] Gutmark, E. J., Ibrahim, I. M., and Murugappan, S., 2008. “Circular and Noncircular Subsonic Jets in Cross Flow”. *Physics of Fluids,* ***20***, pp. 1–17.

[29] Hanson, R. K., and Salimian, S., 1984. “Survey of Rate Constants in the N/H/O System”. In *Combustion Chemistry*, W. C. G. Jr., Ed. Springer, ch. 6, pp. 362–421.

[30] Harworth, D. C., 2010. “Progress in Probability Density Function Methods for Turbulent Reacting Flows”. *Progress in Energy and Combustion Science,* ***36***, pp. 168–259.

[31] Hirano, K., Nonaka, Y., Kinoshita, Y., Oshima, N., and Matsuya, K., 2012. “Large Eddy Simulation in an Industrial Gasturbine Combustor for NOx Prediction”. In Proceedings of ASME Turbo Expo, no. GT2012-68925.

[32] Huang, C., and Lipatnikov, A. N., 2012. “Comparison of Presumed PDF Models of Turbulent Flames”. *Journal of Combustion,* ***2012***, pp. 1–15.

[33] Hughes, K. J., Turányi, T., Clague, A. R., and Pilling, M. J., 2001. “Development and Testing of a Comprehensive Chemical Mechanism for the Oxidation of Methane”. *International Journal of Chemical Kinetics,* ***33***(9), pp. 513–538.

[34] Hunt, J., Wray, A., and Moin, P., 1988. “Eddies, Streams and Convergence Zones in Turbulent Flows”. In Proc. 1988 Summer Program, no. CTR-S88, Stanford N.A.S.A. Centre for Turb. Res.

[35] Ihme, M., and Pitsch, H., 2008. “Modeling of Radiation and Nitric Oxide Formation in Turbulent Nonpremixed Flames Using a Flamelet/Progress Variable Formulation”. *Phys. Fluids,* ***20***, pp. 1–20.

[36] International Energy Agency, 2013. Energy Policies of IEA Countries Germany. Tech. rep., International Energy Agency.

[37] Ivanova, E. M., Noll, B. E., Griebel, P., Aigner, M., and Syed, K., 2011. “Numerical Simulation of Turbulent Mixing and Autoignition of Hydrogen Fuel at Reheat Combustor Operating Conditions”. In Proceedings of ASME Turbo Expo: Power for Land, Sea and Air, no. GT2011-46264.

[38] Karvinen, A., and Ahlstedt, H., 2005. “Comparisson of Turbulence Models in Case of Jet in Crossflow Using Commercial CFD Code”. *Journal of Engineering Turbulence Modelling and Experiments,* ***6***, pp. 399–408.

[39] Kempf, A., Klein, M., and Janicka, J., 2005. “Efficient Generation of Initial- and Inflow- Conditions for Transient Turbulent Flows in Arbitrary Geometries”. *Flow, Turbulence and Combustion,* ***74***, pp. 67–84.

[40] Kolb, M., 2015. “Influence of the Injector Geometry on Mixing and Lift-Off of Premixed Jet Flames in Hot Cross Flow”. PhD thesis, Technische Universität München.

[41] Kolb, M., Ahrens, D., Hirsch., C., and Sattelmayer, T., 2015. “A model for predicting the lift-off height of premixed jets in vitiated cross flow”. In Procesdings of ASME Turbo Expo 2015: Turbine Technical Conference and Exposition, no. GT2015-42225.

[42] Konnov, A. A., and De Ruyck, J., 2001. “Temperature-Dependent Rate Constant for the Reaction NNH + O $\rightarrow$ NH + NO”. *Combustion and Flame,* ***125***(4), pp. 1258 – 1264.

[43] Kulkarni, R., 2013. "Large Eddy Simulations of Autoignition in Turbulent Flows". PhD thesis, Technische Universität München.

[44] Kutsenko, Y. G., and Onegin, S. F., 2006. "Development and Application of CFD-Based Analysis Methodology to Evaluate Efficiency of Low NOx Combustion Technologies". In ASME Turbo Expo 2006: Power for Land, Sea and Air, no. GT2006-90530.

[45] Lechner, C., and Seume, J., 2010. *Stationäre Gasturbinen.* Springer Berlin Heidelberg.

[46] Legier, J. P., Poinsont, T., and Veynante, D., 2000. "Dynamically Thickened Flame LES Model for Premixed and Non-Premixed Turbulent Combustion". In Proceedings of the Summer Programm 2000, Center for Turbulence Research.

[47] Lilly, D. K., 1992. "A Proposed Modification of the Germano Subgrid-Scale Closure Method". *Phys. Fluids,* ***3***(A 4), pp. 633 – 635.

[48] Lund, T. S., Wu, X., and Squires, K. D., 1998. "Generation of Turbulent Inflow Data for Spatially-Developing Boundary Layer Simulations". *Journal of Computational Physics,* ***140***(2), pp. 233 – 258.

[49] Mahesh, K., 2013. "The Interaction of Jets with Crossflow". *Annual Review of Fluid Mechanics,* ***45***(1), pp. 379–407.

[50] Meneveau, C., and Poinsot, T., 1991. "Stretching and Quenching of Flamelets in Premixed Turbulent Combustion". *Combustion and Flame,* ***86***, pp. 311–332.

[51] Mengler, C., Heinrich, C., Sadiki, A., and Janicka, J., 2001. "Numerical Prediction of Momentum and Scalar Fields in a Jet in Cross Fow: Comparison of LES and Second Order Turbulence Closure Calculations". In Proceedings of Turbulence and Shear Flow Phenomena Conferences, Vol. 2, pp. 425–430.

[52] Miller, J. A., and Bowman, C. T., 1989. "Mechanism and Modeling of Nitrogen Chemistry in Combustion". *Progress in Energy and Combustion Science,* ***15***(4), pp. 287–338.

[53] Muppidi, S., and Mahesh, K., 2007. "Direct Numerical Simulation of Round Turbulent Jets in Crossflow". *Journal of Fluid Mechanics,* ***574***, pp. 59–84.

[54] O'Rourke, P. J., and Bracco, F. V., 1979. "Two Scaling Transformations for the Numerical Computation of Multidimensional Unsteady Laminar Flames". *Journal of Computational Physics,* ***33***, pp. 185–203.

[55] Peters, N., 1986. "Laminar Flamelet Concepts in Turbulent Combustion". In 21st (Int.) Symposium on Combustion, Vol. 21, pp. 1231–1250.

[56] Petersen, E. L., Kalitan, D. M., Simmons, S., Bourque, G., Curran, H. J., and Simmie, J. M., 2007. "Methane/Propane Oxidation at High Pressures: Experimental and Detailed Chemical Kinetic Modeling". *Proceedings of the Combustion Institute,* ***31***(1), pp. 447 – 454.

[57] Pitsch, H., 2002. A G-Equation Formulation for Large-Eddy Simulation of Premixed Turbulent Combustion. Annual Research Briefs, Center for Turbulence Research.

[58] Poinsot, T., and Veynante, D., 2005. *Theoretical and Numerical Combustion*, 2 ed. R.T. Edwards.

[59] Prière, C., Gicquel, L. Y. M., P., K., Krebs, W., and Po, 2005. "Large Eddy Simulation Prediction of Mixing Enhancement for Jets in Cross Flow". *Journal of Turbulence,* ***5***, pp. 1–24.

[60] Reynolds, O., 1883. "An Experimental Investigation of the Circumstances which Determine Whether the Motion of Water Shall be Direct or Sinuous and of the Law of Resistance in Parallel Channels". *Philosophical Transactions of the Royal Society of London,* ***174***, pp. 935–982.

[61] Rusch, D., Blum, A., Moser, A., and Roesgen, T., 2008. "Turbulence Model Validation for Fire Simulation by CFD and Experimental Investigation of a hot Jet in Crossflow". *Fire Safety Journal,* ***43***, pp. 429–441.

[62] Schlüter, J. U., and Schönfeld, T., 2000. "LES of Jets in Cross Flow and its Application to a Gas Turbine Burner". *Flow, Turbulence and Combustion,* ***65***(2), pp. 177–203.

[63] Schmitt, D., Kolb, M., Weinzierl, J., Hirsch, C., and Sattelmayer, T., 2013. "Ignition and Flame Stabilization of a Premixed Jet in Hot Cross Flow". In Proceedings of the ASME Turbo Expo 2013, no. GT2013-94763, ASME.

[64] Smagorinsky, J., 1963. "General Circulation Experiments with the Primitive Equations, I. The Basic Experiment". *Monthly Weather Review,* ***91***(3), March, pp. 99–164.

[65] Smith, G. P., Golden, D. M., Frenklach, M., Moriarty, N. W., Eiteneer, B., Goldenberg, M., Bowman, C. T., Hanson, R. K., Song, S., Gardiner, Jr., W. C., Lissianski, V. V., and Qin, Z. `http://www.me.berkeley.edu/gri_mech/`.

[66] Spalding, D., 1971. "Mixing and chemical reaction in steady confined turbulent flames". *Symposium (International) on Combustion,* ***13***(1), pp. 649 – 657. Thirteenth symposium (International) on Combustion-Thirteenth symposium (International) on Combustion.

[67] Turns, S. R., 2000. *An Introduction to Combustion.* McGraw-Hill, Boston.

[68] Versteeg, H. K., and Malalasekera, W., 2007. *An Introduction to Computational Fluid Dynamics.* Pearson Education Limited.

[69] Veynante, D., and Poinsot, H., 1997. Large Eddy Simulation of Combustion Instabilities in Turbulent Premixed Burners. Annual research briefs, Center for Turbulence Research.

[70] Westbrook, C. K., and Dryer, F. L., 1981. "Simplified Reaction Mechanisms for the Oxidation of Hydrocarbon Fuels in Flames". *Combustion Science and Technology,* ***27***, pp. 31–43.

[71] Yuan, L., and Street, R., 1998. "Trajectory and Entrainment of a Round Jet in Crossflow". *Phys. Fluids,* ***10***(9), pp. 2323–2335.

A Cantera's Reactor Model

Continuity

$$\frac{dm}{dt} = \sum_{in} \dot{m}_{in} - \sum_{out} \dot{m}_{out} + \dot{m}_{wall} \tag{A.1}$$

$$\dot{m}_{k,gen} = V\dot{\omega}_k W_k + \dot{m}_{k,wall} \tag{A.2}$$

$$\frac{d(mY_k)}{dt} = \sum_{in} \dot{m}_{in} Y_{k,in} - \sum_{out} \dot{m}_{out} Y_k + \dot{m}_{k,gen} \tag{A.3}$$

$$\frac{d(mY_k)}{dt} = \sum_{in} \dot{m}_{in} \left(Y_{k,in} - Y_k\right) + V\dot{\omega}_k W_k + \dot{m}_{k,wall} \tag{A.4}$$

$$\frac{d(mY_k)}{dt} = m\frac{dY_k}{dt} + Y_k\frac{dm}{dt} \tag{A.5}$$

$$\dot{m} + Y_k \left[\sum_{in} \dot{m}_{in} - \sum_{out} \dot{m}_{out} + \dot{m}_{wall}\right] = \sum_{in} \dot{m}_{in} Y_{k,in} - \sum_{out} Y_k + \dot{m}_{k,gen} \tag{A.6}$$

$$m\frac{dY_k}{dt} = \sum_{in} \dot{m}_{in} \left(Y_{k,in} - Y_k\right) - Y_k \dot{m}_{wall} + \dot{m}_{k,gen} \tag{A.7}$$

Energy

$$\frac{dU}{dt} = -p\frac{dV}{dt} - \dot{Q} + \sum_{in} \dot{m}_{in} h_{in} - h\sum_{out} \dot{m}_{out} \tag{A.8}$$

$$H = U + pV \tag{A.9}$$

$$\frac{dH}{dt} = p\frac{dV}{dt} + V\frac{dp}{dt} \tag{A.10}$$

$$\frac{dH}{dt} = p\frac{dV}{dt} \tag{A.11}$$

$$\frac{dH}{dt} = \frac{dU}{dt} + p\frac{dV}{dt} \tag{A.12}$$

$$\frac{dH}{dt} = -\dot{Q} + \sum_{in} \dot{m}_{in} h_{in} - h\sum_{out} \dot{m}_{out} \tag{A.13}$$

$$H = m\sum_{k} Y_k h_k(T) \tag{A.14}$$

$$\frac{dH}{dt} = h\frac{dm}{dt} + mc_p\frac{dT}{dt} + m\sum_k h_k\frac{dY_k}{dt} \tag{A.15}$$

$$mc_p\frac{dT}{dt} = \dot{Q} - \sum_k h_k\dot{m}_{gen} + \sum_{in}\dot{m}_{in}\left(h_{in} - \sum_k h_k Y_{k,in}\right) \tag{A.16}$$

$$h\frac{dm}{dt} + mc_p\frac{dT}{dt} + m\sum_k h_k\frac{dY_k}{dt} = \dot{Q} + \sum_{in}\dot{m}_{in}h_{in} - h\sum_{out}\dot{m}_{out} \tag{A.17}$$

$$\begin{aligned}
-\dot{Q} + \sum_{in}\dot{m}_{in}h_{in} - h\sum_{out}\dot{m}_{out} = \\
h\left[\sum_{in} - \sum_{out}\dot{m}_{out} + \dot{m}_{wall}\right] + mc_p\frac{dT}{dt} + \\
\sum_k h_k\left[\sum_{in}\dot{m}_{in}\left(Y_{k,in} - Y_k\right) - Y_k\dot{m}_{wall} + \dot{m}_{k,gen}\right]
\end{aligned} \tag{A.18}$$

$$\begin{aligned}
-\dot{Q} + \sum_{in}\dot{m}_{in}h_{in} = \\
h\sum_{in}\dot{m}_{in} + \sum_k h_k\sum_{in}\dot{m}_{in}Y_{k,in} - \\
\sum_k h_k\sum_{in}\dot{m}_{in} + \sum_k h_k\dot{m}_{k,gen} + mc_p\frac{dT}{dt}
\end{aligned} \tag{A.19}$$

$$\sum_k h_k\sum_{in}\dot{m}_{in}Y_{k,in} + \sum_k h_k\dot{m}_{k,gen} + mc_p\frac{dT}{dt} = -\dot{Q} + \sum_{in}\dot{m}_{in}h_{in} \tag{A.20}$$

B Reaction Schemes

B.1 One Step Reaction Mechanism

$$CH_4 + 2O_2 \rightarrow CO_2 + 2H_2O \tag{B.1}$$

$$k_{+B.1} = A \;\; exp\left(-E_A/RT\right)[\mathrm{CH4}]^{\nu_1'}[\mathrm{O_2}]^{\nu_2'} \tag{B.2}$$

Reaction	A	E_A	ν_1'	ν_2'
$B.1$	$6.7E12$	48.4	0.2	1.3

Table B.1: One step reaction scheme from Westbrook and Dryer [70].

B.2 Two Step Reaction Mechanisms

$$CH_4 + 1.5O_2 \rightarrow CO + 2H_2O \tag{B.3}$$

$$CO + 0.5O_2 \rightarrow CO_2 \tag{B.4}$$

$$k_{+B.3} = A \;\; exp\left(-E_A/RT)\right][\mathrm{CH4}]^{\nu_1'}[\mathrm{O_2}]^{\nu_2'} \tag{B.5}$$

$$k_{+B.4} = A \;\; exp\left(-E_A/RT)\right][\mathrm{CO}]^{\nu_1'}[\mathrm{H_2O}]^{\nu_2'}[\mathrm{O_2}]^{\nu_3'} \tag{B.6}$$

$$k_{-B.4} = A \;\; exp\left(-E_A/RT)\right][\mathrm{CO_2}]^{\nu_1'} \tag{B.7}$$

$$CH_4 + 1.5O_2 \rightarrow CO + 2H_2O \tag{B.8}$$

$$CO + 0.5O_2 \rightarrow CO_2 \tag{B.9}$$

$$k_{+B.8} = A \;\; exp\left(-E_A/RT)\right][\mathrm{CH4}]^{\nu_1'}[\mathrm{O_2}]^{\nu_2'} \tag{B.10}$$

Reaction	A	E_A	ν_1'	ν_2'	ν_2'
$B.5$	$6.7E12$	48.4	0.2	0.25	
$B.6$	$3.98E14$	40.0	1.0	0.5	0.25
$B.7$	$5.0E8$	40.0	1.0		

Table B.2: Two step reaction scheme from Westbrook and Dryer [70].

$$k_{+B.9} = A \;\; exp\,(-E_A/RT)]\,[\mathrm{CO}]^{\nu_1'}[\mathrm{O_2}]^{\nu_2'} \tag{B.11}$$

$$k_{-B.9} = A \;\; exp\,(-E_A/RT)]\,[\mathrm{CO_2}]^{\nu_1'} \tag{B.12}$$

Reaction	A	E_A	ν_1'	ν_2'	ν_2'
$B.10$	$2.0E15$	35000	0.9	1.1	
$B.11$	$2.0E9$	12000	1.0	0.5	
$B.12$	$2.0E9$	12000	1.0		

Table B.3: Two step reaction scheme from Bibrzycki et al. [3].

C Turbulent Boundary Conditions

In the following a summary of the procedure for the generation of turbulent boundary condition described in Kempf et al. [39] is given. One theoretical approach to generate synthetic fluctuations of a velocity field is to apply a digital filter on a field of random numbers. This approach is expensive and Kempf et al. [39] developed an elegant solution to generate suitable fluctuations at lower costs. The desired spectra is obtained much cheaper by applying diffusion on a field of random numbers.

In a first step, a precursor mesh of the inlet is created. Therein, random noise U_i for three fields is generated. Normalizing leads to a mean value $\bar{U_i} = 0$ and $\bar{U_i U_i} = 1$. The fields are normalized by the volume $V_{\mathbf{i}}$ of each cell $\mathbf{i} = (i_x, i_y, i_z)$, $U_{i,\mathbf{i}} = \frac{U_i}{\sqrt{V_{\mathbf{i}}}}$ in order to make the diffusion process independent of the cell size.

In the next step, diffusion is applied on all three fields using a diffusion coefficient D. With increasing time, smaller scales vanish and the field is dominated by bigger scales.

$$\frac{\partial U_i}{\partial t} = D \frac{\partial^2 U_i}{\partial x_j^2} \tag{C.1}$$

As the number of time steps n increases, the remaining scales gets bigger. The size of the retained scales L can be estimated by the following equation:

$$L \approx \sqrt{2\pi c n} \Delta x \qquad \text{with} \qquad c = D \frac{\Delta t}{\Delta x^2}, \tag{C.2}$$

where Δt describes the time step and Δx is the width of a cell. It is shown in Kempf et al. [39], that a diffusion process like in C.1 is equivalent to the convolution of the original field with a Gauss-Filter, yielding an auto correlated function of Gaussian shape.

After the diffusion process stops, the field must again be normalized to $\bar{U_i} = 0$ and $\bar{U_i U_i} = 1$. Finally the velocity fluctuation field u_i' is constructed from a given Reynolds stress tensor τ_{ij}. Using the Lund transformation [48] the cross correlation for u'_i can be easily computed from U_i:

$$u'_i = a_{ij} U_j \tag{C.3}$$

$$a_{ij} = \begin{pmatrix} \sqrt{\tau_{11}} & 0 & 0 \\ \tau_{21}/a_{11} & \sqrt{\tau_{22} - a_{21}^2} & 0 \\ \tau_{21}/a_{11} & (\tau_{32} - a_{21}a_{31})/a_{22} & \sqrt{\tau_{33} - a_{31}^2 - a_{32}^2} \end{pmatrix} \tag{C.4}$$

After this transformation, an artificial turbulent velocity field u'_i is generated on the precursor mesh. Since artificial turbulent fluctuations are taken from a slice parallel to the inlet through from the precursor mesh are and mapped on the inlet.

This approach has two advantages in comparison to other turbulent boundary generation mechanisms. The presented approach uses the solution algorithms available within a CFD solver as the turbulence spectra is generated by a diffusion process (see equation C.1). This process is more complicated and more expensive within other turbulent boundary generation mechanisms where Fourier transformation and filtering is used to generate the turbulence spectra. The used mechanism to generate a turbulent boundary condition can also be applied on non-uniform meshes because the diffusion process does not depend on the mesh quality. This is not the case for a turbulence generator using Fourier transformation or filtering, where the filter width is connected to mesh size.

D Configurations

Conf.	$J\,[-]$	$D_{jet}\,[mm]$	$p\,[bar]$	$T_{jet}\,[K]$	$T_{cf}\,[K]$	$u_{cf}\,[m/s]$	$I\,[-]$	$\Phi\,[-]$	CM
1	6	100	1.01325	293	293	2.59	0.05	–	–
2	6	100	1.01325	293	293	2.59	0.0	–	–
3	15	50	1.01325	393	293	3.00	0.05	–	–
4	6	100	1.01325	293	293	2.59	0.05	–	–
5	6	100	1.01325	393	293	2.59	0.05	–	–
6	6	141x56.2	1.01325	393	293	2.59	0.05	–	–
7	6	100	1.01325	636	1773	16.21	0.05	0.66	$PaSR$
8	6	100	1.01325	636	1773	16.21	0.05	0.66	TFM
9	15	50	1.01325	636	1773	15.81	0.05	0.66	$PaSR$
10	15	50	1.01325	636	1773	15.81	0.05	0.66	TFM
engine	6	2.54	20	636	1773	98.05	0.05	0.66	$PaSR$

Table D.1: Overview of the configurations (I: turbulence intensity, CM: combustion model).